MEASUREMENTS OF BLACK CARBON PROPERTIES DURING CLOUD, BIOMASS BURNING, AND FREE TROPOSPHERIC CONDITIONS AT A MARINE BOUNDARY LAYER SITE AND HIGH ELEVATION MOUNTAIN SITE

by

Jason C. Schroder

B. Sc., Northern Arizona University, 2001

A THESIS SUBMITTED IN PARTIAL FULFILLMENT
OF THE REQUIREMENTS FOR THE DEGREE OF

Doctor of Philosophy

in

THE FACULTY OF GRADUATE AND POSTDOCTORAL STUDIES

(Chemistry)

The University of British Columbia
(Vancouver)

December 2014

Abstract

Black carbon is a subset of the total atmospheric aerosol population that is formed in the incomplete combustion of fossil fuels, biofuels, and biomass. This research focused on the properties of black carbon particles measured in the boundary layer and free troposphere, as well as the activation of black carbon particles by cloud droplets. The primary motivation for this research is to increase our understanding of the properties of black carbon under these different atmospheric conditions.

A single particle soot photometer was used to study properties of black carbon particles incorporated into cloud droplets at two field locations: 1) a marine boundary layer site, and 2) a high elevation mountain site. At both sites, a size dependence on the fraction of black carbon incorporated into cloud droplets was observed; and for small ($<$100 nm) diameters, black carbon was efficiently incorporated into droplets. In addition, at the marine boundary layer site, thick coatings were observed on the small diameter black carbon particles that were incorporated into the droplets, which was consistent with theory.

The single particle soot photometer was also used at a high elevation mountain site to investigate properties of black carbon from biomass burning and black car-

bon within the free troposphere. The average mass concentration of black carbon was found to be significantly higher ($\approx$ 9x) during periods of biomass burning than within the free troposphere, yet had similar mass median diameters. Coating thicknesses of black carbon containing particles during the two subsets of data were also investigated. Average coating thicknesses for black carbon core diameters between 140 to 160 nm was 55 nm when sampling in the free troposphere, but approximately 32 nm when sampling air masses influenced by biomass burning.

The results presented in this dissertation increase our understanding of the properties of black carbon particles and how they vary as a function of location and type of air mass sampled. This information can be used to further constrain computer models that are used to predict how black carbon can affect climate.

Preface

Chapter 4 is a co-authored journal article that has been accepted and published to an online discussion forum, and is awaiting peer review. Chapters 5 and 6 are being prepared for submission to peer-reviewed journals as co-authored journal articles. The details of my contributions to each research chapter, mentioned above, are outlined below.

Chapter 4 (first author of a published journal article) J. C. Schroder, S. J. Hanna, R. L. Modini, A. L. Corrigan, A. M. Macdonald, K. J. Noone, L. M. Russell, W. R. Leatich, and A. K. Bertram. Size-resolved observations of refractory black carbon in cloud droplets at a marine boundary layer site, *Atmospheric Chemistry and Physics Discussion*, 14: 11447-11491, 2014.

- I formulated the research questions in collaboration with my supervisor.
- I calibrated, optimized, operated, and maintained two SP2s throughout the duration of this field study.
- I performed all of the data analysis in this publication with exception to the back trajectory model simulations, refractory black carbon coating thick-

ness, and aerosol mass fraction analysis.

- I prepared all of the figures in this publication, with exception to Figure 4.3 showing the back trajectory analysis.
- Writing of the text for this publication was in collaboration with my supervisor.
- Contributions from co-authors:
  - Dr. S. Hanna performed the HYSPLIT back trajectory model simulations and provided the data used for the refractory black carbon coating thickness analysis.
  - Dr. R. Modini and A. Corrigan provided the HR-ToF-AMS data used for the aerosol mass fractions analysis as well as the SEMS bulk aerosol particle count data.
  - Dr. K. Noone provided consultation on the theory and calculations performed on the counteflow virtual impactor.
  - Dr. R. Leaitch provided consultation on the cloud microphysics for the clouds reported in this chapter.

Chapter 5 (first author of a journal article in preparation for submission to a peer-reviewed journal) J. C. Schroder, S. J. Hanna, S. Sharma, S. Sjostedt, K. J. Noone, A. M. Macdonald, W. R. Leaitch, and A. K. Bertram. Size-resolved observations of refractory black carbon particles in cloud droplets at a Canadian high elevation site, 2014.

- I formulated the research questions in collaboration with my supervisor.
- I calibrated, optimized, operated, and maintained one of the SP2s used during this field study.
- I performed all of the data analysis in this publication with exception to the back trajectory model simulations.
- I prepared all of the figures in this publication, with exception to Figure 5.2 showing the back trajectories analysis.
- Writing of the text for this publication was in collaboration with my supervisor.
- Contributions from co-authors:
  - Dr. S. Sharma and Dr. R. Leaitch calibrated and operated the second SP2 used during this field study.
  - Dr. S. Hanna performed the HYSPLIT back trajectory model simulations for this publication.
  - Dr. S. Sjostedt performed the data analysis for the acetonitrile measurements
  - Dr. K. Noone provided consultation on the theory and calculations performed on the counteflow virtual impactor.
  - Dr. R. Leaitch provided consultation on the cloud microphysics for the clouds reported in this chapter.

Chapter 6 (second author of a journal article in preparation for submission to a peer-reviewed journal) S. J. Hanna, J. C. Schroder, A. M. Macdonald, W. R. Leaitch, and A. K. Bertram, Measurements of refractory black carbon at the Whistler high elevation site from 2009-2012, 2014

- I calibrated, optimized, operated, and maintained the SP2s used in the 2010 and 2012 datasets.
- Dr. S. Hanna and I shared the data analysis for this manuscript. Specifically, I performed the initial data analysis used in the size distributions and mass concentration analysis reported in the manuscript.
- I prepared all the figures and tables within this chapter.
- Writing of the text for this chapter was in collaboration with Dr. S. Hanna and my supervisor.

Table of Contents

List of Tables

List of Figures

List of Symbols

A	amplitude of SP2 scattering signal
AF	activated fraction
a_w	water activity
B	baseline offset for Gaussian distribution
C	fraction of CVI orifice outer radius used in Equation 4.4
CF	size-resolved instrument sensitivity correction factor
$CVI - D_{50}$	CVI cut-size
D	cloud droplet diameter
D_g	lognormal distribution mean parameter
D_p	dry particle diameter
D_{pc}	critical activation diameter
D_{stop}	droplet stopping distance within CVI

DT	droplet transmission factor through CVI
EF	CVI enhancement factor
ε	constant used in Equation 4.5 (0.158)
η_{air}	viscosity of air
$F1$	CVI counterflow
$F2$	CVI sample flow
i	i^{th} component
κ	hygroscopicity parameter
κ_{Bulk}	hygroscopicity parameter for internally mixed particle
λ	wavelength
L_{cur}	length of gas stream lines curving around CVI probe tip
L_{min}	length from the CVI probe tip to the top of the porous frit
L_{por}	length from the top of the CVI porous frit to the end of the stagnation plane
L_{stag}	overall length to the end of the stagnation plane
M_{Res}	residual particle mass concentration
M_{Tot}	total (residual + interstitial) particle mass concentration

M_w	molecular weight of water
μ	Gaussian distribution mean parameter
μ_{sp2}	center of the SP2 laser beam
m/z	mass to charge ratio
n	number of moles
N_{Res}	residual particle number concentration
N_{Tot}	total (residual + interstitial) particle number concentration
R	universal gas constant
r_d	cloud droplet radius
r_i	inner radius of CVI orifice
r_o	outer radius of CVI orifice
Re_d	droplet Reynolds number
ρ_{air}	density of air
ρ_d	droplet density
ρ_w	density of water
ρ_{bc}	density of black carbon

σ	Gaussian distribution width parameter
σ_{sp2}	width of SP2 laser beam
σ_g	lognormal distribution width parameter
$\sigma_{s/a}$	surface tension at the air/surface interface
σ_{std}	standard deviation
σ_w	surface tension of water
S	supersaturation
S_C	critical supersaturation
T	temperature
t	time
υ	volume fraction
V_∞	air intake velocity of CVI
VED	volume equivalent diameter
X	length of CVI porous frit
x	SP2 peak height

List of Abbreviations

ABL	atmospheric boundary layer
ACSM	aerosol chemical speciation monitor
APD	avalanche photodiode
a.g.l.	above ground level
a.m.s.l.	above mean sea level
BC	black carbon
$\text{BulkAero}_{\text{Res}}$	residual bulk aerosol (entire aerosol population, including BC)
$\text{BulkAero}_{\text{Tot}}$	total (residual + interstitial) bulk aerosol (entire aerosol population, including BC)
CCN	cloud condensation nuclei
CDNC	cloud droplet number concentration
CPC	condensation particle counter

C-ToF-AMS	C-mode time-of-flight aerosol mass spectrometer
CVI	counterflow virtual impactor
CWFIS	Canadian wildland fire information system
DMA	differential mobility analyzer
FT	free troposphere
FM	fog monitor
HIPPO	HIAPER pole-to-pole observations
HR-ToF-AMS	high-resolution time-of-flight aerosol mass spectrometer
HYSPLIT	hybrid single particle Lagrangian integrated trajectory model
IPCC	Intergovernmental Panel on Climate Change
LEO	leading edge only
LWC	liquid water content
MODIS	moderate resolution imaging sprectroradiometer
NOAA	National Oceanic and Atmospheric Administration
OM	organic aerosol, or matter
OPC	optical particle counter

PDT	pacific daylight savings time
PMT	photomultiplier tube
PSL	polystyrene latex bead
PST	pacific standard time
rBC	refractory black carbon
rBC_{Res}	residual rBC particles
rBC_{Tot}	total (residual + interstitial) rBC particles
SEMS	scanning electrical mobility spectrometer
SMPS	scanning mobility particle sizer
SP2	single particle soot photometer
$SP2_{Res}$	SP2 measuring residual particles
$SP2_{Tot}$	SP2 measuring total (residual + interstitial) particles
UHSAS	ultra-high sensitivity aerosol spectrometer
WACS	Whistler aerosol and cloud study
WHI	Whistler high elevation site
WPS	wide range particle spectrometer

Acknowledgments

A dissertation that focuses on field measurements of atmospheric aerosols takes an immense amount of effort from a great number of individuals. None more so than my advisor, Dr. Allan Bertram, who provided an open atmosphere for me to begin learning the complex field of atmospheric chemistry and grow as a scientist in general. Allan, I appreciate the direction you provided, your patience in my ignorance, and the knowledge you imparted as I journeyed through the muddled waters of black carbon cloud interactions.

To all the past and present Bertram group members: Emily, Pedro, Donna, Michael, Sarah, Yuan, Meng, MiJung, Stephan, Song, Aidan, Rich, Lyndsay, Vickie, Yuri, Cédric, Ryan, and James, thank you for helping to create a work environment that was fun, stimulating, and most of all memorable. I would like to especially thank Emily, Sarah, Pedro, and Michael who received the brunt of my incessant questioning. I am forever indebted to all of you for the kindness, patience, and knowledge each of you shared with me.

All of the work presented in this dissertation would not have been possible without the help and expertise of all the field campaign contributors, of which

there are too many to list, but I thank each and everyone of you for your contribution and for helping me accomplish this immense task. I would like to particularly thank Richard for everything you taught me in the field and your invaluable mentorship along the way, and Anne Marie, for your insight into CVIs and for doing anything and everything in your power to collect the best dataset possible. For spending hours with me on the phone diagnosing SP2 detector issues, and in general, helping me understand the complex world of SP2 measurements, I would like to thank Subu. Finally, to Rob and Ran who spent hours with me holed up in a shipping container at ungodly hours of the night, thanks for the entertainment and friendships that have ensued.

A most special appreciation goes to my mother, Patricia Schroder, who instilled in me, at a very early age, that I can accomplish anything I set my mind to. Mom, assuming all goes well here, this is just another testament to the constant support and unconditional love you've shown me over the years, regardless of my endeavor. Without this I would not be the person I am today and only exemplifies what a wonderful person and amazing mother you truly are. Also, to my late uncle, Mr. Ron Gill, without whom none of this would have come to fruition. Ron, you plucked me from a path that was surely headed for despair and showed me that the world is a beautiful place. I wholeheartedly believe that it was through this that I have ended up where I am today, a doctoral candidate in atmospheric chemistry.

To my children, Dillon and Zoë, you have brought so much joy into my life that words could never justify. Dillon, throughout this journey you have taught

me, and continue to teach me, the virtue of patience. Your humor often reminds me that life doesn't always have to be serious and sometimes playing catch with you is way more important than analyzing data. To my precious little Zoë girl, your constant source of undying affection has picked me up more times than I can count, and your thoughtful nature never ceases to amaze me from such a young girl. To both of you, I am eternally grateful, and if there is one thing I hope you've learned by watching me go through this, is that you too can also accomplish anything if you put your mind to it.

Finally, to the love of my life, Mrs. Lisa Schroder. What you have sacrificed for me to accomplish this task will take me multiple lifetimes to repay. Your never-ending support, pursuit for harmony, calm nature, warm hugs, and acceptance are just a few of your traits that have been my rock. It is because of you that all of this was possible, and as a result, I hereby grant you the most distinguished award (created by your late father) of PhT (Put him Through). Luv, I am so thankful for everything you've given to me. There is no one else on the planet I would have rather endured this with than you!

To my wife, Lisa, son, Dillon, and daughter, Zoë who are constant reminders that in the pursuit of becoming a better person there is no time like right now.

Chapter 1

Introduction

1.1 The Atmosphere

The Earth‘s atmosphere is divided into several layers as seen in Figure 1.1 top panel, which shows a temperature profile as a function of altitude that typically occurs near midlatitude regions (between approximately 23° and 66° for both hemispheres) (Wallace and Hobbs, 2006). The troposphere is the bottom layer and is characterized by a decrease in temperature with an increase in altitude. This layer contains approximately 85% of the total mass within the atmosphere (Jacob, 1999), and extends from the Earth's surface to approximately 11 km (depending on latitude). The troposphere can be further classified into two regions known as the atmospheric boundary layer (ABL) and the free troposphere (FT) (Figure 1.1 bottom panel). The ABL is the lowest portion of the troposphere, typically from 0-1 km, where the frictional forces of the Earth's surface acting on wind direction

and velocity are greatest, causing turbulent vertical mixing of atmospheric components (Stull, 2003). The altitude at which the Earth's frictional forces on wind direction and velocity diminish is called the FT. Within the FT vertical mixing is slow (Stull, 2003).

The atmosphere is made up of gaseous, liquid, and solid materials that are emitted from both natural and anthropogenic sources (e.g. volcanic eruptions, dust storms, forest fires, and vehicular exhaust). It is within the troposphere that these components can most greatly influence the quality of life for humans by altering such parameters as visibility, or air quality, which in turn can impact human health. All of the work performed in this document takes place in the troposphere.

1.2 Aerosols

The liquid and solid components, mentioned above, are referred to as particulate matter, or aerosol when that particulate matter is suspended in a gaseous medium (Finlayson-Pitts and Pitts, 2000), such as air. Although the rigorous definition of aerosol accounts for both the particles and the gas it is suspended in, it is common in atmospheric literature to use the word aerosol and particle interchangeably. Therefore, for the remainder of this dissertation the word aerosol will refer to the particles alone, without reference to the gas. Aerosols are ubiquitous in the atmosphere and exist in a wide range of sizes, number concentrations, and chemical compositions. The exact chemical and physical properties of aerosol particles are governed by the source of emission and any chemical, or physical changes that

occur while the particles are suspended in the atmosphere.

Aerosols within an air mass can exist in different mixing states. The mixing state describes the extent to which multiple different aerosols from different sources have been atmospherically processed to form internal mixtures of composition within a single aerosol. The two extreme cases of mixing state are classified as externally mixed and internally mixed. Externally mixed aerosols exist when aerosols from multiple sources are present in the same air mass as independent particles with chemical compositions that are characteristic of the initial source. Alternatively, several aerosols from different sources can be combined into a single aerosol particle through processes such as coagulation or condensation. These are considered to be internally mixed as the chemical composition of a single particle is now a mixture of species from each of the different sources. For example, a black carbon particle that has had ammonium sulfate condensed on its surface is considered to be an internally mixed particle.

The presence of complex mixtures of aerosols that have different sizes, chemical compositions, and mixing states within a given air mass creates a dynamic system in which atmospheric gases and aerosols interact under different meteorological conditions (e.g. temperature, pressure, relative humidity). Variations in the meteorological conditions as well as the size and chemical composition of the aerosols are important parameters as they greatly affect the amount of time an aerosol spends suspended within the atmosphere (Seinfeld and Pandis, 2006), referred to as the lifetime of an aerosol. The greater the aerosol‘s lifetime, the greater the impact it can have on climate (see Section 1.4 for further discussion).

1.3 Black Carbon

Black Carbon (BC) is a subset of the aerosol population that is emitted as a result of incomplete combustion. Historically, the term BC has not had a standardized definition and has been used, in the literature, to represent various components of the total carbonaceous material present in the atmosphere (Bond et al., 2013; Petzold et al., 2013). Here, I adopt the recommendations laid out by Bond et al. (2013), namely that BC is only produced in flames and is distinguished from other forms of atmospheric carbonaceous material by the following four physical properties:

1. BC strongly absorbs visible light.
2. BC retains its form at high temperatures (referred to as refractory).
3. BC is insoluble in water, organic solvents, and other components of atmospheric aerosols.
4. BC is an agglomerate of small carbon spherules.

Because the measurements of BC contained in this document were carried out with a single particle soot photometer (SP2, see Chapter Chapter 3) I further adopt the convention suggested by Petzold et al. (2013) and refer to the BC measured by the SP2 as refractory black carbon, or rBC.

1.3.1 Black carbon emissions

BC emissions come from both naturally occurring and anthropogenic sources. The only natural source of BC in the atmosphere is biomass burning initiated by natural causes, such as lightning. However, biomass burning BC is also emitted from anthropogenic sources such as wood based cook stoves, or stoves used for heating, as well as the burning of agricultural waste, or prescribe forest fires used in forest management.

Table 1.1 was adapted from Bond et al. (2013), and lists the best-estimates of BC emissions from the year 2000 and the year 1750, which is often used as preindustrial conditions. BC emissions are segregated into those emissions that are associated with anthropogenic energy related BC and open vegetative, or biomass burning emissions (Bond et al., 2013). Approximately 4.8 Tg of BC were emitted in the year 2000 as a result of energy related anthropogenic combustion sources, an 1100% increase from preindustrial conditions. A much smaller yet still significant increase of 180% was observed for open burning BC emission sources. The estimates for open burning listed here however, do not necessarily account for agricultural waste burning due to a lack of direct measurements of such processes (Bond et al., 2013). Combining BC emissions from both sources results in a total increase of BC emissions from preindustrial levels of 436%. However, based on the ranges of total BC emissions estimated from all sources in the year 2000 (shown in parenthesis in Table 1.1) a considerable uncertainty is associated with these estimates. These large uncertainties have also been reported in other studies (e.g. Bond et al., 2004; Koch et al., 2009).

1.4 The Effects of Aerosols on Climate

As mentioned in Section 1.2, aerosols can affect climate, and they can do so directly and indirectly. Figure 1.2 pictorially describes the different affects that aerosols can have on climate.

1.4.1 Radiative forcing

The metric used by atmospheric scientists to quantify a particular aerosol‘s effect on climate is known as radiative forcing. The Intergovernmental Panel on Climate Change (IPCC) defines, in general terms, radiative forcing as “the net change in the energy balance of the Earth’s atmospheric system as a result of some imposed perturbation, such as an aerosol. It is usually expressed in watts per square meter, averaged over a particular period of time, and quantifies the energy imbalance that occurs when the imposed change takes place” (IPCC-AR5, 2013). It is through interactions with solar radiation and clouds that aerosols can impose either a cooling or warming effect on the Earth’s atmospheric system. An aerosol that has a positive radiative forcing is considered to be a warming forcer, while an aerosol that has a negative radiative forcing is considered to be a cooling forcer.

1.4.2 Direct effects on radiative forcing

Aerosols can directly affect climate by absorbing, or scattering incoming solar radiation (Figure 1.2). When incoming solar radiation is scattered by aerosols the net amount of radiation reaching the Earth’s surface is reduced, leading to a negative radiative forcing and cooling of the Earth’s atmospheric system (IPCC-

AR5, 2013). Opposite to scattering, when incoming solar radiation is absorbed by aerosols the energy is emitted in the form of heat, leading to a positive radiative forcing and a warming of the Earth's atmospheric system (IPCC-AR5, 2013).

1.4.3 Indirect effects on radiative forcing

Aerosols can also affect climate indirectly through a variety of interactions with clouds. The indirect effects on climate are classified into two categories; the 1st indirect effect, or cloud-albedo effect, and the 2nd indirect effect, or cloud-lifetime effect. Both of these effects are represented pictorially in Figure 1.2. In order for an aerosol to impact climate indirectly it must have the ability to act as a cloud condensation nuclei (CCN), which is a requirement to form cloud droplets (see Chapter 2 for further details on cloud droplet formation).

The cloud-albedo effect is characterized by an increase in the cloud droplet number concentration (CDNC) as a result of an increase in the number of CCN active aerosols. The cloud-albedo effect assumes the amount of liquid water available remains the same as the clean cloud conditions (see Figure 1.2). The increase in number of CDNC increases the reflectivity, or albedo of the cloud. An increase in the cloud-albedo reduces the net radiation reaching the Earth's surface producing a negative radiative forcing and hence a net cooling effect on climate.

The cloud-lifetime effect, on the other hand, is the result of the decrease in droplet size, as a result of an increase in the number of CCN active aerosols. A decrease in droplet size results in a decrease in the amount of precipitation and therefore, an increase in the lifetime of the cloud. An increased lifetime, in turn,

reduces the amount of solar radiation reaching the Earth's surface also producing a negative radiative forcing.

1.5 Effects of Black Carbon on Climate

1.5.1 Direct effects of black carbon on climate

BC is a strong absorber of all wavelengths of visible light (Bond et al., 2013). In fact, BC is the atmospheric species with the strongest known absorption of solar radiation at these wavelengths (Bond et al., 2013). As a result of such efficient absorption, BC has the potential to significantly influence climate directly. Based on the current best-estimates the BC direct radiative forcing, from all present day sources, is +0.88 W m^{-2}, however this number has a 90% uncertainty. Accounting for this uncertainty places BC direct radiative forcing estimates between +0.17 to +1.48 W m^{-2} (Bond et al., 2013). The uncertainty in the BC direct radiative forcing estimates stems from uncertainties in the emission rates of BC, spatial and temporal distributions of BC, as well as removal rates of BC from the atmosphere through such processes as wet or dry deposition (Bond et al., 2013).

1.5.2 Indirect effects of black carbon on climate

BC particles have been shown to acquire hydrophyilic coatings (Bond et al., 2013). Once coated with a hydrophyilic substance they can become CCN active, and therefore contribute to the indirect effects on climate (Bond et al., 2013). The best-estimates of the indirect radiative forcing of BC, based on current knowledge, is

+0.23 W m^{-2} (Bond et al., 2013). However, similar to the direct radiative forcing estimate, this indirect radiative forcing estimate has a 90% uncertainty associated with it, thus giving a range of -0.47 to +1.0 W m^{-2} (Bond et al., 2013). Bond et al. (2013) remark that it is a lack of scientific understanding in the BC-cloud effects that is the largest source of uncertainty in calculating the contribution of BC to climate change.

1.6 Dissertation Research Goals

To better understand the role of BC in climate, and to better quantify the direct and indirect effects of BC on climate, the incorporation of rBC particles into cloud droplets as a function of rBC particle size was investigated at two locations: 1) La Jolla, CA, and 2) Whistler, BC. Measurements of rBC in cloud droplets as a function of size is important to test our current understanding of the incorporation of rBC particles into cloud droplets and to test our understanding of the CCN properties of rBC. A better understanding of the CCN properties of BC should eventually translate to better estimates of the direct and indirect effects of BC on climate.

In addition to investigating the incorporation of rBC in cloud droplets, this thesis also describes measurements of rBC at the Whistler High Elevation Site (WHI) conducted during 2009, 2010, and 2012. This included measurements of rBC from biomass burning and rBC in the free troposphere. From these studies, properties of rBC, such as coating thickness and size distributions, that are needed when calculating the direct effect of rBC on climate were determined. The three

year record also serves as a bench-mark that can be used to test current atmospheric models that predict concentrations of BC in the atmosphere.

1.7 Overview of Dissertation

Chapter 1 (this chapter) gives an introduction to atmospheric aerosols, including BC, and their potential effect on climate. It also outlines the research goals of this dissertation. Chapter 2 discusses the theory used to determine if an aerosol will activate to form a cloud droplet, and Chapter 3 describes the operational theory and data analysis procedures for the SP2, the primary instrument used in this research. Chapters 4-6 are the research chapters. For example, Wang et al. (2014) compared modelled BC concentrations with ambient measurements of BC and concluded that most models overestimate atmospheric BC concentrations, likely indicating that activation of BC into cloud droplets is not simulated correctly, and therefore contribute to the uncertainties of the direct and indirect estimates. By directly measuring CCN properties of BC in cloud droplets at two distinct locations, models can be further constrained to more accurately determine the indirect effects of BC on climate.

Chapter 4 investigates the size-resolved activation of rBC measured at a marine boundary layer site during two liquid water cloud events. The size-resolved activated fractions of rBC are compared to the activated fractions of the bulk aerosol, and the average coating thickness of rBC containing particles are also reported and discussed. In addition, the observed activation of rBC at this site is compared with kappa-Köhler theory in order to validate the theory with observa-

tions from a natural environment. Chapter 5 also investigates the size-resolved activation of rBC in liquid water clouds, but at a high elevation mountain site. Comparisons between the size-resolved activated fractions of rBC and the size-resolved activated fractions of the bulk aerosol are also discussed in Chapter 5.

Chapter 6 presents results from a three year period of measurements taken at the high elevation mountain site, and discusses properties (size distributions, mass concentrations and distributions, as well as coating thicknesses) of rBC measured during two types of sampling conditions: 1) during biomass burning episodes and 2) during free tropospheric sampling conditions. Finally, Chapter 7 summarizes the research with some general conclusions and considerations for future work.

1.8 Chapter 1 Figures and Tables

Table 1.1: Best-estimates of BC emissions in Tg yr^{-1} with available estimate ranges in parentheses (adapted from Bond et al. (2013) Table 6). Energy related estimates are from energy-related combustion sources while open burn refers to open vegetative, or biomass burning estimates.

Time frame	BC Emissions
Year 2000	
Energy related	4.8 (1.2-15)
Open burning	2.8 (0.8-14)
Total	7.5 (2-29)
Year 1750	
Energy related	0.4 (-)
Open burning	1.0 (-)
Total	1.4 (-)

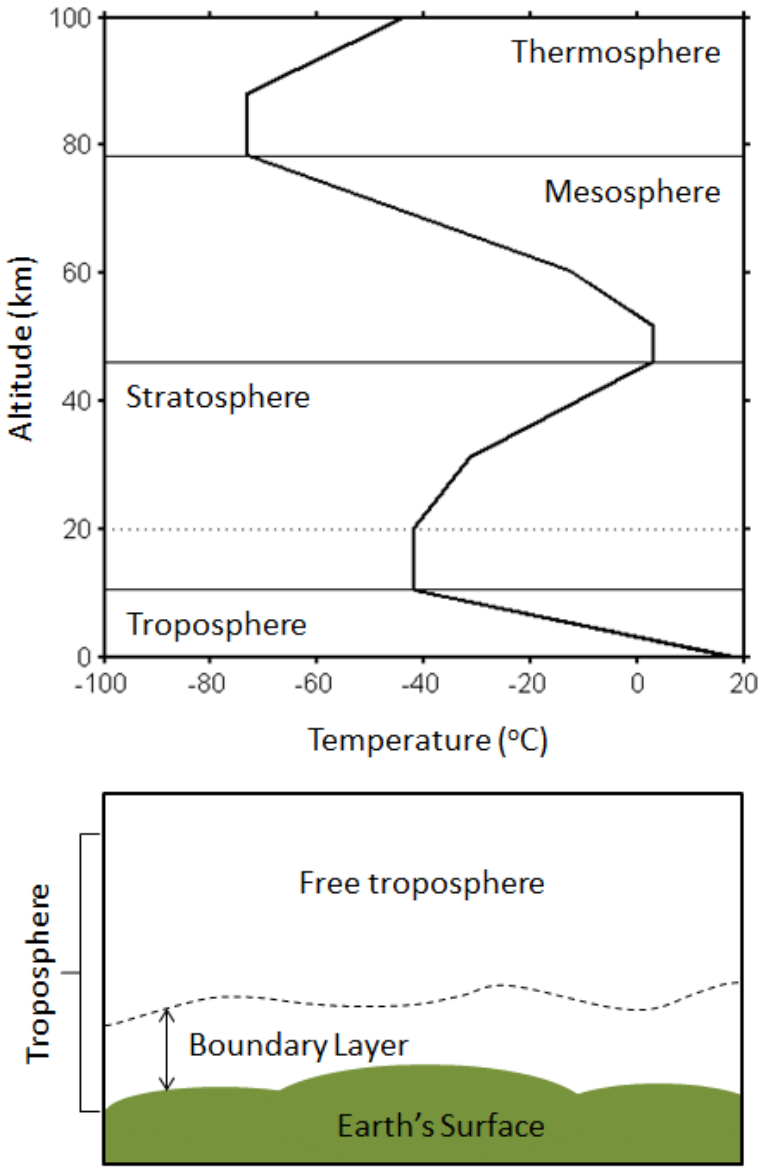

Figure 1.1: Vertical structure of the atmosphere (top panel) for a typical mid-latitude temperature profile (adapted from Wallace and Hobbs (2006)), and a schematic showing the components of the troposphere (bottom panel).

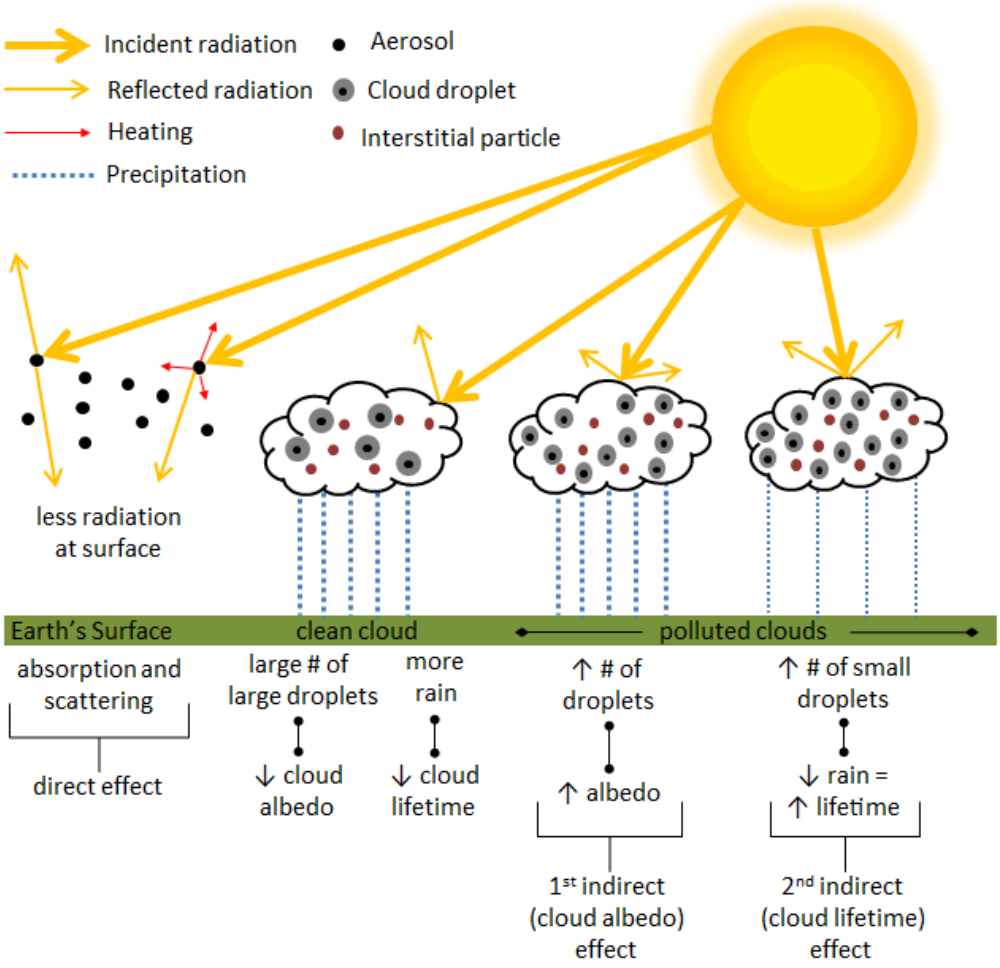

Figure 1.2: Schematic showing the different mechanisms by which aerosols can affect climate (adapted from IPCC-AR4 (2007) Figures 2.10 and 7.20). The thickness of the lines represent the magnitude of the radiation.

Chapter 2

Formation of Cloud Droplets and kappa-Köhler Theory

2.1 Introduction

Given the numerous pathways by which aerosols can interact with clouds to affect climate, it is important to determine a given aerosol's ability to act as a CCN (see Section 1.4.3). The following section describes the details of how Köhler theory can be used to determine if an aerosol will act as a CCN, and provides the necessary background theory for the rBC cloud studies described in Chapters 4 and 5.

2.2 Theory Describing Droplet Formation for Insoluble Particles Coated with Soluble Material

The supersaturation of water vapor (S) over a droplet containing a dissolved solute can be described by the following equation (Seinfeld and Pandis, 2006):

$$S = \left[a_w exp\left(\frac{4\sigma_{s/a} M_w}{RT\rho_w D} \right) - 1 \right] x100, \tag{2.1}$$

where a_w is the activity of water in a solution, $\sigma_{s/a}$ is the surface tension of the air/surface interface, M_w is the molecular weight of water, R is the universal gas constant, T is temperature, ρ_w is the density of water, and D is the droplet diameter. S is the supersaturation and is defined as the saturation minus one and is usually expressed as a percent. For example, a supersaturation, S, of 1% corresponds to a relative humidity of 101%. A more convenient form of Equation 2.1 that incorporates a single hygroscopicity parameter kappa (κ) for the aerosol (Petters and Kreidenweis, 2007), has been widely adopted (e.g., Chang et al., 2010; Dusek et al., 2011; Moore et al., 2012; Petters et al., 2009; Prenni et al., 2007; Rose et al., 2010), and can be expressed as:

$$S = \left[\frac{D^3 - D_p^3}{D^3 - D_p^3(1-\kappa)} exp\left(\frac{4\sigma M_w}{\rho_w RTD} \right) - 1 \right] x100, \tag{2.2}$$

where D is still the droplet diameter; D_p is the dry particle diameter; σ is the droplet surface tension, and is assumed to be that of water (0.072 J m^{-2}); and κ is a compositionally specific parameter that describes an aerosol's hygroscopic-

ity. For a complex internally mixed aerosol particle, such as an insoluble particle coated with soluble material, the hygroscopicity of the entire particle (κ_{Bulk}) can be calculated by following a simple mixing rule as follows:

$$\kappa_{Bulk} = \sum_i \upsilon_i \kappa_i, \tag{2.3}$$

where υ_i is the volume fraction and κ_i is the hygroscopicity parameter of the i^{th} component present in an internally mixed aerosol (Petters and Kreidenweis, 2007). A large value for κ_{Bulk} would indicate a strongly hygroscopic aerosol that would therefore be an efficient CCN.

At a constant D_p, Figure 2.1 can be used to evaluate the relationship between S and droplet growth. Figure 2.1 panel A shows an example of this relationship for ammonium sulfate, a ubiquitous atmospheric aerosol, where supersaturation is plotted as a function of droplet diameter. Equation 2.2 panel A is often referred to as a Köhler curve. The maximum of the Köhler curve for a given dry diameter of an aerosol with hygroscopicity κ represents the minimum, or critical supersaturation (S_C) required for that specific aerosol to be activated into a cloud droplet. At any supersaturation $\geq S_C$ the droplet will continue to grow indefinitely, or at least until it grows large enough to rain out. S_C can be determined from Equation 2.2 as a function of aerosol dry diameter, to produce a plot similar to that shown in Figure 2.1 panel B. In this figure, S_C is plotted as a function of aerosol dry diameter for ammonium sulfate using a κ value of 0.61 (Petters and Kreidenweis, 2007). Figure 2.1 panel B can then be used to predict the minimum, or critical dry

diameter (D_{pc}) of an aerosol with hygroscopicity κ that will act as a CCN, if S of the cloud is known. Alternatively, if the D_{pc} is known, in a given cloud for a given aerosol species, a plot similar to that in Figure 2.1 panel B can be used to predict the maximum S_C reached in the cloud.

In summary, kappa-Köhler theory can be used to predict whether or not an aerosol with a given diameter and hygroscopicity will activate to form a cloud droplet at a given S. However, Figure 2.1 panel B also indicates that for a given aerosol at a constant S not all sizes of that aerosol will activate to form droplets. As an example, if ammonium sulfate were exposed to a supersaturation of approximately 0.2% all diameters $\geq\approx$90 nm would activate, while all diameters $<$ 90 nm would not activate to form cloud droplets. Therefore, a cloud will have both activated particles, which have particles incorporated into cloud droplets, as well as non-activated particles referred to as interstitial particles. This is represented pictorially in Figure 1.2, where the cloud droplets are represented by grey circles with smaller black circles inside, and the interstitial particles are represented by small red circles.

2.3 Chapter 2 Figures

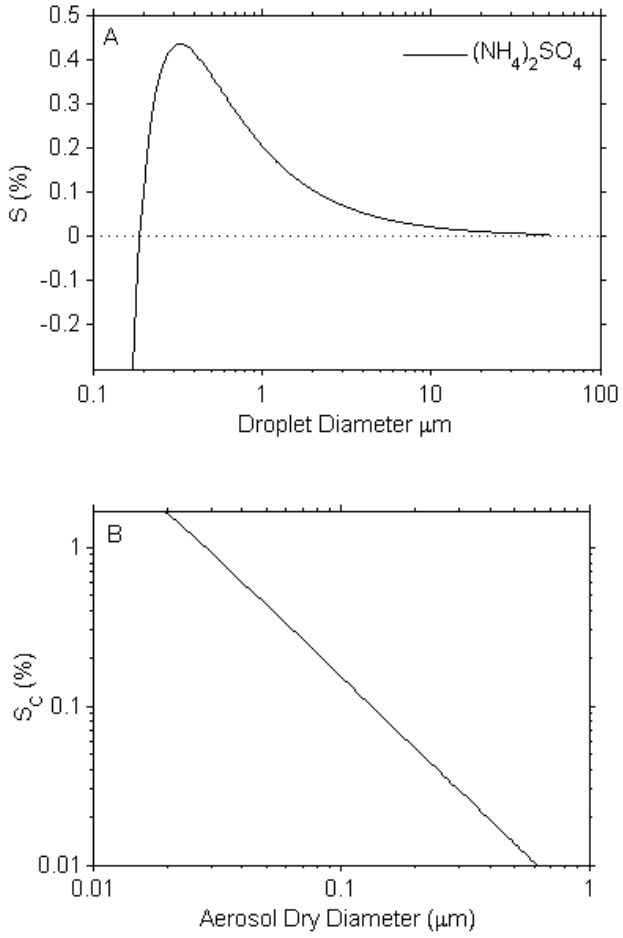

Figure 2.1: Panel A is an example Köhler curve for a 50 nm dry $(NH_4)_2SO_4$ particle using a κ value of 0.61 (Petters and Kreidenweis, 2007). Panel B is the critical supersaturation (S_C) as a function of ammonium sulfate dry diameter.

Chapter 3

Single Particle Soot Photometer

3.1 Introduction

The primary instrument used to measure the mass, number and coating properties of rBC, throughout all of the research chapters in this dissertation, was a single particle soot photometer (SP2). Since the SP2 was the principal instrument used throughout the course of this thesis work, the following sections describe in detail the SP2 theory of operation and procedures for data analysis.

3.2 Theory of Operation

The SP2 (Droplet Measurement Technologies, Boulder, CO) is a commercially manufactured instrument designed to measure the mass of individual rBC particles via laser induced incandescence (Stephens et al., 2003). A schematic of the SP2 is shown in Figure 3.1. The instrument is comprised of an aerosol inlet, an in-

tracavity laser and four detectors. Ambient aerosol particles are drawn in through the aerosol inlet at a flow rate of $\approx$ 120 cm^3 min^{-1} and introduced into a high intensity ($\approx$ 1 MW cm^{-2}), intracavity, continuous Nd:YAG laser beam. A diode laser, operating at a wavelength (λ) of 808 nm, is used to pump a Nd:YAG doped crystal to produce laser light with an output λ=1064 nm in a TEM00 mode. Once an aerosol particle intersects the intracavity laser, two events can occur: 1) the particle can elastically scatter light and/or 2) the particle can absorb laser light. By measuring the elastically scattered light and by measuring the incandescence of the particle due to absorbed laser light, the SP2 can be used to obtain the rBC mass, rBC volume equivalent diameter (VED), and the thickness of any coating surrounding individual rBC particles. Each of these measurements is discussed in further detail in Sections 3.3 to 3.5 below.

Two types of SP2s were used during the field studies discussed in this dissertation. One is a four channel instrument, which records either a low-gain, or a high-gain signal for each of the four detectors shown in Figure 3.1 at any given time. The second type of SP2 is an eight channel instrument that simultaneously records both the high and low gain signals for each of the four detectors shown in Figure 3.1, thus extending the size and mass detection limits. The detection limits for each of the specific SP2s used during the experiments discussed in this dissertation will be addressed in the corresponding chapters for which they were used.

3.3 Mass Calibration

If a particle efficiently absorbs at λ=1064 nm, such as rBC, it will rapidly heat to it's vaporization, or boiling point, temperature ($\approx$ 4000K for rBC) as it traverses the laser beam profile. Once a rBC particle reaches its boiling point temperature, incandescence occurs, and the visible light emitted is recorded by two Photomultiplier Tubes (PMT), labeled 'Ch1 PMT Broadband Incandescence' and 'Ch2 PMT Narrowband Incandescence' in Figure 3.1. The incandescence signals measured by the SP2 are only from the refractory portion of black carbon. Both of the incandescent PMT detectors are positioned to collect light over a solid angle of $\approx$ π/2 sr. The broadband incandescent detector is optically filtered to collect light with wavelengths between approximately 350 to 800 nm, whereas the narrowband incandescent detector is filtered to only collect light between wavelengths of 630 to 800 nm. The ratio of the broadband to narrowband signal can be used to extract the boiling point temperature by utilizing the theory of two-color pyrometry (Schwarz et al., 2006; Stephens et al., 2003). The boiling point temperature is characteristic of the absorbing species and can be used as a means of particle identification. However, since BC is considered to be the only species in the atmosphere that absorbs in the near-IR and gives a significant incandescence signal at the wavelengths measured, all incandescent signals used in the analysis included in this dissertation were taken to be from rBC (McMeeking et al., 2010; Schwarz et al., 2006).

The amplitude of the signal recorded by the incandescent detectors is propor-

tional to the mass of rBC in a particle. The signal and rBC mass are related through a calibration curve created using a known reference material (see Figure 3.2 as an example). All SP2s used in this study were calibrated with a reference material recommended by the manufacturer of the SP2. The calibration material is a colloidal graphite called Aquadag® (Moteki et al., 2009). The Aquadag® is first size selected using a differential mobility analyzer (DMA) prior to being sampled by the SP2. Data is recorded for ≈10,000 to 100,000 Aquadag® particles for each particle size selected by the DMA. The baseline corrected maximum signal amplitude, referred to as peak height, of the signal recorded by the broadband incandescent detector is determined for each particle. For a given size selected particle a distribution of peak heights is obtained. In order to find the average peak height for a given size the distribution of peak heights is fit with a Gaussian function.

Once the average peak height for a given size-selected particle is determined, the corresponding mobility diameter is converted to a mass using the size dependent effective densities reported by Gysel and Crosier (2007). The proportionality between broadband incandescent peak height and mass is then determined by fitting a second order polynomial function to the data (Figure 3.2). The fit parameters are then used to convert measured peak heights to mass for rBC particles in the atmosphere.

3.4 Volume Equivalent Diameter

Once the mass is determined, the volume equivalent diameter (VED) for each individual rBC particle can be calculated by assuming a density (ρ_{bc}) of 1.8 g

cm^{-3} (Bond and Bergstrom, 2006) and solving the following equation for VED:

$$Mass = \frac{4}{3}\pi\left(\frac{VED}{2}\right)^3 \rho_{bc}. \tag{3.1}$$

3.5 Refractory Black Carbon Coating Analysis

Upon intersecting the intracavity laser beam, a particle will elastically scatter light, and this scattered light is collected by two avalanche photodiodes (APDs) positioned to capture light over a solid angle of $\approx \pi/2$ sr (Schwarz et al., 2006). These two scattering detectors are both optically filtered to only collect light between wavelengths of approximately 850 to 1200 nm, and are labeled 'Ch0 APD Scattering' and 'Ch3 APD Split Scattering' in Figure 3.1 . The elastically scattered light detected by these two APDs can be used to obtain a measure of any coating thickness on an absorbing rBC particle.

The procedure for determining the coating thickness on a coated rBC particle requires three steps: 1) the amplitude of the scattering signal from a coated rBC particle is determined; 2) a relationship between the calculated Mie scattering amplitude and the SP2 instrument response is established; and 3) a core and shell Mie scattering model is used to determine the coating thickness required to produce the same scattering amplitude as determined in step 1. Each of these steps is discussed in detail below.

3.5.1 Step 1: Determining the scattering amplitude of coated refractory black carbon particles

Since the SP2 laser beam is in a TEM00 mode and exhibits a Gaussian profile the scattering signal from a non-absorbing (referred to as scattering only) particle that intersects the laser will also exhibit Gaussian behavior, where the maximum amplitude will occur at the most intense region of the beam, which for a Gaussian profile is at the center. As an example, the scattering signal from a theoretical scattering only particle is shown in Figure 3.3 panel A (blue trace), where the maximum amplitude is shown to occur at the center of the beam.

When a rBC particle that has a non-refractive coating, such as sulfate, intersects the laser beam the coating will begin to vaporize before incandescence of the rBC core occurs (Schwarz et al., 2006). Therefore, when the coated particle reaches the center of the laser beam the scattering amplitude no longer represents the scattering produced from a particle with a diameter equal to its core plus its coating. Figure 3.3 panel B shows the SP2 signals recorded from a theoretical absorbing rBC particle, where the scattering signal is shown as a solid blue line, and indicates that the maximum scattering amplitude occurs prior to reaching the center of the beam and therefore no longer represents the true size of the particle being sampled. However, for a short time before the coating begins to vaporize the scattering signal measured does represent the scattering properties of the unaffected coated rBC particle (Gao et al., 2007). Therefore, since the laser beam is fixed in space and has a Gaussian profile the full scattering signal of the coated rBC particle can be reconstructed by using only the leading edge of the measured

scattering signal in order to determine the true scattering amplitude of the particle. This technique is called the leading edge only (LEO) technique and was first implemented, in conjunction with SP2 data, by Gao et al. (2007). The procedure for determining a coated rBC particle's scattering amplitude using the LEO technique is outline below.

3.5.1.1 Leading edge only fitting procedure

The scattering signal from a scattering only particle exhibits Gaussian behavior and is therefore, mathematically represented by the following equation:

$$F(x) = A * exp^{-\left(\frac{x-\mu_{sp2}}{2\sigma_{sp2}}\right)^2} + B, \tag{3.2}$$

where A is the maximum scattering amplitude, and with respect to time, x is the position of a particle within the laser beam at time t, μ_{sp2} is the position of a particle at the center of the beam, σ_{sp2} is the width of the beam, and B is the baseline offset. Since the SP2 laser has a stable Gaussian profile and is fixed in space σ_{sp2} and μ_{sp2} are also fixed and can be characterized by using non-absorbing, purely scattering, polystyrene latex (PSL) beads. The beam width is found by collecting data for 50,000 to 100,000 PSL particles and each signal is fit with a Gaussian function to extract the σ_{sp2} parameter. The average σ_{sp2} from all PSL particles is then used as the fixed beam width.

The incorporation of a split-detector (labeled 'Ch3 APD Split Scattering' in Figure 3.1) has a physical gap in between two detecting surfaces, which provides an absolute positional reference for a particle in the laser beam, relative to the

beam center (Gao et al., 2007). The signal produced by the split-detector from a theoretical particle is shown in Figure 3.3 panels A and B as a sold green line. The scattering signal drops to zero when the scattered light falls on the gap in the detector. The signal shape seen in Figure 3.3 is produced when the initial portion of the scattering signal, prior to crossing the split in detecting surfaces, is digitally inverted in order to determine the position of the particle at the point at which the signal crosses zero (zero-crossing) by means of linear interpolation. Using PSL particles, an average offset of the time from the zero-crossing to the time the particle reaches the center (referred to as the zero-crossing-to-peak time) of the beam can be determined. This offset is then combined with the zero-crossing time of an unknown rBC particle to determine the position at which the maximum scattering amplitude would occur had the coating not volatilized, μ_{sp2}.

The point at which the scattering signal is 5% of the maximum laser intensity occurs defines the last point in the leading edge used to reconstruct the full scattering properties (Gao et al., 2007). Similar to finding the zero-crossing-to-peak time offset the ending point of the leading edge is relative to the zero-crossing, and the constant offset needed can be determined from PSL data.

Once σ_{sp2}, μ_{sp2}, and the leading edge data points are known, Equation 3.2 reduces to a linear function, where the slope represents the amplitude and the intercept is the baseline offset. Thus, using this method the true scattering amplitude of coated rBC can be determined on a single particle level.

3.5.2 Step 2: Relating calculated Mie scattering amplitudes to an SP2 instrument response (i.e. calibration of the elastic scattering detectors)

In Section 3.5.3 a core and shell Mie model is used to predict scattering amplitudes of coated rBC particles. However, prior to using the Mie model, it is necessary to be able to relate the calculated Mie scattering amplitude to the SP2 signal response. This is achieved by collecting data for different sizes of PSL particles and calculating the scattering amplitude as determined by the LEO technique as well as calculating the scattering amplitude by using Mie scattering calculations (Leinonen Mie Code developed by (Mätzler, 2002a,b)). A PSL refractive index of 1.59-0.0i was used in the Mie scattering calculation. Plotting the amplitude as determined by the LEO technique as a function of the amplitude as determined by Mie calculations and fitting the data to a linear function provides the parameters needed to relate the core and shell Mie scattering amplitudes to the SP2 signal response. An example calibration plot is shown in Figure 3.4, where data were only available for two PSL sizes, 200 and 300 nm.

3.5.3 Step 3: Determining the coating thickness of a coated refractory black carbon particle using a core and shell Mie scattering model

For any rBC containing particles sampled by the SP2, the full scattering signal derives from both the rBC core and any coating surrounding the particle. Since the mass of the rBC is known from the incandescence signal (and can be used to calculate the core VED) and the maximum scattering amplitude is determined

from the LEO technique, a core and shell Mie scattering model can be employed to determine what coating thickness would give the scattering amplitude as determined from the LEO technique (Metcalf et al., 2012; Schwarz et al., 2008b). In this work a core and shell Mie scattering model was used to construct a lookup table for core diameters from 60 to 220 nm (in 1 nm increments) and shell thicknesses from 0 to 360 nm (in 1 nm increments). The complex index of refraction used for the core was 1.95-0.79i (Bond and Bergstrom, 2006) and for the shell was 1.5-0.0i, which is consistent with that of dry sulfate or sodium chloride (Metcalf et al., 2012; Schwarz et al., 2008a,b). When calculating coating thicknesses, the particles were idealized as a pure BC core uniformly coated with a non-absorbing material, although the actual particle morphology may be more complicated (Sedlacek et al., 2012). The calculated amplitudes determined from the core and shell Mie scattering model were all scaled by the calibration plot shown in Figure 3.4.

3.5.4 SP2 optical detection limits and the implications for determining average coating thickness

The optical detection limits of the SP2 impose some restrictions on determining average coating thickness across the full range of rBC core sizes that can be measured by incandescence. These optical detection limits impose restrictions on the coating analysis for both small and large rBC-containing particles.

For small particles, although the incandescence measurements can size rBC cores down to $\approx$ 70 nm, the SP2 optical detection limit means that scattering from bare rBC cores below $\approx$ 100 nm cannot be measured. As particle size decreases

below 100 nm, thicker and thicker coatings are required to produce a measurable scattering signal. As a result, particles with smaller rBC cores and thin or no coatings have no scattering signal that can be used in the LEO fitting procedure and the coating thickness on them cannot be determined. In this analysis any particle with no measurable scattering was assumed to have a coating thickness of 0 (i.e. they were assumed to be bare rBC cores). As a result of this assumption, the average coating thickness reported for particles below 100 nm is a lower limit.

For large rBC cores the optical detectors become saturated when even relatively modest coatings are present. For example, the scattering from a 220 nm rBC core with a coating thickness of 40 nm would saturate the SP2 optical detector. Since the contribution from particles with large scattering signals is not included in the calculation of average coating thickness, it follows that the coating thickness for particles larger than $\approx$ 100 nm is considered an underestimation.

3.6 Chapter 3 Figures

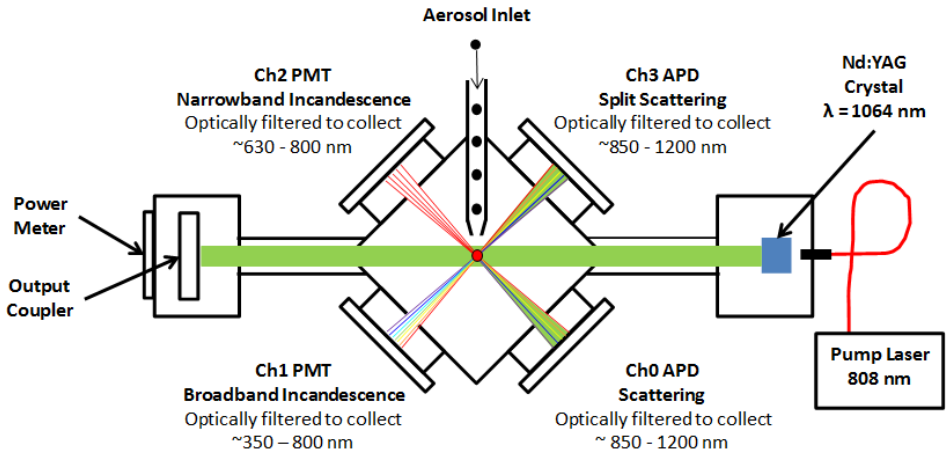

Figure 3.1: Schematic of the SP2 showing the three main components: 1) aerosol inlet; 2) intracavity laser; and 3) the two scattering and two incandescence detectors.

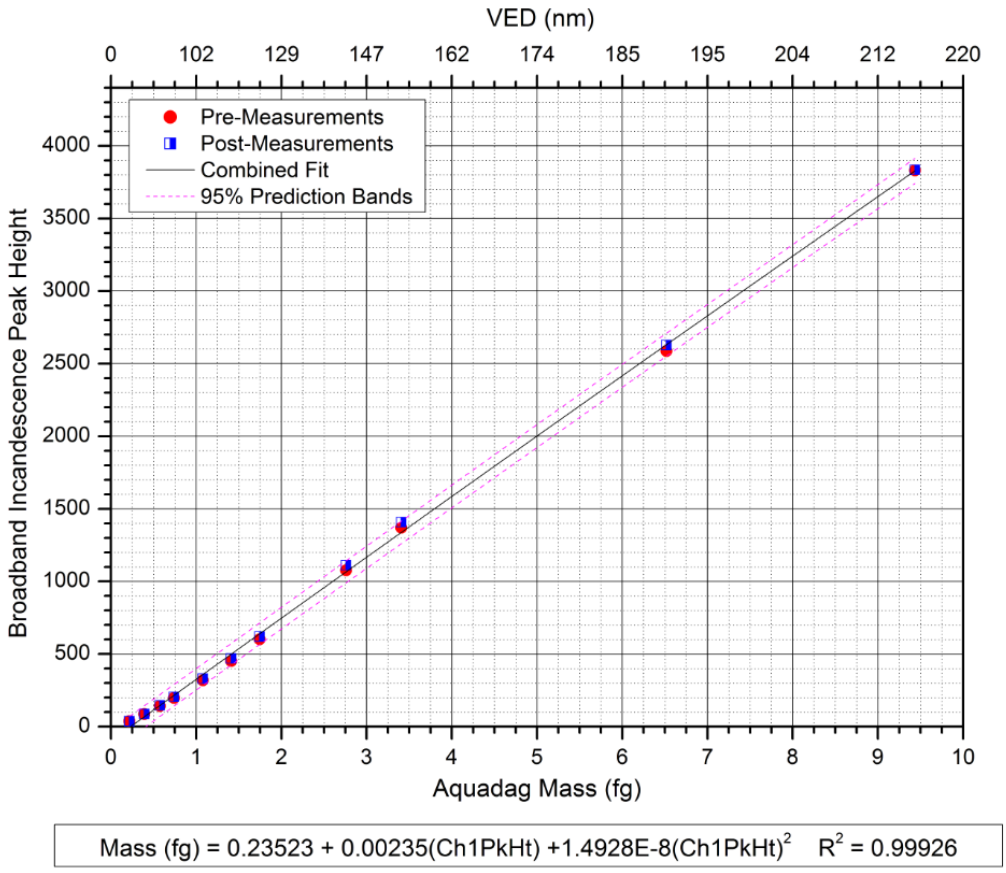

Figure 3.2: Example mass calibration plot for the broadband incandescence channel of the SP2. This plot was created from pre (red circles) and post (blue squares) campaign Aquadag data collected on one of the SP2s used in Chapter 4. The calibration data was fit to a second order polynomial function (solid black line) for the combined pre and post measurement data to create the equation used to determine the mass of an unknown rBC particle (shown in the box below the plot). Also shown are the 95% prediction bands (pink dashed lines) corresponding to the polynomial fit. The X axis is plotted in terms of Aquadag mass on the bottom axis and in terms of volume equivalent diameter (VED) on the top axis.

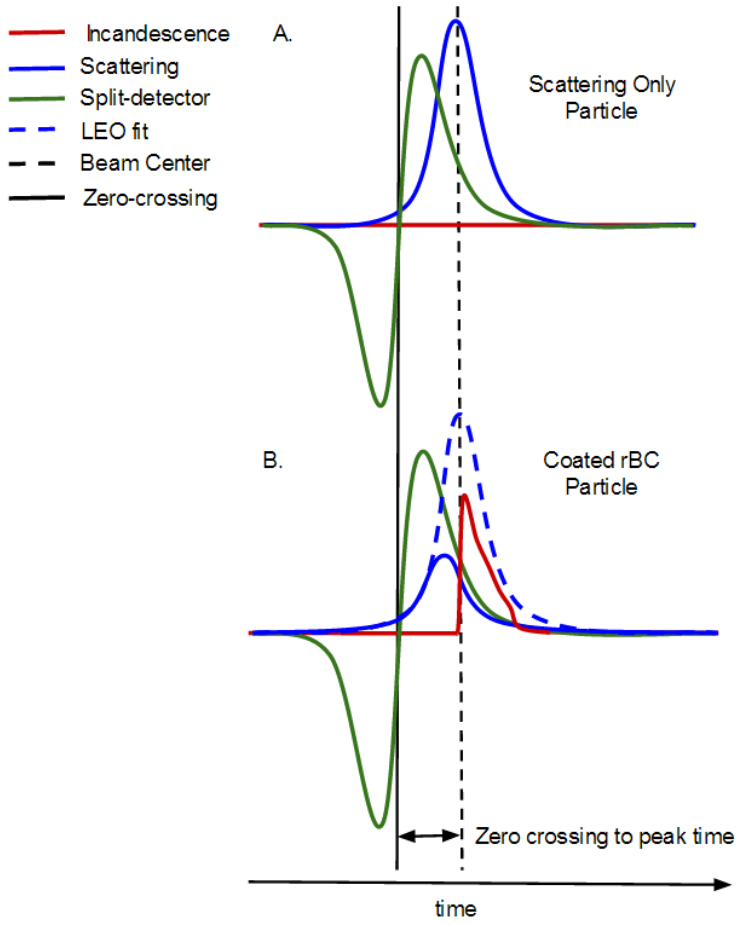

Figure 3.3: Raw signals produced by the SP2 from a theoretical scattering only particle in panel A and a theoretical coated absorbing rBC particle in panel B. For both particle types, the signals recorded from the broadband incandescence detector (red lines), scattering detector (blue lines), and split-detector (green lines) are shown. The reconstructed leading edge only (LEO) scattering signal (blue dashed line) is also shown in panel B. The center of the laser beam is represented by the black dashed line and the point at which the signal recorded from the split-detector crosses zero is indicated by the solid black line.

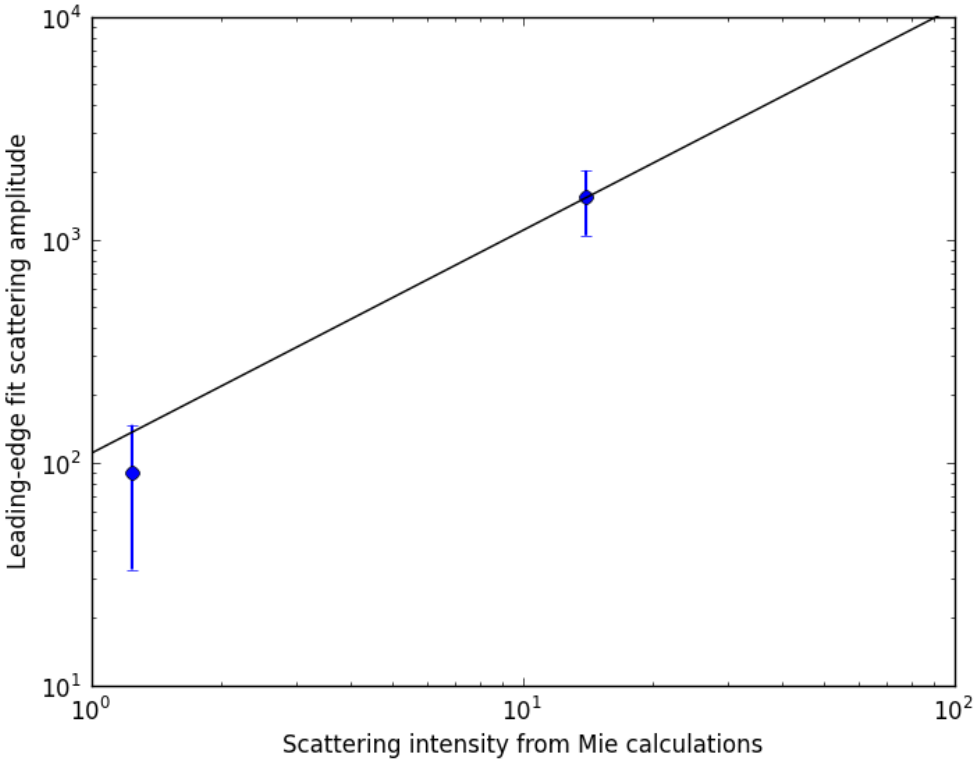

Figure 3.4: An example calibration plot for the elastic scattering detector created from 200 and 300 nm PSL particles. Each data point is the median of $\approx$ 25,000 particles and the error bars indicate one standard deviation. The black line is a linear fit with a forced intercept at zero.The units for both axes are arbitrary.

Chapter 4

Size-Resolved Observations of Refractory Black Carbon Particles in Cloud Droplets at a Marine Boundary Layer Site

4.1 Introduction

BC particles, which typically have sizes less than 1 μm, are emitted into the atmosphere through incomplete combustion of fossil fuels or biomass burning (Bond et al., 2013) (see Section 1.3) . When first emitted into the atmosphere these particles are thought to mainly be hydrophobic. During their atmospheric lifecycle hydrophillic substances, such as sulfate or water soluble organics, can form a coat-

ing surrounding the BC cores (Ching et al., 2012; Metcalf et al., 2012; Schwarz et al., 2008b), enabling the particles to act as CCN (see Chapter 2). Modeling studies have shown that this process can occur in the boundary layer on the order of hours during the daytime (Riemer et al., 2004, 2010).

By absorbing solar radiation or by acting as CCN, BC particles can influence climate both directly and indirectly (see Section 1.5 and Bond et al. (2013); Wang (2013); Wang et al. (2013); Zhuang et al. (2010)). To predict both the direct and indirect effects of BC on climate, a good understanding of the CCN ability of BC is needed (Koch et al., 2011; Vignati et al., 2010; Wang, 2013). When describing the CCN properties of BC in atmospheric models, different approaches have been applied. Often BC is initially assumed to be CCN inactive and is converted to a CCN active species after a prescribed time and at a constant efficiency (Koch et al., 2011; Vignati et al., 2010; Wang, 2013). Alternatively, the CCN properties of particles containing BC in models have been described by Köhler theory (see Chapter 2 and Ching et al. (2012); Jacobson (2012); Koch et al. (2011); Riemer et al. (2010)) .

The CCN ability of BC particles has been studied in both laboratory and field studies (Cozic et al., 2007; Dusek et al., 2011; Hallberg et al., 1992, 1994; Henning et al., 2010, 2012; Hitzenberger et al., 2000, 2001; Kasper-Giebl et al., 2000; Koehler et al., 2009; Kuwata et al., 2009; Noone et al., 1992; Petters et al., 2009; Petzold et al., 2005; Popovicheva et al., 2011; Sellegri et al., 2003; Verheggen et al., 2007). Laboratory studies have examined both coated and uncoated BC particles (Dusek et al., 2011; Henning et al., 2010, 2012; Koehler et al., 2009;

Petters et al., 2009; Petzold et al., 2005; Popovicheva et al., 2011). These studies have shown that for uncoated flame or spark generated BC the particles are not activated into cloud droplets even with supersaturations of $\geq 1\%$ (Henning et al., 2012). On the other hand, once BC is coated with hygroscopic material the supersaturation required for activation is significantly decreased, a decrease that can be described under laboratory conditions by Köhler theory (Chapter 2 and (Henning et al., 2010, 2012; Petzold et al., 2005; Popovicheva et al., 2011)). Field measurements of the activated fraction of BC in cloud droplets have also investigated the CCN ability of BC particles. Most measurements have shown that as BC particles age in the atmosphere the fraction incorporated into cloud droplets increases (Cozic et al., 2007; Hitzenberger et al., 2000, 2001; Kasper-Giebl et al., 2000; Sellegri et al., 2003; Verheggen et al., 2007). An exception to this trend is the work done by Granat et al. (2010) which showed that after several days of travel in the winter subtropical marine environment, soot retained much of its hydrophobic properties. However, the conclusions stated in this study assumed that hygroscopicity controlled the removal of BC through wet scavenging, when a more important factor is particle size. Furthermore, the washout ratio, which is the metric used to interpolate scavenging efficiencies, was computed for BC mass and not number. Therefore, direct comparisons of their work and the work presented here are difficult to make. Some field studies (Hallberg et al., 1992, 1994) have shown that 10-20% of atmospheric BC can activate at supersaturations of between $\approx$ 0.2-0.5%. Several of the studies mentioned in the preceding discussion used different measurement techniques than the one presented in this chapter.

Slowik et al. (2007) presents a detailed inter-comparison of different methods for measuring BC and possible corrections needed for making direct comparisons between differing techniques. None of the data reported here have been corrected for sampling technique.

Although the activated fraction of BC in cloud droplets has been measured at some locations, the true contribution of BC to CCN in the atmosphere is unknown, yet potentially significant (Chen et al., 2010). Measurements of the activated fraction of BC as a function of size are important to test our current understanding of the incorporation of BC particles into cloud droplets. In this study we measured rBC as a function of size in cloud residuals at a marine boundary layer site (251 m amsl) in La Jolla, CA during 2012 and compared the results with rBC as a function of size measured from a total inlet that sampled both cloud residuals and interstitial particles. Coating thicknesses on rBC cores in the cloud residuals were also determined. The measurements of rBC as a function of size in cloud residuals were further compared to predictions with kappa-Köhler theory (see Chapter 2).

4.2 Sampling Site

4.2.1 Site description

The sampling site was located below the peak of Mt. Soledad (251 m above mean sea level (a.m.s.l.)), which is 3 km from the coast of the Pacific Ocean in La Jolla, CA (32.8400°N, 117.2769°W). The city of La Jolla is predominately residential with a population of approximately 43,000 people and situated 24 km north of

San Diego (population 1.3 million), the closest urban center.

Data were collected from 27 May to 18 June, 2012 using instruments housed in a modified shipping container. A total of three stratocumulus clouds were sampled during this time frame. The first cloud event was rejected from analysis due to an instrumental error. The second cloud event occurred from 12 June 2012 20:43 to 13 June 2012 11:35 PDT, and hereinafter called Cloud 2. The third cloud event took place from 17 June 2012 20:36 to 18 June 2012 07:52 PDT, and called Cloud 3 for the remainder of the document.

4.2.2 Inlets

Two inlets, referred to as the total inlet and residual inlet, were used during this study (Figure 4.1). The total inlet measured both interstitial and cloud residual particles during cloud events. This heated inlet was designed and built following the specifications reported by Bates et al. (2002) and therefore assumed to have the same transmission efficiency, namely $> 95\%$ for particles $<$6.5 μm.

The intake of the residual inlet was a CVI (see Section 4.3.1) that enabled the sampling of cloud droplets without interstitial particles, thus only the residual particles of the cloud droplets were sampled. This inlet was used only during cloudy periods and was connected to a branch of the total inlet by a 3-way valve (Figure 4.1). During a cloud event, the valve was manually switched so that cloud droplets were sampled through the CVI and cloud residuals were measured by instrumentation connected downstream of the valve. At times when no clouds were present the valve was switched such that all instruments sampled ambient

particles.

Since much of the analysis performed in this study is based on a measured ratio of particle number concentration it was necessary to ensure that there were no significant losses of particles due to the inlet configuration. Therefore, particle losses from diffusion, sedimentation, turbulent inertial deposition and inertial deposition from both bends and contractions for the total and residual inlets (assuming cloud free sampling) were calculated using the Particle Loss Calculator (Von der Weiden et al., 2009) and found to be $< 2\%$ for particles with diameters between 0.07 and 1 μm, covering the size range used for this analysis.

4.3 Experimental

4.3.1 Counterflow virtual impactor

4.3.1.1 Theory of operation

In order to separate cloud droplets from interstitial particles a counterflow virtual impactor (CVI) was used. A CVI separates droplets from interstitial particles by using inertial separation. A schematic of the CVI probe is shown in Figure 4.2. During operation, the CVI probe is placed inside a wind tunnel, which is connected to a vacuum pump that accelerates droplet laden air (shown as green lines in Figure 4.2) to high velocities ($\approx$100 m s^{-1}). Since the air contains different sizes of droplets and particles, the process of accelerating this air mass to a constant velocity imparts different inertial forces on the droplets and particles. The vacuum intake draws the accelerated air towards the CVI probe, which is made up

of two concentric cylindrical tubes (see Figure 4.2). The tip of the outer cylinder provides the inlet where cloudy air is sampled through an orifice with an outer radius of r_o. The inner concentric cylinder has a porous frit at its tip; which allows a supply gas (shown as red lines in Figure 4.2) to permeate through. The inner cylinder is also connected to a vacuum pump downstream, which creates the sample flow (shown as a purple line in Figure 4.2), the counterflow (shown as yellow lines in Figure 4.2), and the stagnation plane, which is a theoretical plane within the porous frit that droplets must cross in order to be sampled (shown as a black dashed line in Figure 4.2). Based on a CVI's specific geometry and the flow rates used a minimum droplet diameter exists that will be sampled by the CVI. Once a droplet enters the CVI probe tip the water component of the droplet, as well as any dissolved volatile gasses, begin to evaporate upon impacting with the warm dry counterflow of gas (often purified air or N_2). Droplets that are sampled by the CVI are further evaporated by heated sections of the sample tubing, which are typically held at a constant temperature of 40°C. Therefore, the instrumentation downstream of the CVI samples only the residuals of the cloud droplets that remain after evaporation.

4.3.1.2 Calculating a CVI cut-size

The minimum droplet diameter sampled by a CVI is considered to be the CVI cut-size ($CVI - D_{50}$) and is the diameter for which a droplet's stopping distance (D_{stop}) is greater than the length to the stagnation plane (L_{stag}) (Anderson et al.,

1993; Noone et al., 1988), or:

$$CVI - D_{50} = D_{stop} > L_{stag}, \tag{4.1}$$

where L_{stag} is comprised of three components, and is equal to:

$$L_{stag} = L_{min} + L_{por} + L_{cur}, \tag{4.2}$$

where L_{min} (see #2 labeled in Figure 4.2) is the amount of dead-space that exists between the CVI orifice and the top of the porous frit, L_{por} (see #3 labeled in Figure 4.2) is the length from the top of the porous frit to the stagnation plane, which is related to the counterflow ($F1$), sample flow ($F2$), and the length of the entire porous frit (X, see #4 labeled in Figure 4.2) by Equation 4.3:

$$L_{por} = \left[\frac{F1 - F2}{F1}\right] X, \tag{4.3}$$

L_{cur} is a parameterization (Anderson et al., 1993) that estimates the length a particle must traverse to deviate from the high velocity streamlines curving around the CVI probe tip in order to enter the CVI orifice, and is considered a linear function of the outer radius (r_o) of the tip:

$$L_{cur} = Cr_o, \tag{4.4}$$

where C can range from 0 to 1 (Anderson et al., 1993; Noone et al., 1988) and

represents the uncertainty of the estimate. In this document, $CVI - D_{50}$ is always reported at C=0.5 and the uncertainty of the cut-size is calculated by averaging the differences calculated when using the lower and upper bounds of C=0 and C=1, respectively.

D_{Stop} can be calculated as follows (Serafini, 1954):

$$D_{Stop} = \frac{r_d \rho_d}{3\varepsilon^{\frac{3}{2}} \rho_{air}} \left[Re_d^{1/3} \varepsilon^{1/2} - \frac{\pi}{2} + tan^{-1} \left(Re_d^{-1/3} \varepsilon^{-1/2} \right) \right], \tag{4.5}$$

where r_d is the droplet radius, ρ_d is the droplet density, ε is a constant (0.158), ρ_{air} is the density of air, and Re_d is the droplet Reynolds number, which is represented by:

$$Re_d = \frac{2\rho_d r_d V_\infty}{\eta_{air}}, \tag{4.6}$$

where V_∞ is the CVI air intake velocity, and η_{air} is the viscosity of air.

4.3.1.3 Calculating a CVI enhancement factor

Sampling through a CVI will also enhance the particle concentrations relative to the initial ambient concentrations (Noone et al., 1988; Serafini, 1954). Therefore, measurements made downstream of a CVI need to be corrected by what's referred to as the enhancement factor (EF), which can be calculated using the following equation:

$$EF = \frac{V_\infty \pi r_i^2}{F2}, \tag{4.7}$$

where r_i is the inner radius of the CVI probe tip.

The CVI used during this study, as well as the study discussed in Chapter 5

was based on the design by (Noone et al., 1988) with the following geometry: an outer radius (r_o) of 0.9 cm; an inner radius (r_i) of 0.3 cm; and a 9.5 cm long porous frit (X).

4.3.1.4 CVI cut-size and enhancement factor measured at La Jolla, CA

Based on Equation 4.5 above, a $CVI - D_{50}$ of 11.5±0.7 μm and 11.6±0.7 μm for Cloud 2 and Cloud 3, respectively, were calculated for the two clouds sampled in this study. In addition, using Equation 4.7, calculated EF values were 7.1 and 7.4 for Cloud 2 and Cloud 3, respectively.

4.3.2 Refractory black carbon measurements

4.3.2.1 Refractory black carbon mass measurements

Refractory black carbon (rBC) mass was measured from the total inlet and the residual inlet using two separate SP2s (Droplet Measurement Technologies, Boulder, CO). These instruments are referred to as the total SP2 ($SP2_{Tot}$) and the residual SP2 ($SP2_{Res}$). The location of these instruments is shown in Figure 4.1. The SP2 has been described in detail in Chapter 3 and elsewhere (Moteki and Kondo, 2008; Schwarz et al., 2006; Stephens et al., 2003). The two SP2s used in this study were calibrated pre and post-campaign following the procedure discussed in Section 3.3. The calibration parameters used to determine mass were taken from a second order polynomial fit of the combined pre and post-campaign data. A VED was also determined from the measured mass assuming a BC density of σ_{bc}=1.8 g cm^{-3} (Bond and Bergstrom, 2006). The $SP2_{Res}$ was a 4 channel instrument with

a detection range of 70-220 nm, whereas the $SP2_{Tot}$ was an 8 channel instrument with a detection range of 70-558 nm.

4.3.2.2 Refractory black carbon coating thickness measurements

The information from the two scattering APDs (see Figure 1.1) was used to determine the coating thicknesses on rBC cores as described in Section 3.5 and by Gao et al. (2007). Due to a failure of the split detector on the SP2 connected to the total inlet, coating thicknesses on rBC cores were only determined from the data collected with the SP2 connected to the residual inlet. To determine coating thicknesses the scattering amplitudes for rBC containing particles were determined using the LEO fitting method (see Section 3.5 and Gao et al. (2007)). In short, the early part of the elastic scattering signal (up to 5% of the maximum laser intensity (Gao et al., 2007)) was fit to a Gaussian function and the maximum scattering amplitude was retrieved from the fit.

As mentioned above, only data collected with the SP2 connected to the residual inlet were analyzed for coating thickness. Approximately 99% of the rBC containing particles detected with the $SP2_{Res}$ had elastic scattering signals above the background signals on the APDs. Nevertheless, only 50% of the rBC containing particles detected with the $SP2_{Res}$ were successfully fit with the LEO fitting procedure. Hence, coating information reported here is only from a subset of the rBC particles measured with the $SP2_{Res}$. Failure to fit the elastic scattering signals with the LEO procedure was mainly due to either; a) large scattering signals that saturated the APD detector, or b) time dependent scattering signals were above 5%

of the maximum laser intensity at time zero. 11% and 27% of all rBC containing particles detected with the $SP2_{Res}$ had a failure due to a) and b), respectively.

4.3.3 Size distribution measurements of the bulk aerosol

Two instruments were used to measure particle size distributions (Figure 4.1). Size distributions of particles sampled from the total inlet were determined with a scanning electrical mobility spectrometer (SEMS, model 2002, BMI, Hayward, CA), which counted particles into 61 discrete size bins from 0.01-1 μm with a 5-minute scan time interval. Size distributions of particles sampled from the residual inlet were determined with a scanning mobility particle sizer (SMPS, model 3034, TSI, St. Paul, MN), which recorded particle counts into 55 size bins from 10-487 nm with a 3-minute scan time interval. Both the SEMS and SMPS operate based on the coupling of a size selecting DMA and a condensational growth particle counter (CPC). During cloud free sampling the SMPS and SEMS agreed to within 4% for particles between 70 and 400 nm.

4.3.4 Aerosol mass spectrometry

An online high-resolution time-of-flight aerosol mass spectrometer (HR-ToF-AMS, Aerodyne Reserch Inc., Billerica, MA) was operated downstream of the CVI on the residual inlet to characterize the chemical composition of the cloud droplet residuals. The HR-Tof-AMS measured non-refractory, sub-micrometer aerosol chemical composition at high time resolution (DeCarlo et al., 2006). Here we only consider data measured by the HR-ToF-AMS in its mass-spectrum and V-

modes of operation. These data were recorded as 2 minute averages every 4-6 minutes, depending on how many other modes of operation (W-mode, light scattering) the instrument was alternating between. Size-resolved composition data for the residual particles measured by the HR-ToF-AMS in time-of-flight mode are not considered here since the signal was generally at or below the detection limit. Standard quantification procedures (Allan et al., 2004) were applied to the mass spectra measured by the HR-ToF-AMS to determine the relative concentrations of the non-refractory species (organic, nitrate, sulfate, ammonium and chloride) typically reported by aerosol mass spectrometry.

4.3.5 Back trajectories

Air mass back trajectories were calculated using the National Oceanic and Atmospheric Administration (NOAA) Hybrid Single Particle Lagrangian Integrated Trajectory Model (HYSPLIT) (Draxler and Rolph, 2013; Rolph, 2013). All trajectory calculations used the National Centers for Environmental Predictions EDAS meteorological dataset. Trajectories were calculated starting at 10 m above ground level (a.g.l.), 96 hours backwards in time, and at hourly intervals throughout the entire period of cloud sampling.

4.3.6 Cloud properties

A fog monitor (FM-100, model 100, Droplet Measurement Technologies, Boulder, CO), which is a forward scattering optical spectrometer, was stationed on top of the shipping container providing an in-situ measurement of CDNC in 20 dis-

crete size bins ranging from 2-50 μm, whilst simultaneously monitoring the liquid water content (LWC) present with a 1 second time resolution (Eugster et al., 2006).

4.4 Results and Discussion

4.4.1 Back trajectories

The back trajectories for Cloud 2 (Figure 4.3 panels A and C) show that the air mass spent most of the previous 96 hours over the Pacific Ocean and arrived at the sampling site from a northwesterly direction. During the first part of Cloud 2 (12 June 21:00 to 13 June 08:00 PDT) the back trajectories became progressively more northerly and the air mass began traveling near large populated urban regions. Towards the end of the cloud event (at $\approx$ 09:00 PDT on 13 June) the winds shifted to southwesterly. Based on the back trajectories the air mass for Cloud 2 traveled $\approx$ 40-50 km over land before reaching the sampling site. In addition, the air mass spent a significant amount of time close to the ocean surface prior to being lifted up to the sampling site (Figure 4.3 panel C).

The back trajectories for Cloud 3 (Figure 4.3 panels B and D) also show that the air mass spent the majority of the previous 96 hours over the Pacific Ocean before arriving at the site. At the start of Cloud 3 (17 June 21:00 to 22:00 PDT) the air mass arrived from the northwest. Throughout the remainder of the cloud event (17 June 23:00 to 18 June 08:00 PDT) the air mass continued to shift farther north and by the end of the cloud event (18 June 08:00 PDT) the air mass was traveling south along the coastline before arriving at the sampling site. The back trajectories

indicate that the air mass traveled ≈10-20 km over land prior to arriving at the sampling site. Similar to Cloud 2, the air spent a significant amount of time close to the ocean surface prior to being lifted up to the sampling location (Figure 4.3 panel D). Since the trajectories during both clouds are close to the coastline for a period of time, it is likely these air masses contained both marine particles and anthropogenic emissions.

4.4.2 Meteorological conditions and cloud properties

For the purposes of this study, the data were classified as in-cloud and included for analysis if they met the following criteria: 1) the five-minute-averaged CVI counterflow was within $\pm 5\sigma_{std}$ of the mean counterflow to ensure only periods of stable CVI flows were included; and 2) the five-minute-averaged *LWC* was greater than 0.05 g m^{-3} to remove periods of entrainment, or "patchy"regions of the cloud as much as possible (Cozic et al., 2007).

The measured cloud properties as a function of time are shown in Figure 4.4 (panels A to C), where Cloud 2 is shown on the left side and Cloud 3 is shown on the right side of the plot. Cloud 2 was characterized by an average temperature of 13.4±0.2 °C with light and variable winds (0.5±0.2 m s^{-1} and 190±90°respectively), and an average *LWC* of 0.13±0.07 g m^{-3}. During the middle portion of Cloud 2 (13 June 01:00 to 02:00 PDT) the droplet distributions clearly show an interval where the number of droplets above the $CVI - D_{50}$ (black trace overlaid on panel C) increases significantly, which coincides, in time, with a sharp increase in *LWC*. Cloud 3 was characterized by an average temperature of 15.2±0.1 $°C$, northerly

(330±10°) winds with an average speed of 1.5±0.4 m s^{-1}, and an average *LWC* of 0.09±0.02 g m^{-3}.

The cloud droplet number and volume size distributions, averaged over the entire event, are shown in Figure 4.5, and further summarized in Table 4.1. Cloud 3 had a CDNC of 146 cm^{-3}, a factor of two higher than during Cloud 2 (68 cm^{-3}).

From the calculated $CVI - D_{50}$ and the fits to the droplet size distribution (Figure 4.5) the number and volume fraction of droplets sampled by the CVI were determined. The results are summarized in Table 4.1. During Cloud 2 the number fraction of droplets larger than the $CVI - D_{50}$ was about 38% and for Cloud 3 the fraction sampled was about 24%. Since only the larger droplets were sampled by the CVI during these two cloud events, the results presented herein are only representative of the larger droplet population.

4.4.3 Size distributions

Average size distributions of the bulk aerosol particles and rBC particles measured from the total and residual inlets for both Cloud 2 and Cloud 3 are shown in Figure 4.6. Data are plotted in two ways: on a log scale, in panels A and B, and normalized to the respective maximum, in panels C and D. Table 4.2 summarizes the results obtained from the size distribution analysis.

4.4.3.1 Size distributions measured from the total inlet ($\mathbf{BulkAero_{Tot}}$ and $\mathbf{rBC_{Tot}}$)

The average size distributions of the bulk aerosol measured from the total inlet (referred to as $BulkAero_{Tot}$ for the remainder of the document) and the average size

distributions of rBC measured from the total inlet (referred to as rBC_{Tot} for the remainder of the document) are shown in Figure 4.6. The $BulkAero_{Tot}$ distributions for both clouds show evidence of at least two overlapping modes. A single mode lognormal distribution function was fit to the data yielding mean geometric diameters (D_g) of 108 and 81 nm with geometric standard deviations (σ_g) of 1.58 and 1.70 for Cloud 2 and Cloud 3 respectively. Integration of the number distribution during Cloud 2 results in a total number concentration (N_{Tot}) for the bulk aerosol of 981 cm^{-3}. Likewise, N_{Tot} during Cloud 3 was measured to be 994 cm^{-3}. Previous measurements in the marine boundary layer have classified the environment as "clean" marine if the number of particles is $\leq$ 300-500 cm^{-3} and "polluted" marine if the number concentrations are $\geq$ 400-1500 cm^{-3} (Andreae, 2009; Bates et al., 2000; Glantz and Noone, 2000; Hawkins et al., 2010; O'Dowd et al., 2001; Pirjola and O'Dowd, 2000; Twohy et al., 2005). Thus, the particle concentrations measured at Mt. Soledad, in addition to the back trajectories, suggest that for both clouds the air masses can be classified as polluted marine aerosols. The size distributions of the $BulkAero_{Tot}$ as a function of time are also included in Figure 4.4 panel D for comparison.

The rBC_{Tot} size distributions for each cloud are shown in Figure 4.6. The D_g for rBC_{Tot} (assuming the number distributions are lognormal) during both events lies somewhere in the nucleation mode at $<$70 nm, which is outside the detection range of the SP2. Integration of the rBC_{Tot} distributions, from 70-220 nm, yields an N_{Tot} of 75 cm^{-3} during Cloud 2 and 62 cm^{-3} in Cloud 3. Assuming a rBC density of σ_{bc}=1.8 g cm^{-3} the total mass concentrations (M_{Tot}) are 73 and 62 ng

m^{-3} for Cloud 2 and Cloud 3 respectively (Table 4.2). The rBC_{Tot} mass concentrations observed at Mt. Soledad were higher than concentrations measured in clean marine air (Cooke et al., 1997; Shank et al., 2012), but considerably lower than concentrations measured in most urban environments (see Table 1 in Metcalf et al. (2012)).

4.4.3.2 Size distributions measured from the residual inlet ($BulkAero_{Res}$ and rBC_{Res})

Average size distributions of the bulk aerosol measured from the residual inlet (referred to as $BulkAero_{Res}$ for the remainder of the document) are also shown in Figure 4.6. The size distributions of the $BulkAero_{Res}$ indicate that it was mostly the larger particles of the $BulkAero_{Tot}$ distributions that were incorporated into the sampled cloud droplets. The size distributions of $BulkAero_{Res}$ as a function of time for both cloud events are included in Figure 4.4 panel E for comparison.

The size distributions for $BulkAero_{Res}$ shown in Figure 4.6 have a local minimum at 110 nm for Cloud 2 and 90 nm for Cloud 3. The particles observed at sizes less than the local minima may be due to droplet "splash", or due to a leak in the CVI. (Pekour and Cziczo, 2011; Schwarzenboeck et al., 2000; Vidaurre et al., 2011).

Figure 4.6 also shows the size distributions of the rBC residuals (rBC_{Res}) measured with the CVI. Figure 4.6 shows that rBC cores smaller than 100 nm are incorporated into cloud droplets. In addition, Figure 4.6 shows that most of the rBC_{Res} have effective sizes of less than 100 nm and that the rBC_{Res} are overall larger than the rBC_{Tot}. Fitting the rBC_{Res} size distributions (assuming these dis-

tributions are lognormal) results in mean geometric diameters of 87 and 81 nm for Clouds 2 and 3 respectively.

4.4.4 Size-resolved activated fractions

The size-resolved activated fraction [$AF(D_p)$] for rBC and the bulk aerosol were calculated by taking the ratio of the number size distributions measured from the residual inlet and the number size distributions measured from the total inlet. Prior to calculating $AF(D_p)$, a spline interpolation algorithm was applied to the rBC and bulk aerosol number size distributions. After a spline interpolation was applied to the data, the following equation was used to calculate the size-resolved activated fraction:

$$AF(D_p) = \frac{N_{Res}(D_p) * CF(D_p)}{N_{Tot}(D_p) * EF * DT}, \tag{4.8}$$

where $N_{Res}(D_p)$ is the number of residual particles as a function of size, $CF(D_p)$ is the size-resolved instrument sensitivity correction factor, $N_{Tot}(D_p)$ is the number of particles measured from the total inlet as a function of size, EF is the CVI enhancement factor (see Section 4.3.1.3) and DT is the droplet transmission factor through the CVI. Calculations of the droplet transmission factor are given in Appendix B and plotted in Figure B.1. $CF(D_p)$, which corrects for variances in instrument detection efficiencies, were determined from a 12hr period of cloud free air on 5 June 2012 for the bulk aerosol and from side by side ambient sampling of room air during the post-campaign calibration for rBC.

The $AF(D_p)$ for the bulk aerosol and rBC are presented in Figure 4.7, where the error bars represent one standard deviation ($1\sigma_{std}$) of the AF for each 10 nm

size bin. The AF as a function of size for the bulk aerosol is similar to previous measurements in similar clouds (Hallberg et al., 1994). Figure 4.7 panels A and B show that the AF of rBC cores is significant, even for core diameters of $\leq$ 100 nm. Figure 4.7 panels A and B also show that during both clouds the AF for rBC cores is larger than the AF for the bulk aerosol at diameters $<\approx$150 nm. These results can be explained by the presence of large coatings surrounding the core (see Section 4.4.5). Since the fraction of droplets sampled by the CVI was $<$100%, the calculated AF should be considered as a lower limit to the total fraction activated during these two cloud events.

4.4.5 Coating thickness of refractory black carbon residuals

Coating thicknesses were determined using a core and shell Mie model (see Section 3.5) and are shown in Figure 4.7 panels C and D, where the error bars represent $1\sigma_{std}$ and the symbols represent the averages. When calculating coating thicknesses, the particles were idealized as a pure BC core uniformly coated with a non-absorbing material, although the actual particle morphology may be more complicated (Sedlacek et al., 2012). As mentioned in Section 4.3.2.2, only 50% of the rBC containing particles detected with the $SP2_{Res}$ were successfully fit with the LEO fitting procedure. Hence, coating information reported below is only from a subset of the rBC residual particles measured.

Both cloud events show a similar trend, namely that the coating thicknesses are larger at smaller rBC core diameters than larger rBC core diameters, which has also been observed elsewhere (Metcalf et al., 2012). At small core diameters (70-

100 nm) the coating thicknesses range from roughly 45-115 nm, while at larger core diameters (200-215 nm) the coatings range from roughly 0-60 nm. Coating thicknesses measured in this study fall between values measured in previous studies. For example, coating thicknesses ranging from 20 ± 10 nm, in fresh urban plumes (Schwarz et al., 2008a), up to 188 ± 31 nm on more aged rBC particles (Metcalf et al., 2012) have been reported.

4.4.6 In-cloud aqueous phase chemistry

In the discussion above, we assume the coatings on the rBC cores were present before incorporation into the cloud droplets. However, some of the coating material may have formed after the rBC cores were incorporated into the cloud by aqueous phase chemistry. Although stratus cumulus decks can persists for hours, large eddy simulations of non-precipitating stratocumulus suggest that in-cloud residence times of air parcels can be on the order of 12 minutes (Stevens et al., 1995). Based on this work, we assume that an upper limit of 1 hour for the clouds measured in this study is reasonable. Whether significant aqueous phase chemistry can occur on this time scale depends on the level of SO_2 and oxidants. When SO_2 is absorbed by a cloud droplet, it partitions in different forms as a function of pH: at lower pH values, the primary aqueous phase oxidant of dissolved SO_2, or S(IV) is H_2O_2; for higher pH values, ozone and catalyzed aerobic oxidation are important oxidation pathways. Depending on the pH and available oxidants, conversion of the dissolved S(IV) to S(VI) can be fast or slow. The absorption of large amounts of HNO_3 or N_2O_5 can reduce the pH significantly, which will require the

presence of H_2O_2 in order to significantly convert S(IV) to S(VI). Since the clouds at Soledad were mostly overnight, the primary oxidant (H_2O_2) was likely lower (and probably near zero). Also, analysis of the cloud water indicated that nitrate was high, and thus the pH was probably low. Based on these factors, we suspect that aqueous phase production of sulfate was not large. However, a quantitative estimate of the sulfate produced is not possible since the measurements of SO_2 and H_2O_2 were not performed at this site. Based on the discussion above, we assumed that a large fraction of the coatings were present before rBC particles were incorporated into the cloud droplets. However, the production of coating material from in-cloud aqueous phase chemistry cannot be ruled out.

4.4.7 Size distributions of rBC_{Res}(Core+Coating)

For rBC particles measured from the residual inlet, a core diameter (determined from the incandescence signal) and a coating thickness (determined from the Mie scattering calculations discussed in Section 3.5) were combined to calculate the overall rBC particle diameter (Core + Coating). These data are plotted in Figure 4.8, where the distributions are shown to be shifted to larger sizes when compared with the distributions plotted as a function of core diameter [rBC_{Res}(Core)] alone. These results suggest that the coated rBC particle diameters were likely the dominant factor in activation ability over composition. This is a result that has also been seen elsewhere (Fierce et al., 2013). For example, Fierce et al. (2013) investigated how different particle characteristics (e.g. size, supersaturation, and 24 hour aging) at emission influence CCN activity and found that for S_C ¿ 0.2%

CCN activity had a greater sensitivity to emission size than composition.

4.4.8 Comparison of rBC_{Res} as a function of size with predictions based on kappa-Köhler theory

Sections 4.4.5 and 4.4.7 provide a qualitative explanation for why rBC cores smaller than 100 nm are incorporated into cloud droplets, namely that rBC cores have thick coatings which lead to overall particle diameters >100 nm. In the following, we expand on this qualitative explanation by carrying out a quantitative analysis showing that the presence of rBC cores smaller than 100 nm in the cloud residuals is consistent with kappa-Köhler theory. This quatitative analysis consists of the following steps: 1) an estimation of the bulk aerosol composition; 2) an estimation of the critical diameter for activation of the cloud droplets sampled; 3) an estimation of the critical supersaturation required to form the droplets sampled; and 4) a prediction of the critical diameter for activation of rBC cores. Steps 1-3 are required to carry out the predictions in step 4.

4.4.8.1 Bulk aerosol composition

An HR-Tof-AMS was used to measure the bulk aerosol composition downstream of the CVI. Five species (organic, nitrate, sulfate, ammonium and chloride) were quantitatively differentiated. Then, based on a simplified ion-pairing scheme similar to Gysel and Crosier (2007) (see Appendix A), the mass fractions of ammonium nitrate, ammonium sulfate, ammonium bisulfate, sulfuric acid, and ammonium chloride were calculated. The results of these calculations are shown in Figure 4.9. In order to determine the bulk aerosol hygroscopicity (see Equa-

tion 2.3), mass fractions, of these individual components, were first converted to volume fractions using an organic density of 1.4 g cm^{-3} (Moore et al., 2012) and densities reported in Lide (2001) for the inorganic salts.

4.4.8.2 The critical diameter for activation of the bulk aerosol in the cloud droplets sampled

The critical diameter for activation (D_{pc}) of the bulk aerosol is often calculated by integrating the residual number distribution from the largest to the smallest diameters until the number concentration equals the CDNC sampled (see for example Hersey et al. (2013)). Using this method, D_{pc} was found to be 241 nm and 239 nm for Cloud 2 and Cloud 3 respectively. Note these D_{pc} apply only to the cloud droplets sampled (i.e. cloud droplets $>\approx$11 μm). Different D_{pc} values would be expected if the entire droplet population were sampled.

4.4.8.3 Critical supersaturation for the cloud droplets sampled

To estimate the critical supersaturation (S_C) for the formation of cloud droplets sampled during the two cloud events (i.e. cloud droplets $>\approx$11 μm) the single parameter kappa-Köhler model was used (see Chapter 2). The individual κ values used in Equation 2.3 for the species discussed in Section 4.4.8.1 were; 0.1 for organic (Lance et al., 2013; Moore et al., 2012; Rose et al., 2010); 0.67 for ammonium nitrate (Petters and Kreidenweis, 2007); 0.61 for ammonium sulfate and ammonium bisulfate (Petters and Kreidenweis, 2007; Wu et al., 2013); and 0.71 for sulfuric acid, which is the average of the range reported in Shantz et al. (2008). The value for ammonium chloride κ was calculated according to Equation A28 in

Rose et al. (2008) using a Van't Hoff factor of 2.

Using the above κ_i values and the values for υ_i, discussed in Section 4.4.8.1, in Equation 2.3, κ_{Bulk} values of 0.50 and 0.41 were calculated for Cloud 2 and Cloud 3 respectively. The values determined during this study are consistent with the values suggested by Andreae and Rosenfeld (2008) for Cloud 2 and lower than the values suggested for Cloud 3, for marine aerosols.

Shown in Figure 4.10 panel A are plots of S_C as a function of dry diameter for Cloud 2 (solid line) and Cloud 3 (dashed line) calculated using Equation 2.2 and Equation 2.3. Combining D_{pc} (see Section 4.4.8.2) with the results plotted in Figure 4.10, S_C for the cloud droplets sampled can be determined. The points at which D_{pc} intersects with the calculated S_C traces shown in Figure 4.10, result in estimations of S_C values of approximately 0.05% for both clouds. Note, these S_C apply only to the droplets sampled by the CVI. Different S_C values would be expected if the entire droplet population had been sampled. However, it also should be noted that theory predicts that the largest droplets in the distribution should have been the first to form, thus formed on particles activated at the lowest supersaturations. The SC calculated for the coated rBC particles shown in Figure 4.10 are consistent with this theory.

In this determination of S_C several assumptions were made, which are addressed separately below: 1) the predominant mechanism for incorporation of particles into droplets was nucleation scavenging, and influences by impaction were negligible (Noone et al., 1992); 2) the contribution from sea salt aerosols could be neglected. Based on sea salt mass concentrations measured by the HR-

Tof-AMS behind the CVI and calibrated against collocated ion chromatography measurements following a procedure similar to that introduced by Ovadnevaite et al. (2012), we estimated an upper limit of approximately 15% for the sea salt mass fraction of cloud residuals. By including an estimated sea salt mass fraction of 15% into the bulk aerosol composition, bulk kappa values of 0.57 and 0.49 were calculated and used to estimate S_C. Using these kappa values reduced the reported estimated S_C of 0.05% by <8%; 3) we assumed that the particles were internally mixed and the composition did not depend on size. Since, during this study, the size dependent HR-ToF-AMS data were at or below the detection limit we could not determine if the composition was dependent on size. Additionally, no measurements of the bulk aerosol mixing state were carried out; and 4) we assumed that the entire fraction of organics was water soluble and represented by a κ of 0.1. To determine if S_C was sensitive to this value, κ for organics was varied from 0-0.2, which is roughly consistent with the range of κ values reported in the literature for organics (Chang et al., 2010; Lathem et al., 2013; Mei et al., 2013). Over this range of κ values, S_C varied by <4%.

4.4.8.4 Predictions of the critical diameter for activation of refractory black carbon cores

In Figure 4.10 panel B the critical diameter for activation of rBC cores, for cloud droplets sampled, is calculated using kappa-Köhler theory (see Chapter 2) and assuming coating thicknesses ranging from 0-200 nm, which covers the range of coating thicknesses measured. In these calculations the composition of the coating was assumed to be the same as determined by the HR-ToF-AMS (see

Section 4.4.8.1), and the rBC cores were assumed to be insoluble with a $\kappa = 0$ (Rose et al., 2010). As expected, in Figure 4.10 panel B, S_C decreases as the coating thickness increases at a constant rBC core diameter. Figure 4.10 panel B also shows that if the S_C is $>\approx 0.05\%$, for both clouds, the critical diameter for activation of the rBC cores is $<$50 nm for all cores with coating $\geq$100 nm. The combinations of core + thicknesses shown in Figure 4.10 can be translated into the equivalent volume fractions and kappa values, assuming the coating has a kappa of 0.5 and the core has a kappa=0. The smallest kappa in this figure is for a 1 μm core with a 25 nm coating, κ=0.07; however the size is so large the critical supersaturation is very low anyways despite the low kappa. The smallest total particle size (and highest critical supersaturation) represented in Figure 4.10 is a particle with a 50 nm core and 25 nm coating, total 100 nm diameter; the corresponding kappa is 0.44. For cores between 50 and 200 nm and thicknesses between $\approx$ 25 to 200 nm, kappas range from $\approx$ 0.35 to 0.5. As can be seen for the two lines in Panel A this much variability in overall kappa does not create a large change in critical supersaturation. This suggests that the uncertainties of the estimated S_C should have minimal influence on the predicted critical activation diameter of rBC using kappa-Köhler theory. Furthermore, the results from kappa-Köhler theory are consistent with the observations of rBC cores of 100 nm and less being activated into the sampled cloud droplets.

4.5 Summary and Conclusions

Cloud residuals were measured during two cloud events at the top of Mt. Soledad in La Jolla, CA. Back trajectories showed that air masses for both cloud events spent at least 96 hours over the Pacific Ocean and traveled near, or over populated regions before arriving on site. Based on measured bulk aerosol number concentrations the two air masses sampled were classified as polluted marine air, a classification consistent with the back trajectories and measured concentrations of black carbon mass.

The size distributions of the bulk aerosol residuals were shifted to larger sizes for both cloud events compared to the size distributions measured from the total inlet. The size distributions of rBC cloud residuals were also shifted towards larger diameters when compared to the size distributions of rBC measured from the total inlet. The measurements of cloud residuals clearly show that rBC cores less than 100 nm can be incorporated into cloud droplets, assuming that the coatings surrounding these cores are at least moderately hygroscopic and sufficiently large enough to increase the overall particle diameter so that they can contribute to the CCN at low supersaturations. The activated fraction of 70-80 nm rBC cores was 0.01 and 0.045 for Cloud 2 and Cloud 3 respectively. Since the fraction of cloud droplets sampled by the CVI was less than 100%, the measured activated fractions of rBC are lower limits to the total fraction of rBC activated during these two cloud events. The coating analysis of the SP2 data shows that the rBC cores that were activated into cloud droplets had thick coatings, with average coating

thicknesses of ≈75 nm at core diameters between 70-80 nm and ≈29 nm coatings for core diameters between 200-210 nm. Furthermore, the presence of rBC cores less than 100 nm in cloud residuals is consistent with kappa-Köhler theory and the measured rBC coating thicknesses.

4.6 Chapter 4 Figures and Tables

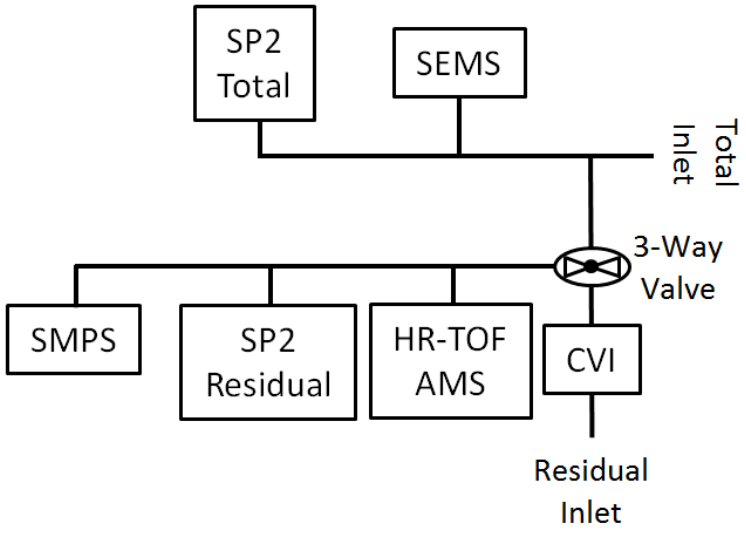

Figure 4.1: Schematic showing the configuration of the inlets and instrumentation housed in the shipping container.

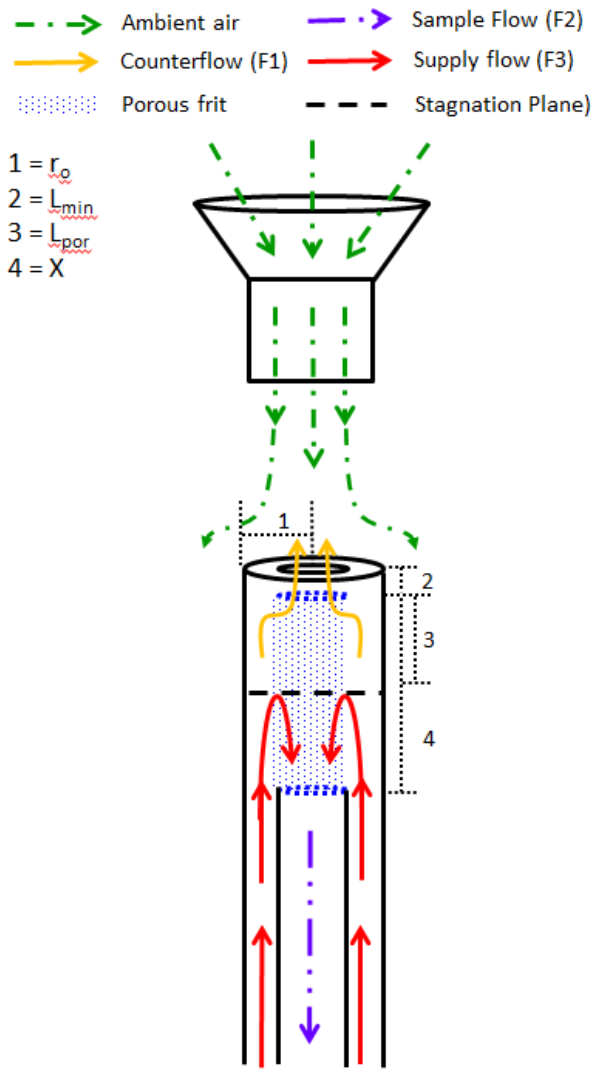

Figure 4.2: Schematic of the CVI showing ambient air (green dashed lines) being drawn towards the CVI probe. The supply flow (red lines) are shown to permeate the porous frit (blue dotted region) creating the counterflow (orange lines) and sample flow (purple dash-dot line). The theoretical stagnation plane (black dashed line) and CVI geometry parameters needed to calculate the stopping distance of a droplet entering the CVI probe (see Section 4.3.1 for further details) are also shown and labeled 1 to 4.

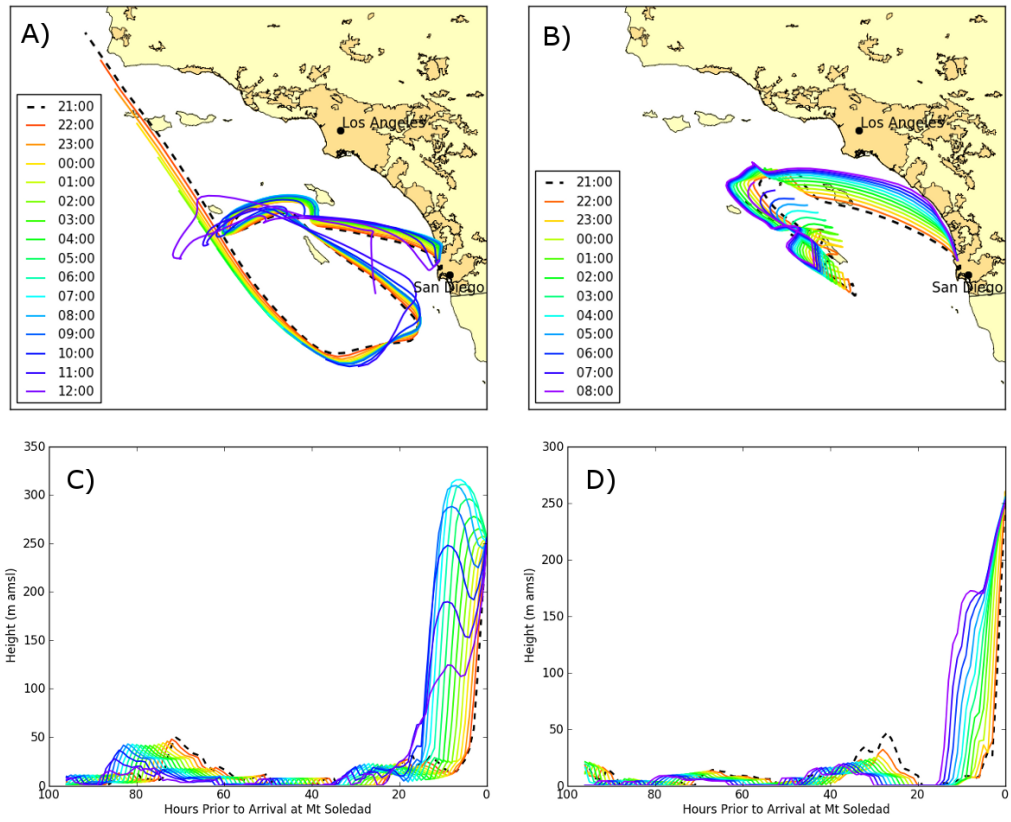

Figure 4.3: In-cloud HYSPLIT 96hr back trajectories ending at hourly intervals for Cloud 2 (12 June 21:00 to 13 June 12:00 PDT) in panels A and C, and Cloud 3 (17 June 21:00 to 18 June 08:00 PDT) in panels B and D. All back trajectories started at 10 m a.g.l.. Darker yellow regions on land in panels A and B indicate densely developed urban areas containing 50,000 or more people (United States Census Bureau). Panels C and D show the vertical profiles over the same hourly intervals shown in panels A and B.

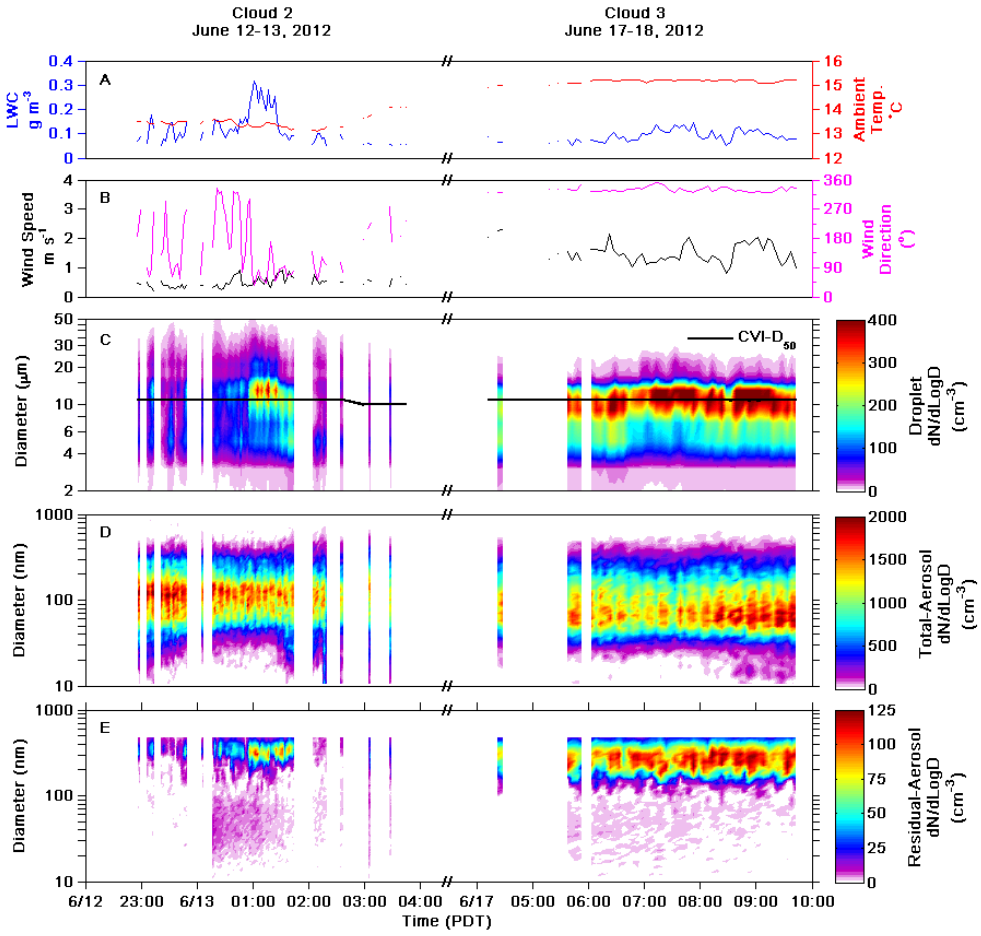

Figure 4.4: Time series data for both Cloud 2 (left side) and Cloud 3 (right side) showing; liquid water content (*LWC*, blue trace) and ambient temperature (red trace) in panel A; wind speed and direction in panel B; cloud droplet number size distributions with the $CVI - D_{50}$ (black trace) overlaid in panel C; the number size distribution for the total aerosol in panel D, and the residual aerosol in panel E. All data shown are five-minute averages and meet the criteria discussed in the text.

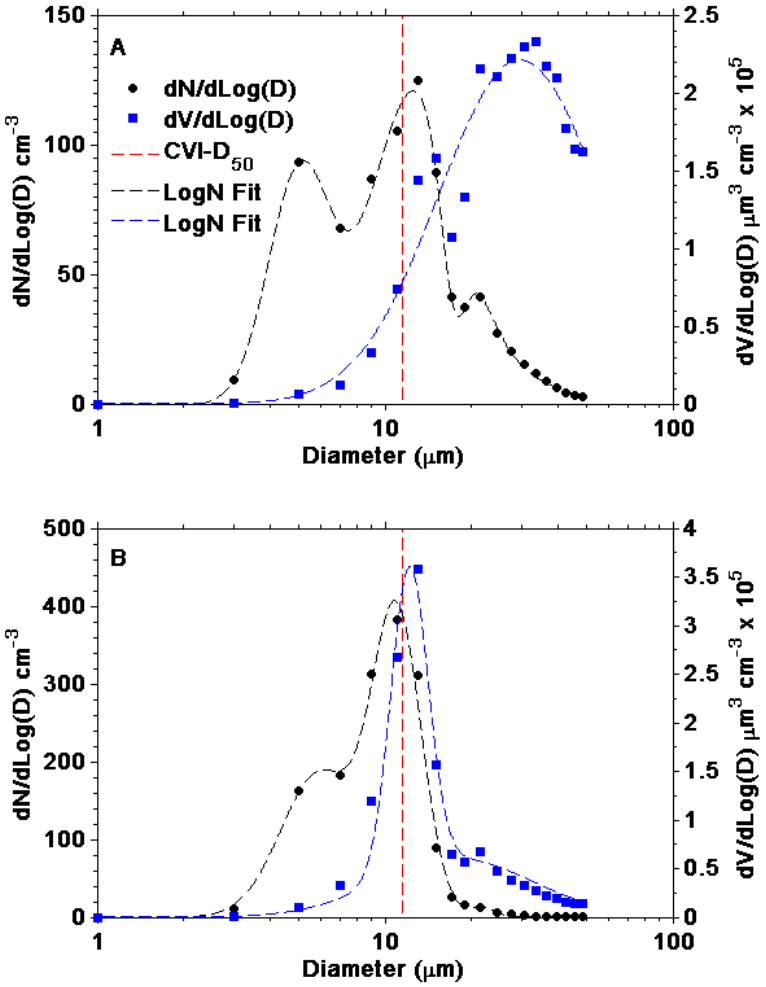

Figure 4.5: Average cloud droplet number size distributions for Cloud 2 (panel A) and Cloud 3 (panel B) measured by the FM-100 (black circles) and fit to a lognormal distribution function (black dashed lines). The average cloud droplet volume distributions (blue squares) and lognormal fits (blue dashed lines) are also shown for each cloud event. The $CVI - D_{50}$ is indicated on each panel by a red dashed line.

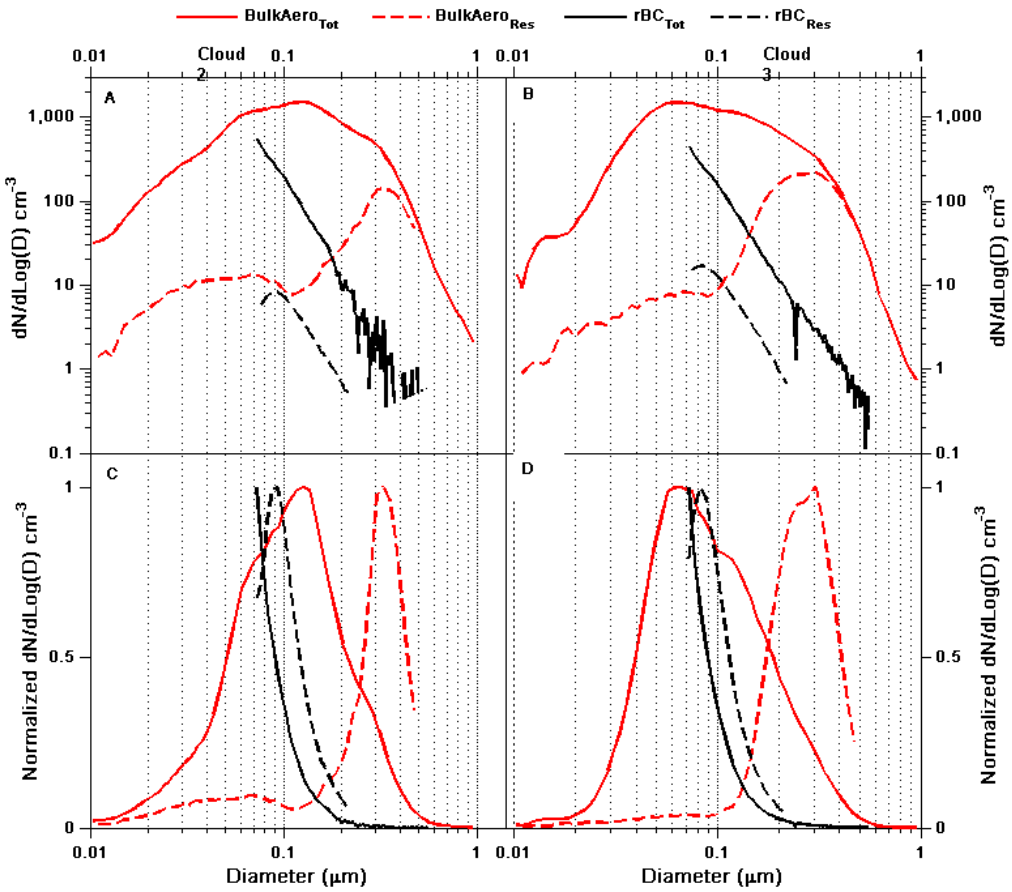

Figure 4.6: Summary of the averaged number size distributions for Cloud 2 (panels A and C) and Cloud 3 (panels B and D) for the total aerosol (red solid lines); residual aerosol (red dashed lines); total rBC as a function of core diameter (black solid lines); and residual rBC as a function of core diameter (black dashed lines). Both the aerosol and rBC for each cloud event are shown in two ways, a log scale (panels A and B) to highlight the relative differences between the aerosol and rBC as well as normalized to the respective maximum value (panels C and D) to highlight the shift in size distributions. All residual distributions have been corrected for CVI enhancement (see Section 4.3.1.3 and droplet losses (see Appendix B).

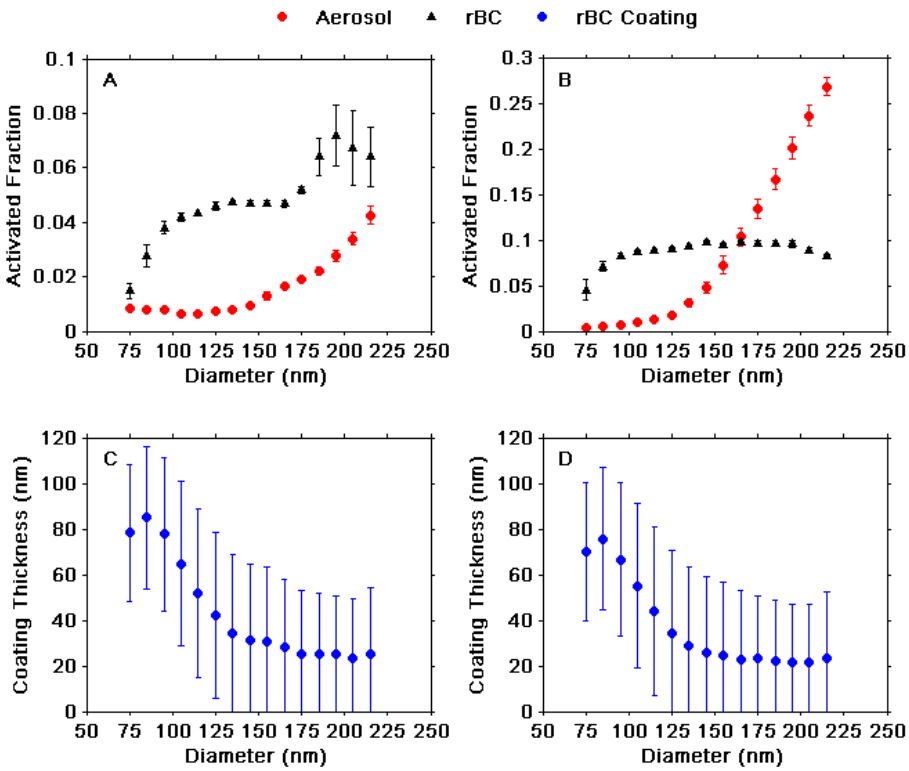

Figure 4.7: Shown in panels A and B are the mean size dependent activated fraction (AF) for the aerosol (red circles), and rBC (black triangles) for Clouds 2 and 3, respectively, where the error bars represent one standard deviation ($1\sigma_{std}$) of the mean AF. The bottom axes represent particle diameter for the aerosol and core diameter for rBC. Since the fraction of the cloud droplets sampled by the CVI was less than 100%, the calculated activated fractions should be considered as lower limits to the total AF during the two cloud events. Shown in panels C and D are the averaged rBC coating thicknesses (blue circle) in nm with $1\sigma_{std}$ as the error bars. Since only 50% of the rBC containing particles detected with the $SP2_{Res}$ were successfully fit with the LEO fitting procedure, the coating thicknesses shown in panels C and D are only from a subset (50%) of the rBC particles measured with the $SP2_{Res}$.

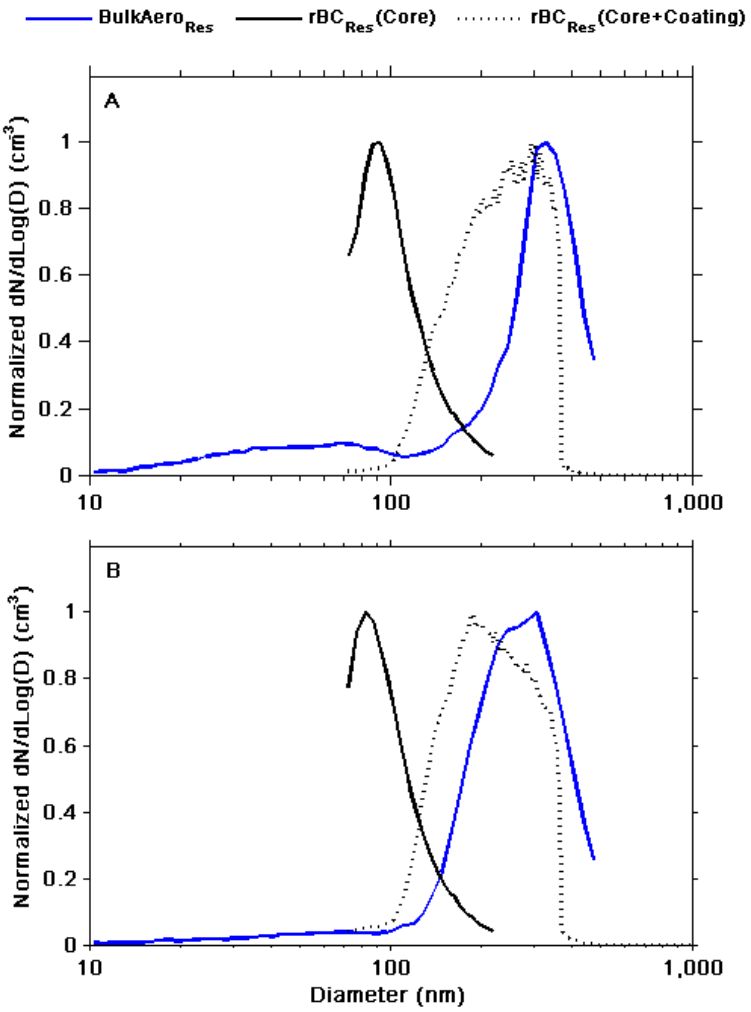

Figure 4.8: Normalized number size distributions from Cloud 2 (panel A) and Cloud 3 (panel B) for residual rBC as a function of particle diameter [rBC$_{Res}$(Core+Coating)]. The residual bulk aerosol distribution (BulkAero$_{Res}$) and rBC distribution as a function of core diameter [rBC$_{Res}$(Core)] are also shown for comparison. Since only 50% of the rBC containing particles detected with the SP2$_{Res}$ were successfully fit with the LEO fitting procedure, the rBC$_{Res}$(Core+Coating) shown in panels A and B are only from a subset (50%) of the rBC particles measured with the SP2$_{Res}$.

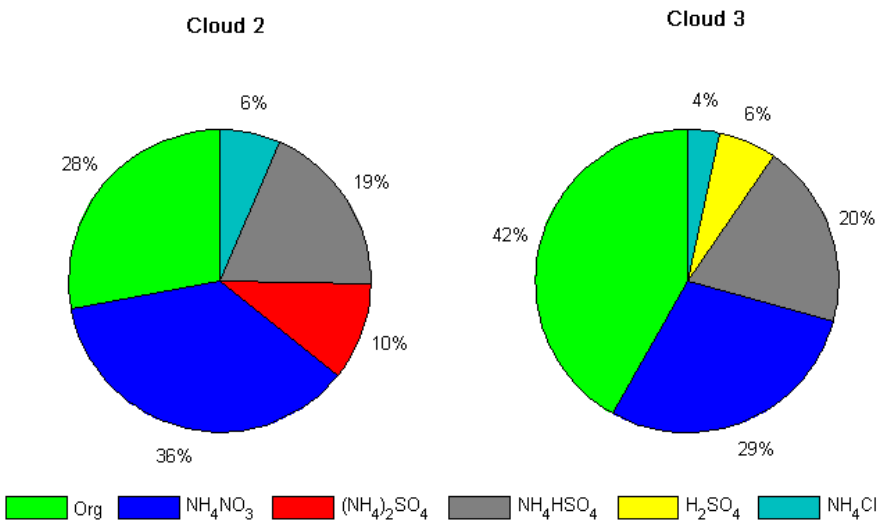

Figure 4.9: Sub-micrometer non-refractory average aerosol mass fractions for Clouds 2 and 3 based on an ion-pairing scheme (see Section 4.4.8.1 and Appendix A) and measured from a high resolution time-of-flight aerosol mass spectrometer.

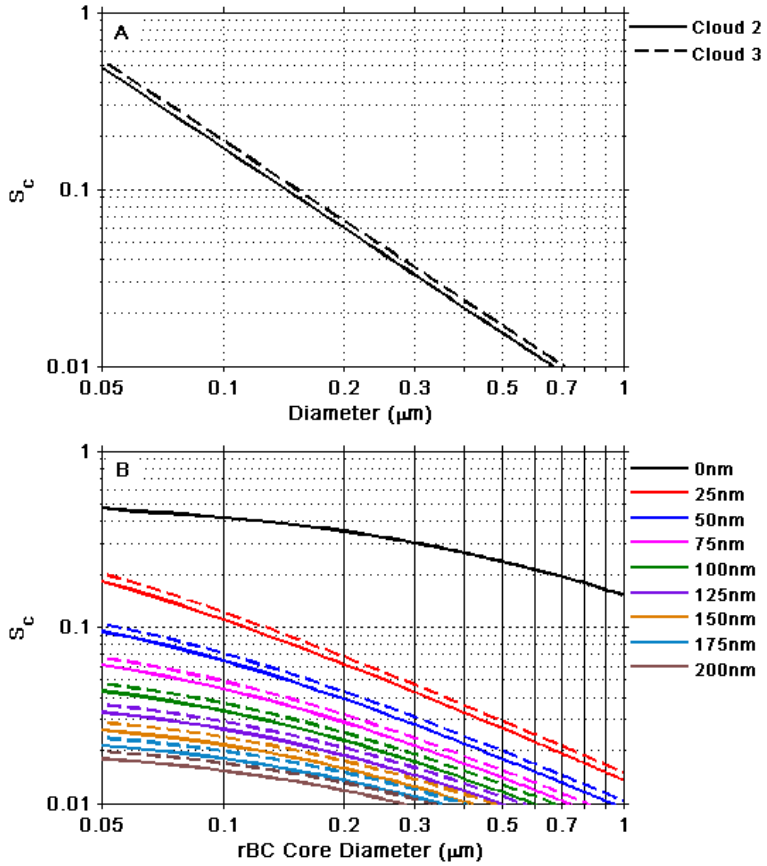

Figure 4.10: Panel A shows the critical supersaturation (S_C, black lines) as a function of particle dry diameter based on measured HR-ToF-AMS bulk compositions and an ion-pairing scheme. Panel B shows S_C as a function of rBC core diameters with coating thicknesses ranging from 0-200 nm. In panel B, the coatings are assumed to have the same composition as the bulk residual aerosol (Figure 4.9). The solid lines are for Cloud 2 and the dashed lines are for Cloud 3.

Table 4.1: Summary of cloud microphysical properties showing the average CVI cut-size ($CVI - D_{50}$) where the uncertainty stems from the calculated cut-size (see Section 4.3.1.2 for details); average liquid water content (LWC) and one standard deviation; and the cloud droplet number ($CDNC_{Tot}$) and volume (Vol_{Tot}) concentrations for droplets with diameters between 2-50 μm. Also shown is the number $\left(\frac{CDNC_{Samp}}{CDNC_{Tot}}\right)$ and volume $\left(\frac{Vol_{Samp}}{Vol_{Tot}}\right)$ fractions of droplets sampled, where $CDNC_{Samp}$ and Vol_{Samp} are the number and volume concentrations, respectively, for the fraction of droplets sampled.

Cloud #	Date Sampled	$CVI - D_{50}$ (μm)	LWC (g m^{-3})	$CDNC_{Tot}$ (cm^{-3})	$\left(\frac{CDNC_{Samp}}{CDNC_{Tot}}\right)$	Vol_{Tot} (μm^3 m^{-3})	$\left(\frac{Vol_{Samp}}{Vol_{Tot}}\right)$
2	12-13 June 2013 2043-1135 PDT	11.5 ±0.72	0.13 ±0.07	67.67	0.38	1.24E5	0.91
3	17-18 June 2013 2036-0752 PDT	11.6 ±0.72	0.09 ±0.02	145.8	0.24	8.88E4	0.68

Table 4.2: Averaged number (N) and mass (M) concentrations, modal parameters D_g and σ_g for aerosol and rBC particles during the two cloud events measured at Mt. Soledad. The subscripts *Tot* and *Res* represent measurements made from the total and residual inlets respectively.

	Cloud 2		Cloud 3	
	Aerosol	rBC	Aerosol	rBC
N_{Tot} (cm^{-3})	980.8	75.24	994.0	62.13
M_{Tot} (ng m^{-3})	-	73.41	-	61.83
$D_{g,Tot}$ (nm)	107.7	$<$70	80.54	$<$70
$\sigma_{g,Tot}$	1.577	-	1.703	-
N_{Res} (cm^{-3})	43.46	2.000	83.15	3.86
M_{Res} (ng m^{-3})	-	2.741	-	4.735
$D_{g,Res}$ (nm)	331.9	87.30	269.2	80.72
$\sigma_{g,Res}$	1.187	1.259	1.281	1.268

Chapter 5

Size-Resolved Activation of Refractory Black Carbon in Cloud Droplets at a Canadian High Elevation Site

5.1 Introduction

As mentioned in the previous chapter, several studies have looked at the activated fraction of BC mass in cloud droplets (Chýlek et al., 1996; Cozic et al., 2007; Hitzenberger et al., 2000, 2001; Kasper-Giebl et al., 2000; Sellegri et al., 2003). Reported values of the average BC mass activated fractions range from 0.06 to 0.8 (Cozic et al., 2007) (and references within), where lower values were typi-

cally seen at urban sites closer to anthropogenic emission sources, and the higher activated fractions were seen at more remote higher elevation sites where it is thought that the air mass is aged to some extent providing the BC an opportunity to form a hydrophilic coating. However, not all data are consistent with this picture. For example, Granat et al. (2010) has shown that BC was three times less efficiently activated compared to sulfate, even after a travel time of several days, suggesting that BC containing particles from India have retained much of their hydrophobicity after a travel time of several days. However, the conclusions stated in this study assumed that hygroscopicity controlled the removal of BC through wet scavenging, when a more important factor is particle size. Furthermore, the washout ratio, which is the metric used to interpolate scavenging efficiencies, was computed for BC mass and not number. Therefore, direct comparisons of their work and the work presented here are difficult to make.

Even though there have now been several studies on the activated fraction of BC mass in cloud droplets in the natural environment, only one size-resolved field study (Schroder et al., 2014), to the best of our knowledge, has been carried out (see Chapter 4). Additional studies on the activated fractions of BC in cloud droplets as a function of size are useful to test the current understanding of BC activation in cloud droplets and the CCN properties of BC in the atmosphere.

In this study we present data collected at a remote mountain site during the Whistler Aerosol and Cloud Study (WACS) that took place in 2010 (Macdonald et al., 2014) (manuscript in preparation). The size-resolved activated fractions of rBC were measured and compared to the size-resolved activated fractions of the

bulk aerosol during two cloud events.

5.2 Sampling Site

5.2.1 Site description

Sampling took place during the Whistler Aerosol and Cloud Study (WACS) during 2010, and occurred at the Whistler High Elevation Site (WHI). The WHI is located at the peak of Whistler mountain (50.06°N, 122.96°W) at an elevation of 2182 m a.m.s.l.. This site is approximately 120 km north of Vancouver, British Columbia, its nearest major urban center, and sits above the Whistler Village (650 m a.m.s.l.). A full description of the site and instruments present during this campaign can be found in the campaign overview paper (Macdonald et al., 2014). Briefly, there were two facilities used to house the instrumentation; a lift operator‘s hut, which includes a year round monitoring station maintained by Environment Canada (Ahlm et al., 2013; Leaitch et al., 2011; Macdonald et al., 2011; McKendry et al., 2010; Takahama et al., 2011); and a shipping container that was used only during the campaign. The cloud portion of the study took place from 1 July to 28 July 2010.

5.2.2 Inlets

Three inlets were used in this study (Figure 5.1), the total aerosol inlet and residual inlet were connected to instrumentation housed in the shipping container by a 3-way valve. During cloud-free periods of sampling the valve was switched so

that ambient air was sampled through the total aerosol inlet (Figure 5.1). When clouds were present the valve was manually switched so that droplet residuals were sampled through the residual inlet (Figure 5.1), which included a CVI as its intake (see Section 4.3.1). The total aerosol, which is the sum of both the residual and interstitial particles, was sampled through the total aerosol inlet (Figure 5.1). Droplets sampled through the total inlet were dried by evaporation as they entered a temperature controlled room, held at approximately room temperature (20-25 °C). The third inlet, labeled total rBC inlet in Figure 5.1, was the inlet connected to the lift operator‘s hut and was used to measure the total rBC. Similar to the total inlet, droplets sampled through the total rBC inlet were dried by evaporation as they entered the temperature controlled room, which on average was at 23.5 °C.

A CVI (see Section 4.3.1) sampled cloud droplets but excluded interstitial particles based on the principle of inertial separation (Noone et al., 1988). After separation from interstitial particles the droplets were dried by a warm dry counterflow as well as heated sections of the sample tubing, leaving only the residual particles of the cloud droplets to be sampled by downstream instrumentation.

The $CVI - D_{50}$ for the two clouds sampled during this study were calculated based on Equation 4.5 and were found to be approximately 10 μm for both clouds. Sampling through the CVI enhanced the particle concentrations sampled when compared to ambient concentrations. Enhancement factors (EF) for the two clouds sampled were calculated to be approximately 11 and 9 using Equation 4.7. To account for droplet losses during CVI sampling a droplet transmission (DT) factor was determined (see Appendix C). All residual distributions have been cor-

rected for both the enhancement of particles and droplet losses.

5.3 Experimental

5.3.1 Refractory black carbon measurements

Two SP2s (Droplet Measurement Technologies, Boulder, CO) were used to measure rBC (Figure 5.1). One SP2 was connected to the total rBC inlet and is referred to as the total SP2 ($SP2_{Tot}$), and the second SP2 sampled from the residual inlet and is referred to as the residual SP2 ($SP2_{Res}$) (see Chapter 3 for a more thorough description and details on the SP2 theory of operation). Both the $SP2_{Tot}$ and the $SP2_{Res}$ used in this study had a rBC size detection range of 70 to 210 nm VED. As discussed in Section 3.5 the SP2 can be used to measure the thickness of any coating surrounding the core of a rBC particle if the elastic scattered light from the particles is measured with a split detector. However, the split detector on the SP2 connected to the residual inlet was not functioning throughout this study. Therefore, no coating thickness analysis was possible.

5.3.2 Size distribution measurements of the bulk aerosol

Bulk aerosol size distributions (here bulk aerosol refers to all aerosol particles regardless of composition) from the total aerosol inlet were measured with a wide range particle spectrometer (Liu et al., 2010a) (WPS, model 1000XP, MSP, Shoreview, MN), which combines a DMA coupled to a CPC and an optical particle counter (OPC) to provide particle counts for particles with diameters between

10 nm to 10 μm. For this analysis, particles with diameters of up to 500 nm were taken from the DMA CPC counts and all diameters greater than 500 nm were taken from the counts recorded by the OPC portion of the instrument. Size distributions of the residual bulk aerosol, sampled from the residual inlet, were measured with an ultra-high sensitivity aerosol spectrometer (UHSAS, Droplet Measurements Technologies, Boulder, CO). The UHSAS sampled particles between 0.06 and 1 μm every 10 seconds. These measurements have been discussed in further detail by Pierce et al. (2012) and Macdonald et al. (2014).

5.3.3 Back trajectories

Air mass back trajectories were obtained using the NOAA HYSPLIT model (Draxler and Rolph, 2012; Rolph, 2012). For the trajectory calculations the National Centers for Environmental Predictions EDAS meteorological dataset was used. All trajectories were calculated at 10 m a.g.l., 24 hours backwards in time and at hourly intervals for the entire duration of cloud sampling.

5.3.4 Cloud properties

A fog monitor (FM-100, model 100, Droplet Measurement Technologies, Boulder, CO), which is a forward scattering optical spectrometer, was stationed on top of the container providing an in-situ measurement of the cloud droplet number concentration (CDNC) and the liquid water content (LWC) present. Droplets with diameters between 2 and 50 μm were counted into 20 discrete size bins with a one-second time resolution (Eugster et al., 2006).

5.4 Results and Discussion

Two cloud events are analyzed in this study: the first cloud event took place on 2 July 2010 10:48 to 12:02 PST and is referred to as Cloud 1, and the second cloud event was sampled from 12 July 2010 07:38 to 11:15 PST and is referred to as Cloud 2.

5.4.1 Back trajectories

The 24 hour back trajectories that arrived at the onset of each cloud event as well as at every subsequent hour until the end of the event are shown in Figure 5.2. According to Figure 5.2 panels A and B, the trajectories during Cloud 1 arrived on-site roughly from the west, whereas the trajectories for Cloud 2 arrived at the peak from the northwest. The trajectories calculated for Cloud 1 and 2 did not pass over any heavily populated regions, suggesting little influence from recent fresh urban emissions. The corresponding vertical profiles for each of the air masses sampled are shown in Figure 5.2 panels C and D. In general, both air masses show some level of vertical lifting prior to being sampled.

Forest fires reported within the previous 24 hours by the Canadian Wildland Fire Information System (CWFIS, vertical red triangle) as well as fires detected by the Moderate Resolution Imaging Spectroradiometer (MODIS, horizontal red triangle) are also plotted on Figure 5.2 panels A and B to indicate if the air masses sampled may have been influenced by biomass burning aerosols. No fires were reported within the 24 hours prior to the sampling of Cloud 1, indicating there was likely no influence from biomass burning aerosols immediately preceding this

event. However, several forest fires were reported within the 24 hours prior to the sampling of Cloud 2 and within roughly 500 km of the sampling site, suggesting the possibility of some biomass burning influence. Trace gas measurements of acetonitrile (Macdonald et al., 2014), a marker for biomass burning (Holzinger et al., 2005), show a sharp rise in the mixing ratio at the beginning of Cloud 2, further suggesting that the air mass sampled during Cloud 2 most likely had some influence from biomass burning aerosols.

5.4.2 Meteorological conditions and cloud properties

Data were classified as in-cloud and included for analysis if the one-minute-averaged LWC was greater than 0.05 g m^{-3} and if the one-minute-averaged CVI counterflow rate varied by less than $\pm 5\sigma_{std}$ of the mean counterflow rate. This filtering of the data removed periods of unstable flows and regions of "patchy" clouds as much as possible (Cozic et al., 2007).

Measured cloud properties as a function of time are shown in Figure 5.3 panels A and B, where Cloud 1 is shown on the left side and Cloud 2 is shown the right side of the plot. Panel A shows the LWC as a function of time for each of the clouds. Averaging the data shown in panel A gave LWC values of 0.07$\pm$0.04 and 0.11$\pm$0.06 g m^{-3} for Clouds 1 and 2, respectively. Figure 5.3 panel B shows the droplet number distributions as a function of time for each of the clouds with the calculated $CVI - D_{50}$ overlaid as a solid black line. The time-dependent data shown in Figure 5.3 panel B were used to calculate the average droplet number distributions for each cloud event (Figure 5.4). Integration of the lognormal fits

between 2 and 50 μm in Figure 5.4 gave cloud droplet number concentrations (CDNC) of 194 cm^{-3} and 258 cm^{-3} for Clouds 1 and 2, respectively. Applying the $CVI - D_{50}$ to the droplet distributions shown in Figure 5.4 indicates that 28% and 41% of the droplet number were sampled during Clouds 1 and 2 respectively. Sampling only a fraction of the cloud droplet number distribution indicates that the results presented in this study apply only to the larger diameter cloud droplets. Averaged relevant properties of Clouds 1 and 2 are summarized in Table 5.1 for reference.

5.4.3 Size distributions

Average size distributions of the bulk aerosol and rBC particles, measured from the total and residual inlets for both clouds are presented in Figure 5.5. Data are plotted in two ways; on a log scale (panels A and C), and normalized to the respective maximums (panels B and D). Table 5.2 summarizes the results of the size distribution analysis.

5.4.3.1 Size distributions measured from the total inlet ($\mathbf{BulkAero_{Tot}}$ and $\mathbf{rBC_{Tot}}$)

The average size distribution of the bulk aerosol measured with the total aerosol inlet (referred to here as $BulkAero_{Tot}$) and the average size distributions of rBC measured with the total rBC inlet (referred to here as rBC_{Tot}) are shown in Figure 5.5. The $BulkAero_{Tot}$ size distributions (red solid lines in Figure 5.5) for both clouds show two distinct modes with D_g, as determined by fitting a lognormal function to the data, of 78 and 47 nm for the smaller diameter mode and 148 and

137 nm for the larger diameter mode (Table 5.2) for Cloud 1 and 2 respectively. Integration of these number distributions from 10 nm to 1 μm resulted in total number concentrations (N_{Tot}) of 736 and 376 cm^{-3} for Clouds 1 and 2, respectively. The size distributions of the BulkAero$_{\mathrm{Tot}}$ as a function of time are also shown in Figure 5.3 panel C for comparison.

The average rBC$_{\mathrm{Tot}}$ size distributions for each cloud are also shown in Figure 5.5 (black solid lines). Assuming that the rBC distributions follow a lognormal function the D_g values are less than 70 nm, which is below the detection limit of the SP2s. Integration of the rBC number distributions, for core $VEDs$ between 70 and 210 nm, results in an N_{Tot} of 8.1 cm^{-3} during Cloud 1 and 1.6 cm^{-3} during Cloud 2. The total mass (M_{Tot}) of rBC was found to be 8.9 and 2.1 ng m^{-3} for Clouds 1 and 2, respectively, assuming a density of σ_{bc}=1.8 g cm^{-3}.

5.4.3.2 Size distributions measured from the residual inlet (BulkAero$_{\mathrm{Res}}$ and rBC$_{\mathrm{Res}}$)

Average size distributions of the bulk aerosol measured from the residual inlet (referred to here as BulkAero$_{\mathrm{Res}}$), are shown in Figure 5.5 (red dashed lines). Applying lognormal fits to the BulkAero$_{\mathrm{Res}}$ yields D_g values of 122 and 128 nm for Clouds 1 and 2, respectively. The D_g values found for the BulkAero$_{\mathrm{Res}}$ distributions indicate that the majority of the particles activated into cloud droplets were from the larger diameter mode of the BulkAero$_{\mathrm{Tot}}$ size distributions. Integration of the BulkAero$_{\mathrm{Res}}$ size distributions between 60 nm and 1 μm gave measured cloud residual number concentrations (N_{Res}) of 91 and 77 cm^{-3} during Clouds 1 and 2, respectively.

Average rBC_{Res} distributions are shown in Figure 5.5 (black dashed lines), and, assuming these distributions follow a lognormal function, the D_g values would be below the detection limit of the SP2 (70 nm), similar to the rBC_{Tot}. Integration of these distributions, for rBC particles with core $VEDs$ between 70 and 210 nm, result in N_{Res} values of 2 cm^{-3} and 0.3 cm^{-3}, and residual mass concentrations (M_{Res}) were found to be 2.1 and 0.4 ng m^{-3} for Clouds 1 and 2, respectively.

5.4.4 Size-resolved activated fractions

The bulk aerosol and rBC size-resolved activated fraction, $AF(DP)$, was calculated similar to Section 4.4.4 using Equation 4.8. In order to account for differences in bin widths counted by the WPS and UHSAS a spline interpolation algorithm was applied to all distributions prior to calculating $AF(DP)$. The $CF(DP)$ in this study represents the size-resolved correction factor that accounts for differences in instrument sensitivity, which were calculated by taking the ratio of the total bulk aerosol number distribution measured from the WPS to the residual number distribution measured from the UHSAS during periods of cloud-free sampling, when the two instruments should have been measuring the same concentrations. The determination of DT in this study is discussed in Appendix C.

Figure 5.6 shows the calculated $AF(DP)$ for the bulk aerosol (red circles) and rBC (black triangles) for both clouds sampled, where $AF(DP)$ of the bulk aerosol was plotted as a function of particle diameter and the rBC size-resolved activated fractions were plotted as a function of rBC core VED. The error bars shown in

Figure 5.6 are taken as $1\sigma_{std}$ of the mean AF determined within each size bin. The AF values show a dependence on size for both the bulk aerosol and rBC during both clouds. The AF of rBC ranged from approximately 0.2 at the smallest size bin (70 to 80 nm) in Cloud 1 to 0.6 at the largest size bin of 200 to 210 nm during Cloud 2. Since the fraction of droplets sampled by the CVI was $<100\%$, the calculated AF should be considered as a lower limit to the total fraction activated during these two cloud events.

The size-resolved activated fractions of rBC cores shown in Figure 5.6 also indicate that even the small 70 nm rBC cores are efficiently activated. Although, since rBC core diameter is not the only factor that needs to be considered in CCN ability and the coating thicknesses could not be determined for these rBC cores, the extent to which the overall particle size influences the activation of these particles could not be investigated. Since 70 nm cores (uncoated) are only expected to be activated at relatively high cloud supersaturations ($\approx 1\%$, see Figure 4.10), it is likely that the rBC cores here were coated with soluble material. During Cloud 1 the rBC activated more efficiently than the bulk aerosol for all sizes. This observation also strongly suggests that the rBC particles during Cloud 1 were coated with soluble material.

5.5 Comparison with Previous Measurements

The study described in Chapter 4 is the only other study in which the size-resolved activation of rBC was measured. In that study, there was also a significant quantity of smaller (sub-100 nm) diameter rBC particles that were activated into cloud

droplets, a result that is consistent with the current study. The previous study showed that rBC cores with diameters less than 100 nm that were activated in cloud droplets had thick coatings ranging from approximately 45 to 115 nm.

Although there has only been one previous study to measure size resolved activation of rBC in cloud droplets, there have been several previous studies that have investigated the average BC mass activated fraction (Cozic et al., 2007; Hitzenberger et al., 2000, 2001; Kasper-Giebl et al., 2000; Sellegri et al., 2003). However, in these studies size-resolved information was not obtained, and only the total activated fraction of BC mass over the entire size range measured was reported. For comparison purposes, we calculated the average BC mass activated fractions for both clouds measured at Whistler by taking the ratio of the rBC residual mass (M_{Res}) to the rBC total mass (M_{Tot}). Using this method, and values for M_{Res} and M_{Tot} shown in Table 5.2, resulted in average BC mass activated fractions of 0.24 and 0.19 for Clouds 1 and 2 respectively. Since less than 100% of the droplet number distribution was sampled for both Clouds 1 and 2, these activated fractions of rBC mass are likely lower limits to the true activated fractions. Another uncertainty, when determining the mass activated fractions, is the fraction of the total mass sampled by the SP2 instruments. Shown in Figure 5.7 are the rBC mass distributions sampled from both the residual and total inlets. By assuming that the mass distributions are lognormal, Figure 5.7 suggests that the SP2s captured most, but not all, of the rBC mass during both of the cloud events.

In Table 5.3 we compare the activated fractions of rBC mass measured here with the average activated fraction of BC mass determined at other remote moun-

tain sites. The average activated fractions of rBC mass for clouds measured at Whistler are smaller than the values reported at other remote mountain sites. The differences may be due to the fact that less than 100% of the droplet number distributions were sampled in the current study and therefore, the activated fractions of rBC mass likely represent lower limits.

As discussed above, the air mass for Cloud 2 was likely influenced by biomass burning particles. A few studies have shown that freshly emitted biomass burning aerosols can have large diameters as well as reasonably high κ values making them fairly hygroscopic, and therefore efficient CCN (see Chapter 2) at or near the point of emission (Petters et al., 2009; Pratt et al., 2011). Andreae and Rosenfeld (2008) summarized previous studies of CCN properties of biomass burning particles and concluded that, in general, the CCN efficiency of biomass burning particles increases with aging. Combining these previously reported results, biomass burning aerosols, whether freshly emitted or aged, can act as efficient CCN. The size-resolved activated fractions measured here, for both bulk aerosol and rBC, appear to be consistent with the conclusions from these previous studies.

5.6 Summary and Conclusions

The size-resolved AF of rBC was measured for two clouds at the peak of Whistler Mountain during the WACS-2010 campaign. Back trajectories calculated for both clouds showed that the air masses sampled did not travel over or near highly populated areas within the previous 24 hours. The first cloud sampled had no influence from biomass burning aerosols within the previous 24 hours. However, 24 hours

prior to sampling Cloud 2, several forest fires were reported or detected within the vicinity of the sampling site. Elevated mixing ratios of acetonitrile were also detected at the beginning of the cloud, indicating that the air mass sampled during Cloud 2 likely had at least some influence from biomass burning aerosols.

The fractions of bulk aerosol and rBC that activated both show a dependence on size from the two clouds measured. The AF of rBC ranged from approximately 0.2 at the smallest size bin (70 to 80 nm) to 0.6 at the largest size bin (200 to 210 nm). Since the fraction of droplets sampled by the CVI was less than 100%, the calculated AF should be considered as lower limits to the total fractions activated during these two cloud events. The size-resolved AF of rBC cores shown in Figure 5.6 indicate that even the small 70 nm rBC cores are efficiently activated. Since 70 nm uncoated cores are only expected to be activated at relatively high cloud supersaturations, it is likely that the rBC cores were coated with soluble material. In addition, during Cloud 1 the fraction of rBC cores was more efficiently activated than the bulk aerosol for all diameters measured. This result strongly suggests that large hygroscopic coatings surrounded these cores since, as seen in Chapter 4, the overall rBC particle diameter likely is the dominant factor in determining the CCN ability. These results should be useful for testing models and parameterizations used to predict activation of BC in cloud droplets. For example, the size resolved activated fractions presented in this chapter could be used to test simulated activated fractions at similar supersaturations and similar elevations.

5.7 Chapter 5 Figures and Tables

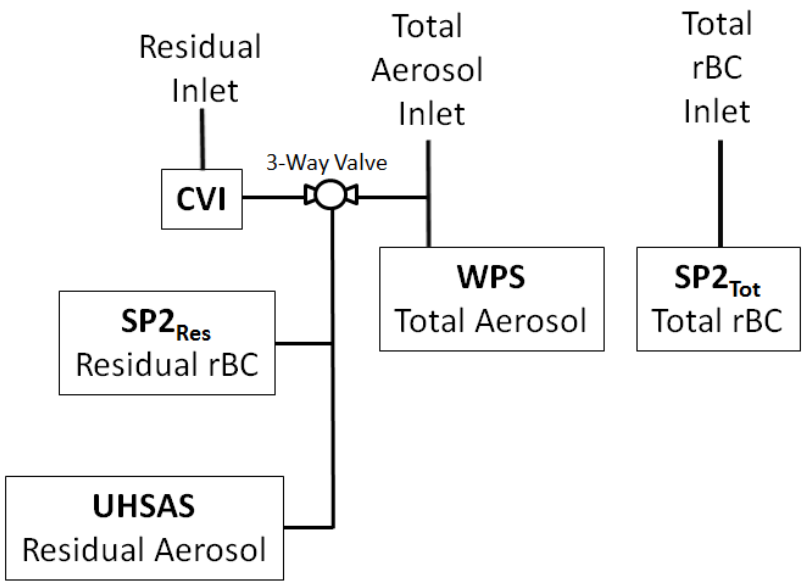

Figure 5.1: Schematic showing the configuration of the inlets and relevant instrumentation used in this study.

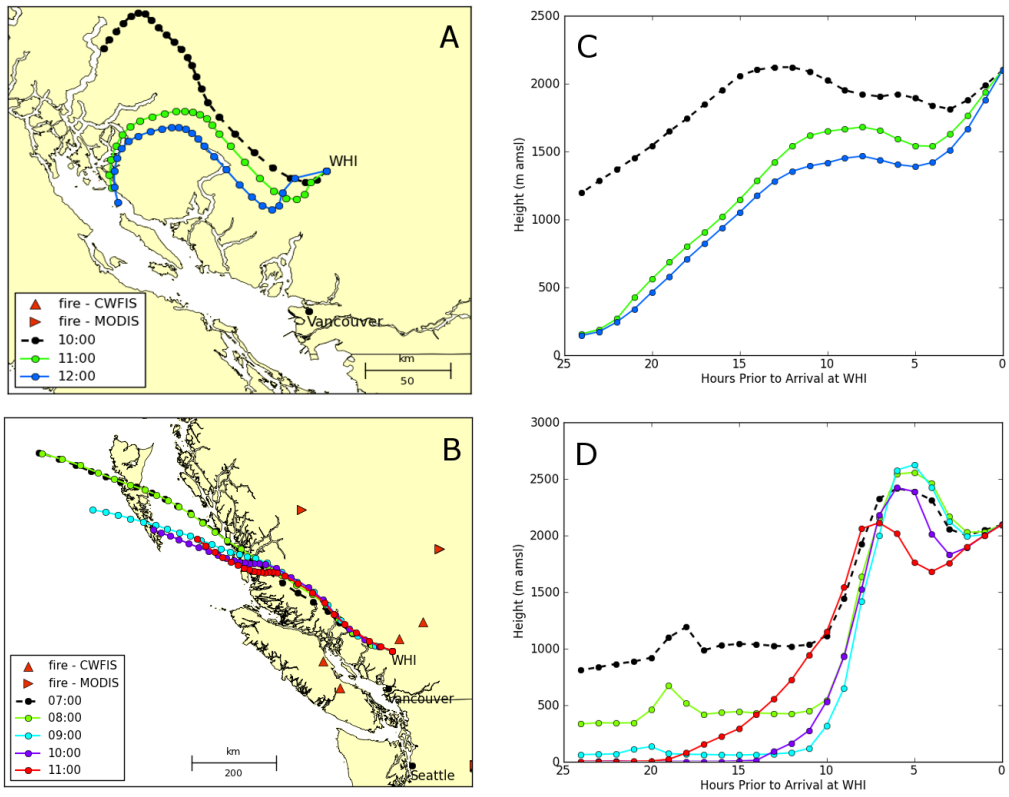

Figure 5.2: HYSPLIT 24hr back trajectories. Panels A and C are trajectories ending at hourly intervals for Cloud 1 (2 July 10:00 to 12:00 PST); panels B and D are trajectories ending at hourly intervals for Cloud 2 (12 July 07:00 to 11:00 PST). All back trajectories started at 10 m above ground level. Red vertical triangles are fires reported by the Canadian Wildland Fire Information System (CWFIS) and red horizontal triangles are fires detected from MODIS for all fires within 24 hours prior to the start of the cloud. Panels C and D show the vertical profiles over the same hourly intervals shown in panels A and B.

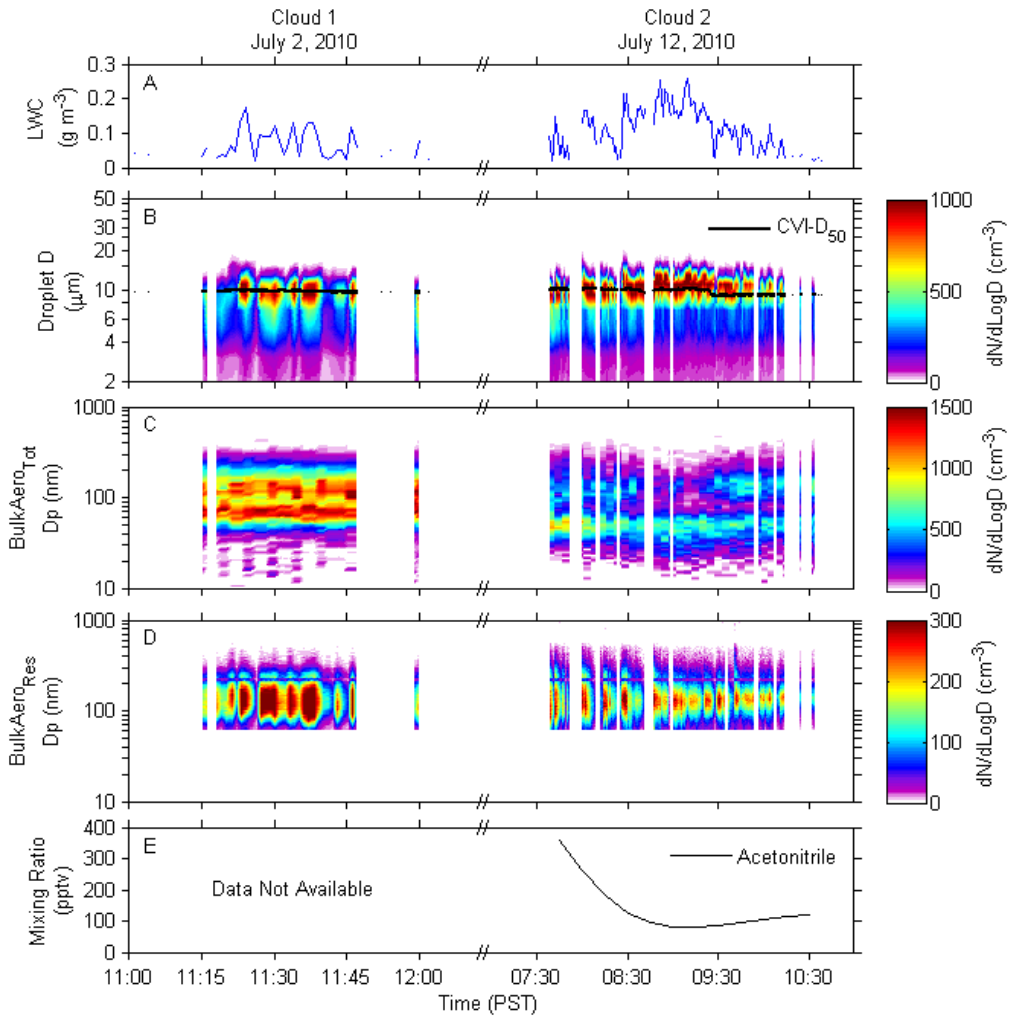

Figure 5.3: Time series data for Cloud 1 (left side) and Cloud 2 (right side) showing; liquid water content (LWC) in panel A; cloud droplet number size distributions with the $CVI-D_{50}$ (black trace) overlaid in panel B; the number size distributions for the total bulk aerosol in panel C, the residual bulk aerosol in panel D, and acetonitrile mixing ratio in panel E. All data shown in panels A to D are one-minute averages and meet the criteria discussed in Section 5.4.2. Data in panel E are 15-minute averages.

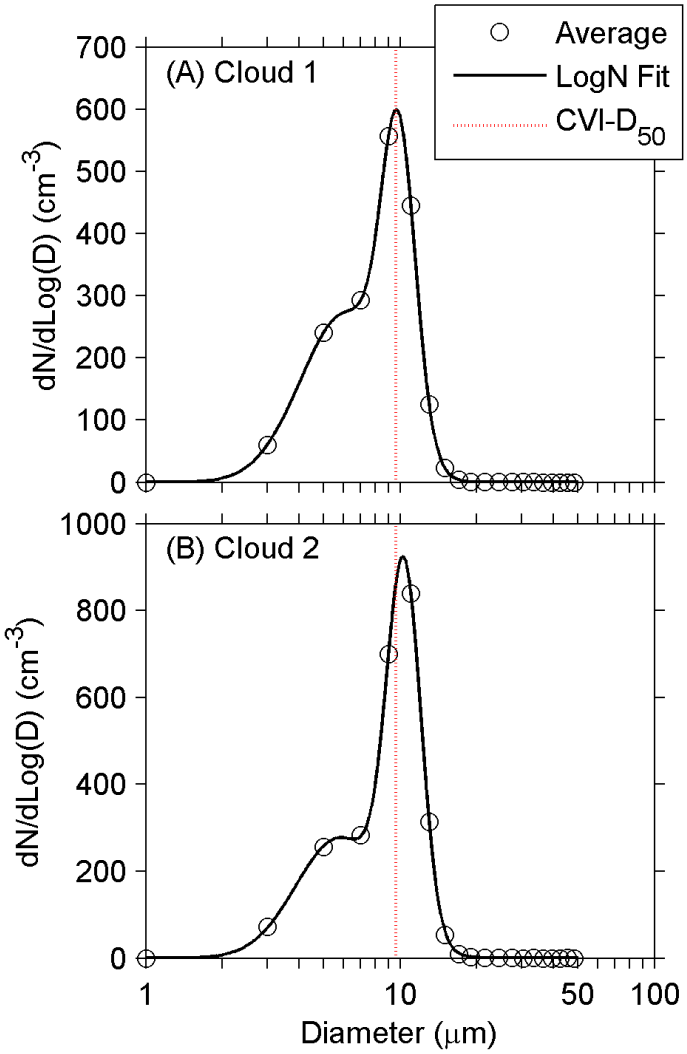

Figure 5.4: Average cloud droplet number size distributions for Cloud 1 in panel A and Cloud 2 in panel B (black circles) and fit to a lognormal distribution function (black lines). The $CVI - D_{50}$ is indicated in each panel by a red line.

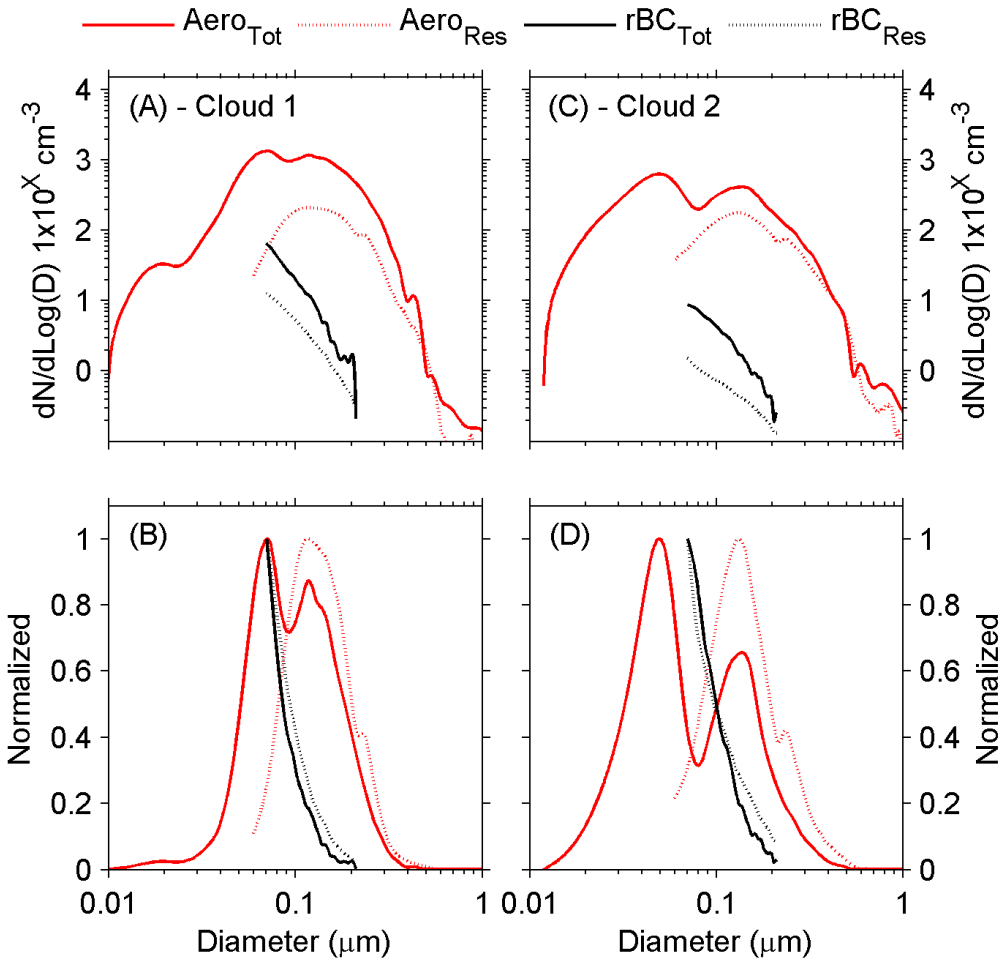

Figure 5.5: Summary of the averaged number size distributions for Cloud 1 (panels A and B), and Cloud 2 (panels C and D) for the total bulk aerosol (red solid lines); residual bulk aerosol (red dashed lines); total rBC as a function of core diameter (black solid line); and residual rBC as a function of core diameter (black dashed lines). Both the aerosol and rBC for each cloud are shown in two ways, a log scale (panels A and C) as well as normalized to the respective maximum values (panels B and D). All residual distributions have been corrected for the CVI enhancement (see Section 4.3.1.3) and droplet losses (see Appendix C)

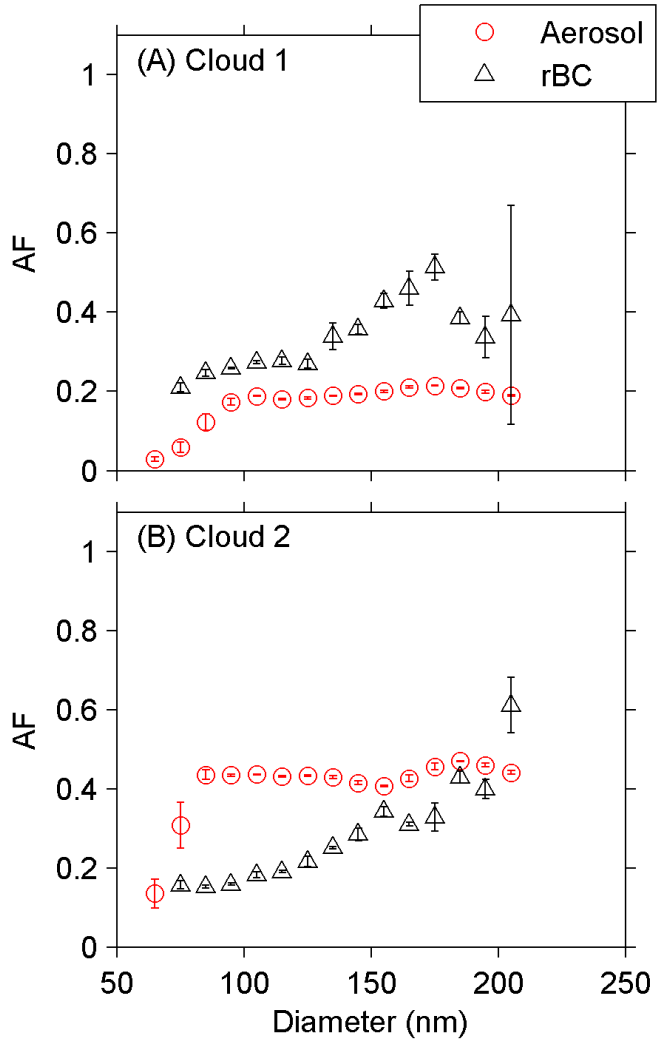

Figure 5.6: Mean size dependent activated fractions (AF) for the bulk aerosol (red circles) and rBC (black triangles) for Clouds 1 and 2 in panels A and B, respectively. The error bars represent one standard deviation of the mean activated fraction within each 10 nm bin. The bottom axis represents particle diameter for the bulk aerosol and core diameter for rBC. Since the fraction of cloud droplets sampled by the CVI was less than 100%, the calculated activated fractions should be considered as lower limits to the total activated fraction.

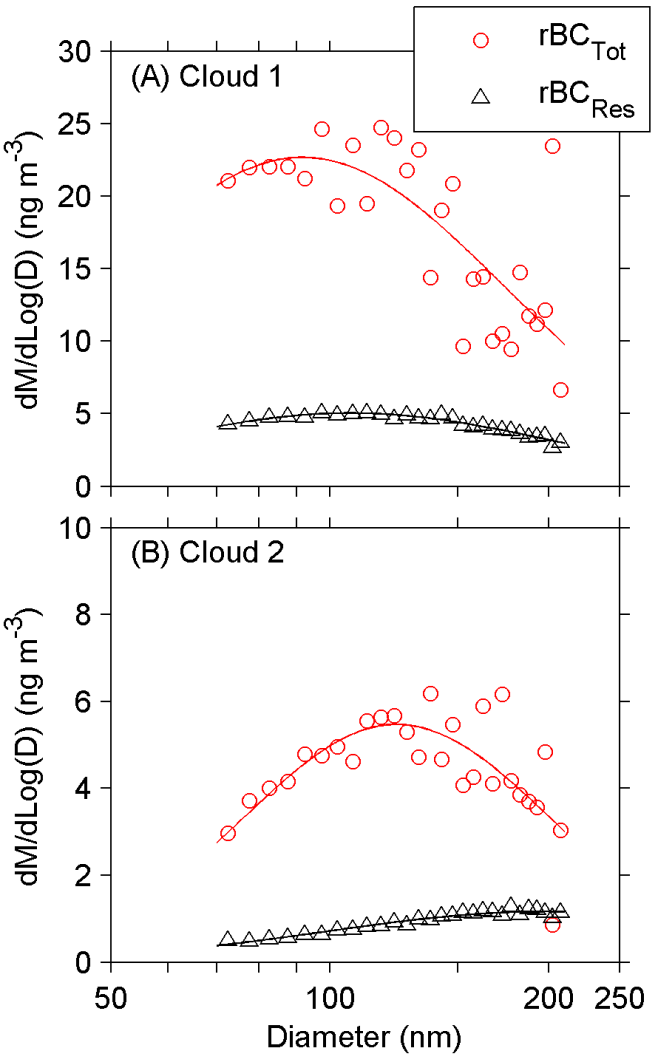

Figure 5.7: Averaged rBC mass distributions as a function of rBC core diameters during Cloud 1 (panel A) and Cloud 2 (panel B) for the total rBC (rBC_{Tot}, red circles) and the residual rBC (rBC_{Res}, black triangles). The solid lines are fits using a lognormal function.

Table 5.1: Summary of cloud microphysical properties showing the dates and times sampled; the average CVI cut-size ($CVI - D_{50}$), where the uncertainty comes from the calculated cut-size; average liquid water content (LWC) and one standard deviation; total cloud droplet number concentration ($\mathrm{CDNC_{Tot}}$); and the number fraction of droplets sampled ($\mathrm{CDNC_{Samp}/CDNC_{Tot}}$), where $\mathrm{CDNC_{Samp}}$ is the droplet number concentration greater than the CVI cut-size.

Cloud #	Date Sampled	$CVI - D_{50}$ (μm)	LWC (g m^{-3})	$\mathrm{CDNC_{Tot}}$ (cm^{-3})	$\left(\frac{CDNC_{Samp}}{CDNC_{Tot}}\right)$
1	2 July 2010 1048-1202 PST	9.67 ±0.08	0.07 ±0.04	194.14	0.28
2	12 July 2010 0738-1115 PST	9.63 ±0.48	0.11 ±0.06	258.36	0.41

Table 5.2: Average number (N) and mass (M) concentrations, modal parameters D_g and σ_g for bulk aerosol and rBC particles during Clouds 1 and 2. The subscripts *Tot* and *Res* represents measurements made from the total and residual inlets respectively. All values reported for residual particles have been corrected for the CVI enhancement (see Section 4.3.1.3) and droplet losses (see Appendix C)

	Cloud 1		Cloud 2	
	Aerosol	rBC	Aerosol	rBC
N_{Tot} (cm^{-3})	736.3[a]	8.1[c]	375.6[a]	1.6[c]
M_{Tot} (ng m^{-3})	-	8.9[c]	-	2.1[c]
$D_g(\sigma_g)_{\mathrm{Tot}}$ (nm)	Mode 1: 77.8 (1.4) Mode 2: 148.3 (1.4)	<70	Mode 1: 46.8 (1.3) Mode 2: 137.1 (1.3)	<70
N_{Res} (cm^{-3})	90.5[b]	2.0[c]	77.2[b]	0.3[c]
M_{Res} (ng m^{-3})	-	2.1[c]	-	0.4[c]
$D_g(\sigma_g)_{\mathrm{Res}}$ (nm)	122.2 (1.2)	<70	127.9 (1.2)	<70

[a] 10 to 1000 nm
[b] 60 to 1000 nm
[c] 70 to 220 nm

Table 5.3: Summary of average black carbon mass activated fractions (AF) measured at other remote mountain locations (adapted from Cozic et al. (2007)), as well as from this study.

Location	AF	Site Elevation	Reference	Dates
Puy de Dôme (France)	0.33	1465 m	Sellegri et al. (2003)	Feb. - Apr. 2001
Rax (Austria)	0.54	1644 m	Hitzenberger et al. (2001)	Apr. 1999 & Mar. 2000
Mt. Sonnblick (Switzerland)	0.45	3106 m	Kasper-Giebl et al. (2000)	Sept. 1995
	0.75		Hitzenberger et al. (2000)	Sept 1996 & Apr. - May 1997
Junfraujoch (Switzerland)	0.61	3850 m	Cozic et al. (2007)	Jul. - Aug. 2004
Mt. Whistler	0.24	2182 m	This work	2 July 2010
	0.19			12 July 2010

Chapter 6

Measurements of Refractory Black Carbon at a High Elevation Mountain Site during 2009, 2010, and 2012

6.1 Introduction

In order to assess the role of BC particles in climate and health, knowledge of the properties of BC (e.g. size distribution, mass loading, and mixing state) in the atmosphere is needed, and this information needs to be represented accurately in atmospheric models. In this study we present measurements of rBC at the Whistler High Elevation Site (WHI) in British Columbia, Canada. The data were

collected during the summertime of 2009 and 2010, as well as the spring of 2012. WHI is a remote station which is often in the free troposphere (FT). It sees little influence from any nearby large urban centers (Macdonald et al., 2011), but in the summer it can be impacted by local and regional biomass burning (Takahama et al., 2011).

A number of studies have measured BC mass concentrations in remote locations. In the INTEX-B campaign a SP2 was used to measure rBC during flights over the US Pacific Northwest (Dunlea et al., 2009). In the INTEX-B campaign, the sampled air was classified into several groups, one of which was the background (free troposphere) aerosol. Mass concentrations in the FT were low relative to air masses influenced by regional sources and averaged 90 ng m^{-3}. In the HIAPER Pole-to-Pole Observations (HIPPO) project, five sets of flights were conducted between 2009 and 2011 over the remote Pacific with an SP2 on board (Kipling et al., 2013; Schwarz et al., 2010b, 2013; Shen et al., 2014). In these, rBC mass concentrations ranged from 1-40 ng m^{-3} for latitudes of 20-60 °N and altitudes up to 5km. Measurements of rBC mass concentration have also been performed at the remote Jungfraujoch station in Switzerland (3580 m a.m.s.l.). There rBC mass concentrations in late winter ranged from median values of 8.11 to 24.08 ng m^{-3} (scaled by a factor of $\approx$1.6 for STP) for FT background or boundary layer aerosol respectively (Liu et al., 2010b)

In this study a seasonal and time-of-day approach is combined with back trajectory analysis to separate periods of FT sampling from the general dataset. Periods of biomass burning influence are also identified using chemical speciation of

the total aerosol.

6.2 Site, Sampling and Analysis

6.2.1 Site description

Sampling for these experiments also took place at WHI (see Section 5.2.1). Since Whistler Mountain is the location of a large ski resort, the periodic arrival of snow-grooming machines, snowmobiles, and trucks near the sampling site results in very sharp spikes in the rBC mass and number concentrations. The data have been filtered to remove these spikes and, although it is believed that all of these have been removed from the dataset, the possibility that some lesser influences remain means that the data presented represents an upper limit for mass and number concentration.

6.2.2 Refractory black carbon mass measurements

For this study two SP2s (see Chapter 3 for details on the SP2) were used during the three collection periods . SP2-1 was used during 2009 and 2010 and SP2-2 was used during 2012. Both SP2s were calibrated with Aquadag® using the procedure discussed in Section 3.3. Using a BC density of σ_{bc}=1.8 g cm^{-3} $VEDs$ were also calculated from the measured masses of ambient particles using Equation 3.1.

One issue that arises with the SP2 is reduced detection efficiency at smaller rBC diameters (Laborde et al., 2012; Schwarz et al., 2010a). In this study SP2-1 had 100% detection efficiency down to an rBC mass of 1.26 fg (110 nm VED) and

reached 50% detection efficiency at 0.41 fg (76 nm VED). SP2-2 had 100% detection efficiency down to an rBC mass of 0.68 fg (90 nm VED) and reached 50% detection efficiency at 0.26 fg (66 nm VED). Because of this we have used 0.41 fg (76 nm VED) as a lower detection limit. At this mass the detection efficiency of SP2-2 was approximately 80%. We have not attempted to correct for this issue since the fraction of the total rBC mass arising from these small particles is not known at all times, and because the shape of the detection efficiency curve can vary with particle morphology and mixing state (Laborde et al., 2012).

6.2.3 Refractory black carbon coating thickness measurements

rBC particles were analyzed to determine the thickness of any coating surrounding the core. Section 3.5 describes, in detail, the procedure used to calculate the coating thickness.

In this work a coating analysis was done for two subsets of the full data record. These were particles measured during periods of biomass burning influence and particles measured during periods of FT sampling.

For the biomass burning periods, approximately 30% of the leading-edge fits failed due to the time dependent scattering signal being above 5% of the maximum laser intensity at a time of zero. Another 5% of the particles were rejected from the coating analysis because the leading edge fit gave a result that was above the scattering detector saturation limit and therefore outside the calibration range. This means that the coating thicknesses were determined for only 65% of the rBC

particles detected.

For the FT sampling periods, only 6% of the leading-edge fits failed due to the time dependent scattering signal exceeding 5% of maximum laser intensity at a time of zero. Another 3% failed when the leading edge fit gave a result above the scattering detector saturation limit. In this case the mixing state analysis was done for 91% of the particles detected.

6.2.4 Total aerosol measurements

In order to identify periods of biomass burning, an Aerodyne aerosol chemical speciation Monitor (ACSM) (Ng et al., 2011) was used for chemical speciation of the total aerosol during the measurements in 2009 and 2012. The ACSM is part of the regular suite of instruments operating at the WHI site (Takahama et al., 2011) and is similar to the Aerodyne Aerosol Mass Spectrometer (Jayne et al., 2000), with the main differences being that it does not measure particle size and it has reduced sensitivity.

In 2010 the ACSM was offline and total aerosol speciation was performed with a C-mode time-of-flight aerosol mass spectrometer (C-ToF-AMS, Aerodyne Research). The C-ToF-AMS measures aerodynamic diameter and provides higher mass resolution and increased sensitivity relative to the ACSM.

6.2.5 Back trajectories

Air mass back-trajectories were calculated using the NOAA HYSPLIT model (Draxler and Rolph, 2012; Rolph, 2012) with the GDAS 1-degree meteorologi-

cal dataset. This has a 3-hour time resolution, a 1-degree horizontal resolution, and 23 vertical layers. The back trajectories were calculated at the elevation of Whistler peak (2182 m a.m.s.l.) as well as at 200 m below the peak to account for uncertainties in the initial conditions.

6.3 Results and Discussion

6.3.1 Size distributions

The range of rBC diameters measured in this study was 76-220 nm VED. It is possible, however, to estimate what portion of the rBC mass is not being measured. If we assume that the mass distribution of rBC containing particles is lognormal with a single mode we can fit the distributions measured by the SP2 and estimate what portion of the actual mass distribution is outside of our measurement range. This was done for two subsets of the full rBC record at WHI: all particles from biomass burning periods, and all particles from FT periods (Figure 6.1). The fraction of the distribution being sampled was 55% and 60% for biomass burning and FT periods respectively. All mass concentrations reported here have been scaled by a factor of 1.8 to account for the fraction of mass not sampled.

In Figure 6.1 the red trace shows the mass distribution for all rBC containing particles collected during periods of biomass burning. The full distribution (from the fit) has a mass median diameter of 218 nm and σ_g of 1.6 (Table 6.1). This is in reasonable agreement with other SP2 measurements of biomass burning particles. Kondo et al. (2011) observed a mass mean diameter of 207$\pm$31 nm for biomass

burning plumes of Asian origin measured over Alaska and a mass mean diameter of 187±10 nm for biomass burning plumes a few hours old measured over northern Canada. Sahu et al. (2012) measured a mass mean diameter of 193±16 nm for fresh biomass burning plumes in California and Schwarz et al. (2008a) measured a mass mean diameter of 210 nm for fresh biomass burning plumes over Texas.

The mass distribution for periods of FT sampling is also shown in Figure 6.1 (blue trace). The full distribution (from the fit) has a mass median diameter of 185 nm and a σ_g of 1.7 (Table 6.1). Liu et al. (2010b) measured a geometric mean diameter of 220-240 nm for FT rBC particles sampled at the Jungfraujoch station in late winter. They noted that the diameters measured during periods of FT sampling did not differ significantly between periods of FT and non-FT sampling. In addition, Metcalf et al. (2012) found a mass median diameter of 161±41 nm from rBC measurements made in the FT over Los Angeles, CA.

6.3.2 Refractory black carbon measurements at WHI

rBC mass concentrations measured at WHI, binned into 10 minute intervals, is shown in Figure 6.2. Data are available for June-August of 2009; June-July of 2010; and April-May of 2012. Figure 6.3, panel A, shows a histogram of rBC mass concentrations for the full measurement record. Over the full measurement period, the median rBC concentration was aproximately 15 ng m^{-3} with 10^{th} and 90^{th} percentile values of about 2 and 42 ng m^{-3} respectively (Table 6.1).

6.3.3 Identifying periods of biomass burning sampling

Periods where the sampled particulate matter was influenced by biomass burning are indicated by the shaded regions in Figure 6.2 and highlighted by the boxed region in Figure 6.4. These were isolated from the general dataset using a procedure based on that of Takahama et al. (2011). First, non-anthropogenic sources were separated from anthropogenic sources using the ratio of organic material (OM) to organic material plus sulfate aerosol (OM+SO_4), as measured by the ACSM or C-ToF-AMS. Periods dominated by non-anthropogenic aerosols are characterized by an OM/(OM+SO_4) ratio of greater than 70%. Second, periods of biomass burning were then separated from biogenic sources by the increased concentration ($> 5\sigma_{std}$ of back ground concentrations) of levoclucosan fragments in the ACSM or C-ToF-AMS signal at m/z 57, 60, and 73 (see Figure 6.4 and Figure 6.5). Levoglucosan is a commonly used tracer for biomass burning aerosols (Simoneit et al., 1999; Takahama et al., 2011). Third, to ensure there were forest fires within the area, the number of forest fires reported by the CWFIS within 200 km of WHI was also taken into account.

6.3.3.1 Refractory black carbon mass concentrations during periods of biomass burning

Periods where the sampled particulate matter was produced by biomass burning are indicated by the shaded region in Figure 6.2. Higher rBC mass concentrations were observed during biomass burning events than during any other period. Figure 6.3 panel B shows a histogram of rBC mass concentrations for all periods of

biomass burning influence. These periods had a mean concentration of approximately 124 ng m^{-3} and a median concentration of about 94 ng m^{-3} with 10^{th} and 90^{th} percentile values of about 41 and 234 ng m^{-3} respectively (Table 6.1).

6.3.3.2 Refractory black carbon coating thicknesses during periods of biomass burning

Figure 6.5 panel A shows a 2D histogram of coating thickness as a function of rBC core diameter for all rBC containing particles measured during the biomass burning period that occurred from July 26-28, 2010. A scattering calibration was not done for the 2009 data, so coating thicknesses could not be determined for the 2009 biomass burning period.

The SP2 scattering detectors limit the range for which coating thicknesses can be measured. Small bare, or thinly coated, particles are below the threshold for detection of scattered light, while large rBC particles with thick coatings are above the saturation limit of the instrument. These limits are evident in Figure 6.5 panel A, where the data are cut off in the lower left and upper right areas of the plot. We‘ve set the lower limits in Figure 6.5 panel A at $2\sigma_{std}$ above the minimum detectable scattering signal of the instrument to avoid the random uncertainty in the scattering from any given particle resulting in a calculated scattering amplitude below our detection limits.

A frequency distribution of coating thicknesses for rBC core particles with diameters between 140-160 nm VED (see Section 6.2.3) measured during the period of biomass burning is shown in Figure 6.5 panel B. The average coating thickness during this period was 55 nm with 10^{th} and 90^{th} percentile values of 3

and 100 nm respectively. This average coating thickness was within the range of coating thickness observed by others. For example, Laborde et al. (2013) found an average coating thickness of biomass burning influenced rBC in Paris of 15 nm for 200 nm rBC core VED, and Schwarz et al. (2008a) observed an average coating thickness of 65 nm for rBC core VED between 190 and 210 nm.

6.3.4 Identifying periods of free tropospheric sampling

Macdonald and colleagues considered a number of strategies for determining when WHI is in the FT (Macdonald et al., 2011). They examined diurnal cycles in ozone, CO, and water vapor as well as measurements of atmospheric stability in the air mass extending from the bottom of Whistler valley up to the peak. In all cases the data showed that in the nighttime (20:00 to 08:00 PST) Whistler Peak is almost entirely free of boundary layer influences, a conclusion that is supported by more detailed meteorological analysis of the area (Gallagher et al., 2011), and by approaches employed for other mountain-top sites (Andrews et al., 2011).

Following their work, we have restricted our analysis for the FT to the 2012 April-May nighttime data (20:00-08:00 PST) as a conservative approach to eliminating boundary layer influences. As a further measure to eliminate possible local or regional influences we have combined this seasonal and time-of-day approach with analysis of air mass back trajectories generated with HYSPLIT (see Section 6.2.5). Ten day back trajectories were calculated for every hour from 20:00 to 08:00 PST and analyzed so that air masses could be classified as non-FT or FT. In order to qualify as a FT air mass, free of valley influence, the back trajectory

had to show the air mass having spent less than 12 of its final 48 hours at pressures above 900hPa (about 1km in altitude) (Macdonald et al., 2011). Once this condition was met, the SP2 data collected from 30 minutes prior until 30 minutes after that air masses arrival time was classified as FT.

6.3.4.1 Refractory black carbon mass concentrations in the free troposphere

Figure 6.3, panel C, shows a histogram of measured rBC mass concentrations for periods when Whistler was determined to be in the FT. These periods had a mean rBC mass concentration of about 14 ng m^{-3}, and a median rBC mass concentration of about 11 ng m^{-3} with 10^{th} and 90^{th} percentile values of around 1 and 46 ng m^{-3} respectively (Table 6.1).

Table 6.2 summarizes the rBC mass concentrations measured for the FT in this study, and also gives values for some comparable measurements made at other locations. The Jungfraujoch high elevation site in Switzerland is located at 3580 m a.m.s.l and like WHI, it is well removed from significant pollution sources (Cozic et al., 2007). Free troposphere rBC concentrations measured in late winter at Jungfraujoch are similar to those measured in April and May of 2012 at WHI. They are slightly lower than WHI for general FT periods (median values of about 11 ng m^{-3} for WHI and about 8 ng m^{-3} for Jungfraujoch) and drop lower for periods when the Jungfraujoch station is influenced by precipitation (median value of around 3 ng m^{-3} for Jungfraujoch) (Liu et al., 2010b). rBC mass concentrations measured in the FT over the US northwest coast during INTEX-B (average of 90 ng m^{-3}) are considerably higher than those measured in this study. In the HIPPO

campaigns, rBC mass concentrations in the central Pacific from 20°N-60°N (0-10 km altitude) ranged from 0.1 to 40 ng m^{-3} depending on season and altitude.

6.3.4.2 Refractory black carbon coating thicknesses in the free troposphere

Figure 6.5 panel C shows a 2D histogram of coating thickness as a function of rBC core diameter for all rBC containing particles measured during the FT sampling periods in April-May of 2012. As in Figure 6.5 panel A, we‘ve set the lower limits in Figure 6.5 panel C at $+2\sigma_{std}$ of the minimum detectable scattering signal of the instrument.

From the coating thickness frequency distribution of rBC particles with core $VEDs$ in the 140-160 nm range (see Figure 6.5 panel C), the average coating thickness was 32 nm with 10^{th} and 90^{th} percentile values of 4 and 60 nm respectively. A study that reports on the rBC coating thicknesses measured in the FT was a study conducted by Metcalf et al. (2012). This study measured the coating thicknesses of rBC particles in the FT near the Los Angeles basin, and found that the mean coating thickness over LA was 188 ± 31 nm for all rBC core diameters between 80-227 nm VED.

6.4 Summary and Conclusions

A 3 year period of rBC measurements from a high elevation mountain site at Whistler, BC were investigated with a SP2. From the full 3 year rBC record, two subsets of data were identified; 1) periods that were influenced by biomass burning and 2) periods of free tropospheric sampling. Air masses that were influenced

by biomass burning were identified by using measurements of aerosol chemical speciation, while free tropospheric periods were identified by using a seasonal and time-of-day approach. Each subset of data was analyzed to investigate the size distributions, mass concentrations, and coating thicknesses of rBC containing particles.

Fitting lognormal functions to the rBC core mass size distributions resulted in median mass diameters of 208 nm for periods of biomass burning influence, a median mass diameter that was consistent with other measurements made of biomass burning influenced rBC. The median mass diameter found for periods of free tropospheric sampling was 192 nm. The mass size distributions during both periods of sampling show a similar spread in the distribution, where the width parameter σ_g was found to be 1.6 and 1.7 for biomass burning and free tropospheric sampling periods respectively.

The median mass concentration found for periods of free tropospheric sampling was appoximately 11 ng m^{-3}, which was significantly lower than free tropospheric air measured in the northwestern part of the US. However, the median mass concentrations measured at the remote high elevation site at Whistler agreed to within 75% of mass concentrations measured at another remote mountain high elevation site (Jungfraujoch).

Coating thicknesses of rBC containing particles during the two subsets of data were investigated, and frequency distributions of coating thickness were investigated for rBC particles with core diameters between 140 and 160 nm. The coating frequency distribution for the biomass burning period had a median coating

thickness of about 55 nm and was quite broad in shape where the 10^{th} and 90^{th} percentiles were 5 and 106 nm respectively. The coating thickness frequency distribution during free tropospheric sampling had a median thickness of nearly half that found for the biomass burning period, at approximately 32 nm, and was much narrower in shape with 10^{th} and 90^{th} percentiles of 6 and 63 nm respectively.

The results found from this study contribute to the body of evidence for measurements of refractory black carbon at remote mountain sites and under different sampling conditions. Adding to this body of evidence aids in increasing our understand of how black carbon properties (e.g. size distributions, mass concentrations, and coating thicknesses) vary as a result of location as well as the type of air mass. Increasing our understanding of these rBC properties can then be used to further constrain computer models that are used to predict how rBC can affect climate. For example, Wang et al. (2014) used atmospheric BC data collected over the ocean and in the free troposphere to constrain the application of a commonly used global climate model (GEOS-Chem) coupled to a radiative transfer model to infer a direct radiative forcing of BC to be 0.19 W m^{-2}, with an uncertainty range of 0.17-0.31 W m^{-2}. They found that this large range of uncertainty was primarily a result of the uncertainty in BC distribution in the atmosphere. Furthermore, the constrained estimate of 0.19 W m^{-2} they computed was lower (by as much as 21%) than results of other modeled estimates reported in the literature, which was primarily driven by BC concentrations over the oceans and in the free troposphere. Data from the study presented in this chapter could also be applied in a similar manner as was done in Wang et al. (2014) to constrain direct radiative

forcing estimates at similar locations as Mt. Whistler.

6.5 Chapter 6 Figures and Tables

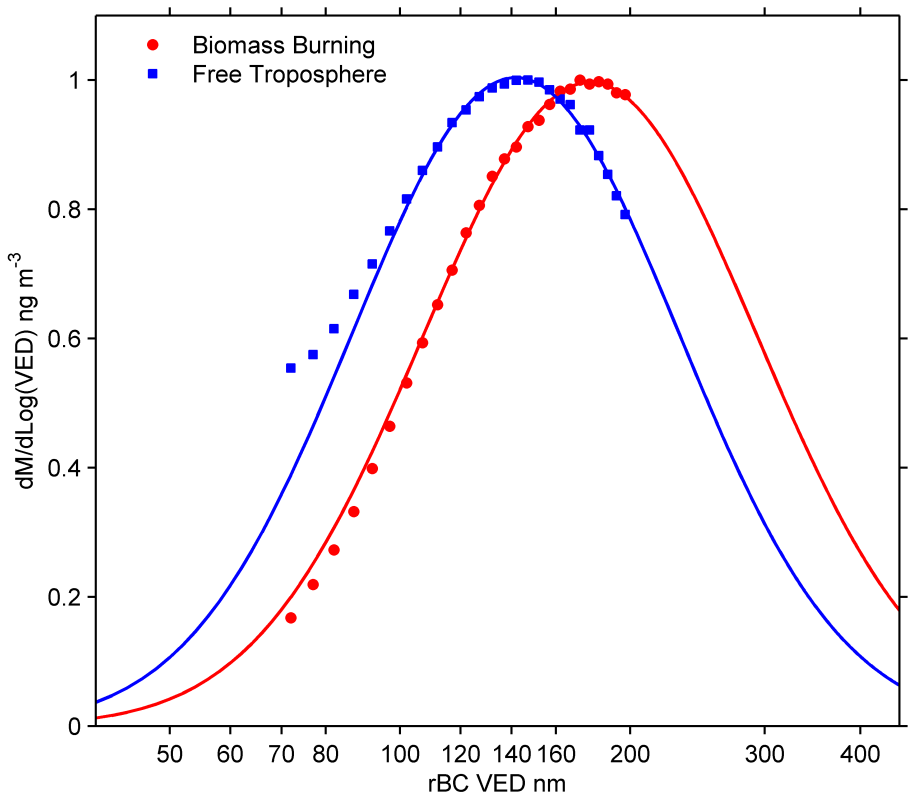

Figure 6.1: Normalized mass distributions for periods of free troposphere sampling and biomass burning. Lines are single lognormal fits.

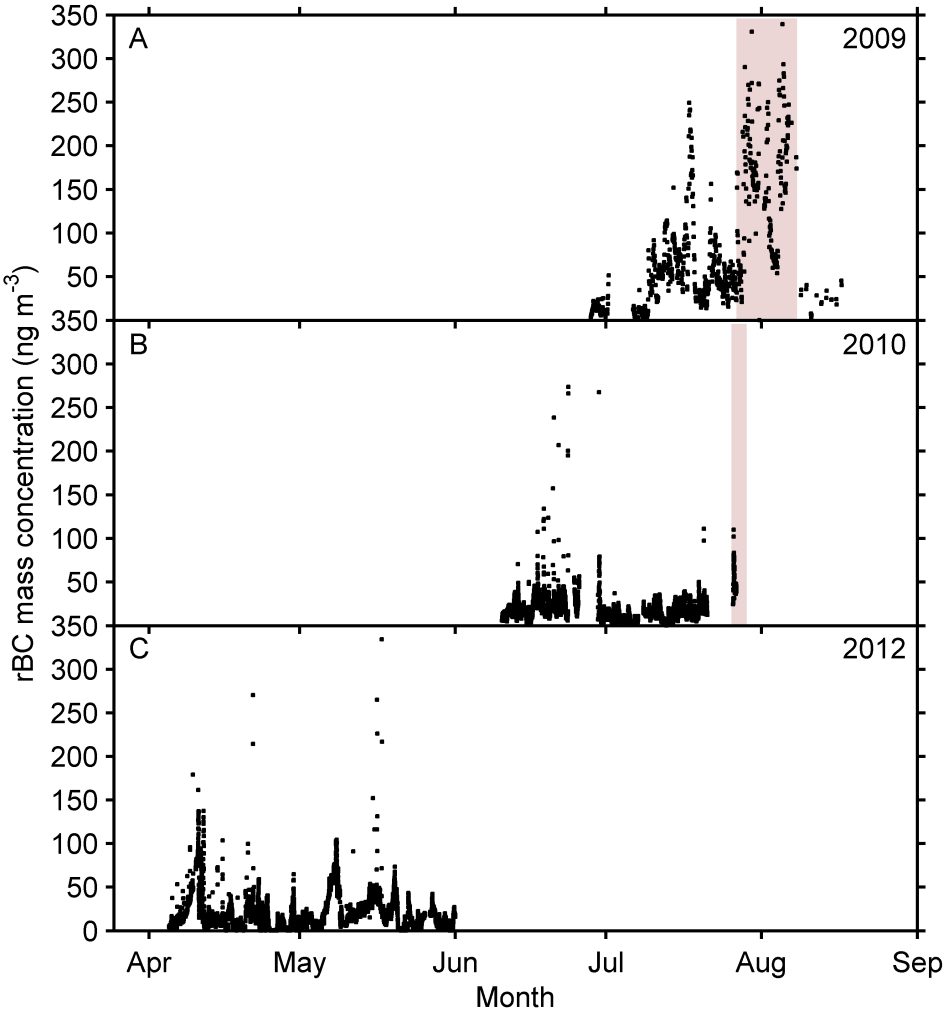

Figure 6.2: Measured rBC mass concentrations for 2009, 2010, and 2012 with periods of biomass burning marked by red shaded areas.

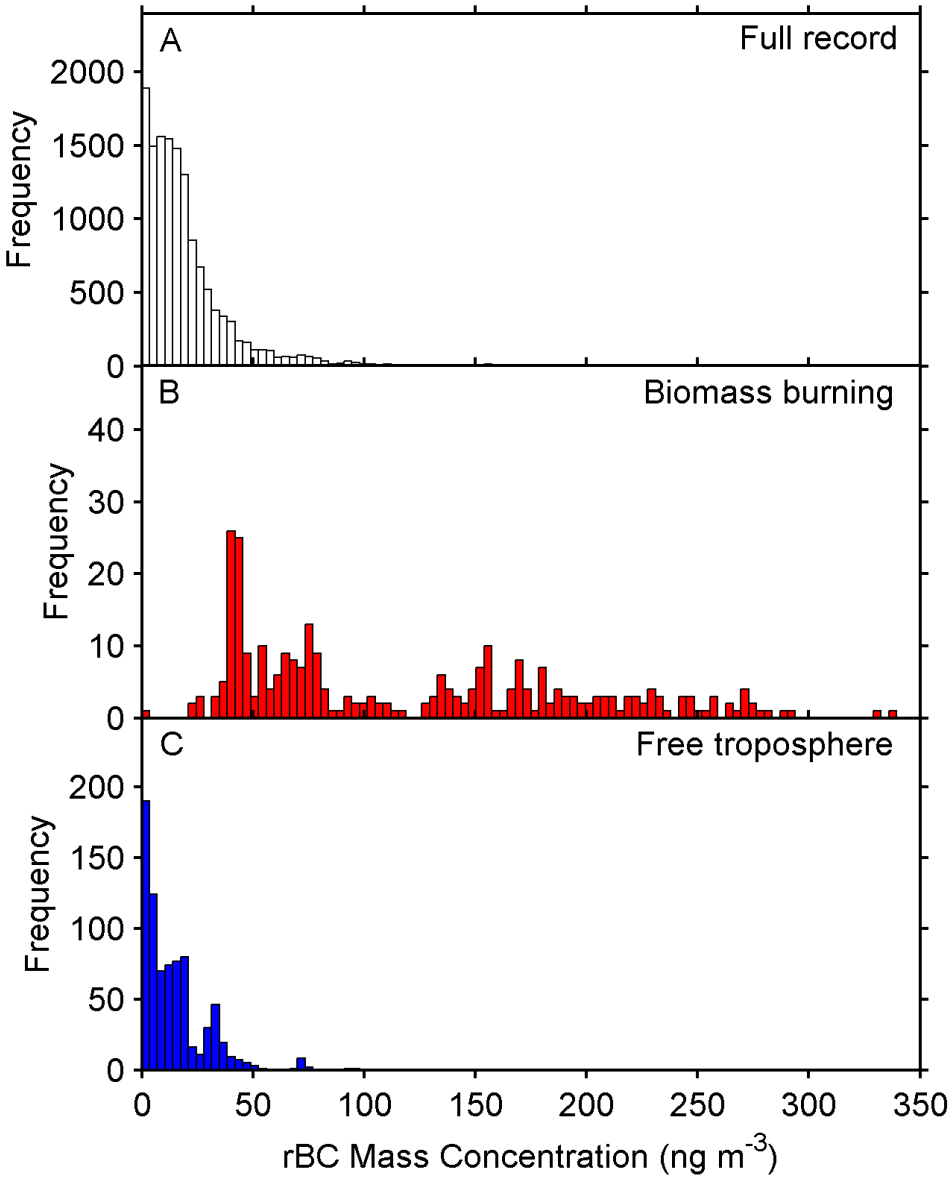

Figure 6.3: Histograms of measured rBC mass concentration at WHI for the full record (panel A), periods of biomass burning (panel B), and periods of free troposphere sampling (panel C). All concentrations are 10 minute averages.

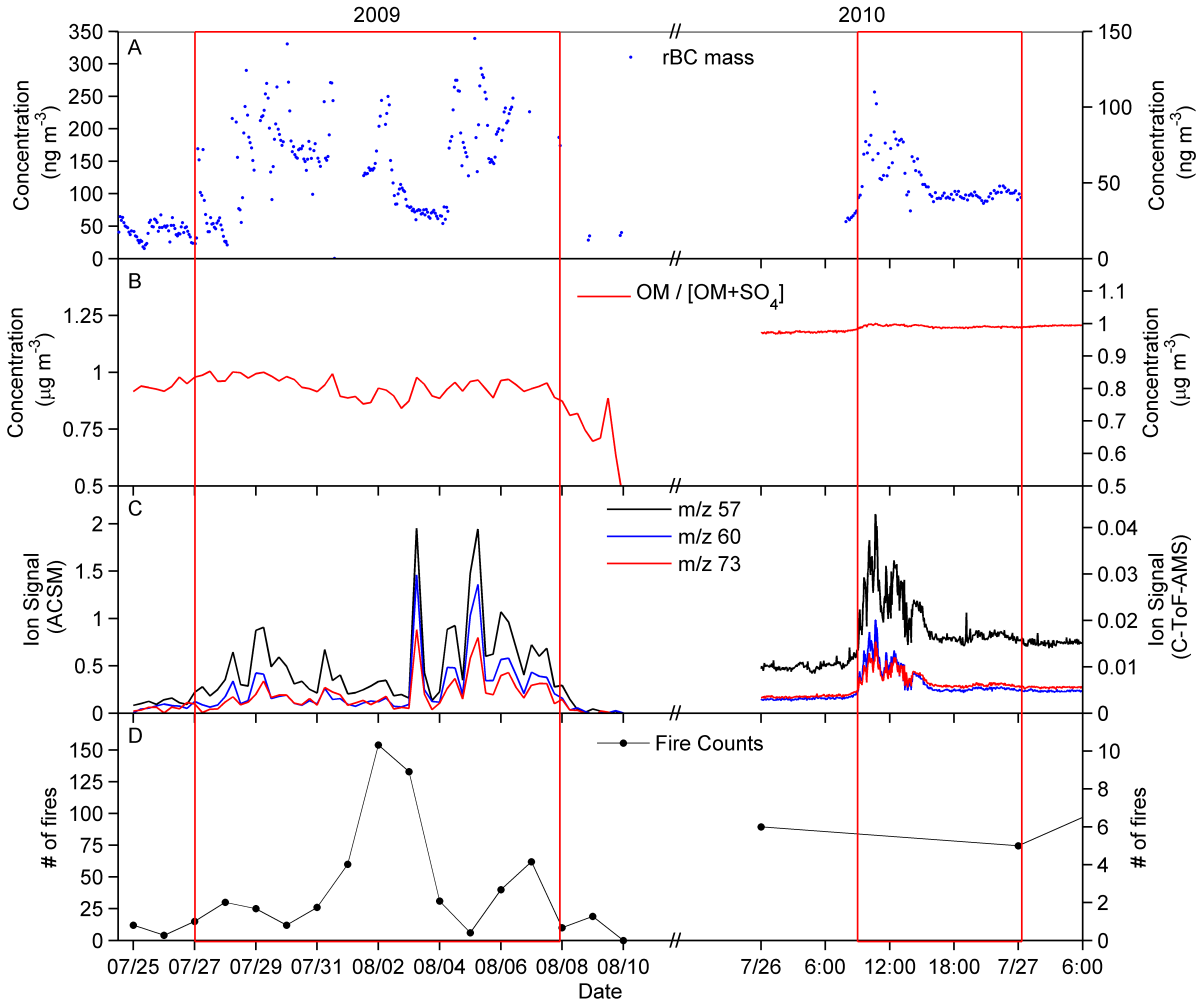

Figure 6.4: Identification of biomass burning periods in 2009 (left side) and 2010 (right side). Panel A Shows rBC mass concentration as measured by the SP2 (binned into 10 minute intervals); panel B shows the ratio of organic material (OM) to OM plus sulfate (SO_4), where a ratio of > 0.7 is considered to be from non-anthropogenic sources; panel C shows the raw ion signals of the levoglucosan fragments at m/z 57, 60, and 73 as measured by the ACSM in 2009 and the C-ToF-AMS in 2010. Ion signals that were greater than $5\sigma_{std}$ were considered to be influenced by biomass burning. Panel D shows the number of fires reported by day within 200 km of Whistler Mountain (CWFIS). The red boxes indicate the portion of the data included from biomass burning.

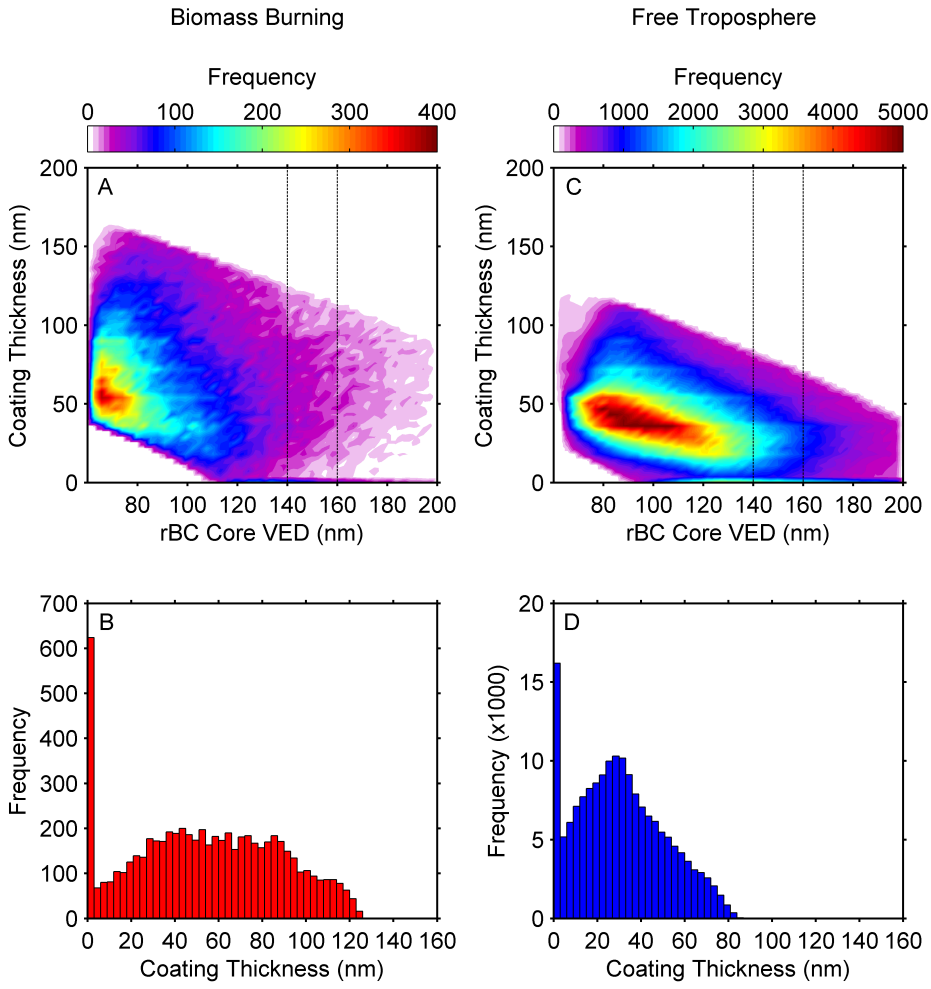

Figure 6.5: 2D histograms of coating thicknesses and core diameters for all rBC containing particles measured during the biomass burning period from July 26-28, 2010 (panel A), and the period of free troposphere sampling in April-May 2012 (panel C). Only particles with detectable scattering signals are shown in panels A and C. Coating thickness frequency distributions for rBC cores with VED from 140-160 nm (represented on panels A and C as black dashed lines) are shown in panel B for biomass burning periods, and panel D for free troposphere periods.

Table 6.1: Summary of basic statistics for rBC mass concentrations and mass distributions measured at WHI for the full record period, periods of biomass burning (BB), and periods of free troposphere sampling (FT).

	10^{th} Percentile [Mass] ng m^{-3}	50^{th} Percentile [Mass] ng m^{-3}	90^{th} Percentile [Mass] ng m^{-3}	Mean [Mass] ng m^{-3}	MMD[a] (σ_g) nm
Full record	2.31	14.99	43.05	23.20	-
BB periods	40.92	94.03	234.09	123.91	218 (1.6)
FT periods	1.05	10.57	32.63	14.16	185 (1.7)

[a]Mass median diameter

Table 6.2: Comparison of rBC mass concentrations measured in the free troposphere from this study and several other locations.

Dataset	10^{th} Percentile [Mass] ng m^{-3}	50^{th} Percentile [Mass] ng m^{-3}	90^{th} Percentile [Mass] ng m^{-3}	Mean [Mass] ng m^{-3}	Reference
WHI FT	1.05	10.57	32.63	14.16	This work
Jungfraujoch FT	0.62	8.11	27.44	13.24	Liu et al. (2010b)
Jungfraujoch FT[a]	0.45	2.68	14.31	6.23	Liu et al. (2010b)
Northwest Coast (USA) FT	-	-	-	90	Dunlea et al. (2009)
Central Pacific[b]	-	0.1-40	-	-	Wang et al. (2014)

[a] Influenced by precipitation

[b] Results are from 20°N to 60°N, 0-10 km, and depend on the season.

Chapter 7

Conclusions

7.1 Activation of Refractory Black Carbon into Liquid Water Cloud Droplets

Refractory black carbon in liquid water cloud residuals was measured during cloud events at a marine boundary layer site in La Jolla, CA, and at the top of Whistler Mountain in Whistler, BC.

In Chapter 4 two liquid water clouds were sampled at La Jolla, CA, and based on the calculated back trajectories, bulk aerosol number concentrations, and rBC mass concentrations, the air masses were classified as polluted marine air. Number size distributions were determined for both clouds, and it was found that the size distributions of both the bulk aerosol and rBC measured in cloud residuals displayed a shift towards larger diameters when compared to the respective measurements made from the total inlet. The number size distributions of rBC resid-

uals also showed that rBC particles with small ($<$ 100 nm) core diameters can be incorporated into cloud droplets and therefore contribute to the CCN population. The coating analysis of the SP2 data showed that the smaller rBC cores that were activated into cloud droplets had thick coatings, with average coating thicknesses of $\approx$75 nm at core diameters between 70-80 nm compared to $\approx$29 nm coatings for core diameters between 200-210 nm. These results suggest that for larger diameter rBC particles only a modest coating ($\approx$ 25 nm) of hygroscopic material is needed to become CCN active at relatively low critical supersaturations (0.05%). Furthermore, incorporating the coating into the rBC size distributions resulted in greater similarities with the size distributions of the residual bulk aerosol measured at the marine boundary layer site.

Size-resolved activated fractions of rBC were determined and compared to size-resolved activated fractions of the bulk aerosol, and it was found that during both clouds sampled, the activated fractions for rBC cores were larger than the activated fractions for the bulk aerosol at diameters $<\approx$150 nm. These results were explained by the presence of thick coatings surrounding the smaller rBC cores. In addition, the activated fractions of rBC particles with core diameters $<$ 100 nm were significant, where the activated fractions of the smallest diameters measured (70-80 nm), were found to be 0.01 and 0.05 for Cloud 2 and Cloud 3 respectively. Since the fraction of droplets sampled by the CVI was $<$100%, the calculated activated fractions found during this study should be considered lower limits to the total fractions activated.

The presence of rBC core particles with diameters $<$ 100 nm seen in the obser-

vations made at La Jolla were quantitatively validated using kappa-Köhler theory. Based on the bulk aerosol chemical compositions and estimations of the critical activation diameters of the bulk aerosol, the cloud critical supersaturations were found to be approximately 0.05% during the two clouds sampled in this study. Using the estimated critical supersaturation of the clouds sampled and applying kappa-Köhler theory to rBC particles with different coating thickness showed that the critical diameter for activation of rBC cores was $<$50 nm for all cores with coating thicknesses $\geq$100 nm. This quantitative prediction using kappa-Köhler theory was consistent with the observations of rBC cores with diameters $<$ 100 nm being activated into the sampled cloud droplets, if the measured coating thicknesses are factored in.

Measurements of rBC in liquid water cloud droplets were also measured during two clouds at the peak of Whistler Mountain and presented in Chapter 5. Back trajectory analysis showed that neither of the two clouds sampled had traveled near, or over any highly populated regions within 24 hours prior to being sampled. Combining calculated back trajectories with forest fire locations, reported or detected by satellite, indicated that the first cloud sampled had no influence from biomass burning aerosols. However, it was concluded that the second cloud sampled most likely had some influence by biomass burning aerosols since there were several forest fires located in the vicinity of the back trajectories. High levels of the biomass burning marker, acetonitrile, further confirmed this conclusion.

The number size distributions of the residual bulk aerosol measured at Whistler Mountain showed that the majority of the activated aerosol came from the larger

diameter mode of the total bulk aerosol. However, unlike the residual rBC measured in La Jolla, the maximum of the residual rBC measured at Whistler Mountain was below the detection limit (≈70 nm) of the SP2. By assuming the rBC residual distribution is lognormal, the mean diameter would therefore be < 70 nm. This result is consistent with the observations of smaller rBC core diameter particles being activated into liquid water droplets at Whistler Mountain.

The average rBC mass fractions activated during the two clouds sampled at Whistler were found to be 0.24 and 0.19 for Clouds 1 and 2 respectively. These average rBC mass fractions activated were lower than those values reported at other remote mountain sites. The differences may have been due to the fact that less than 100% of the droplet number distributions were sampled during the Whistler study and therefore, the rBC mass fractions activated were likely lower limits.

Finally, the size-resolved activated fractions of both the bulk aerosol and rBC observed at Whistler also showed a size dependence for the two clouds sampled at this remote mountain site. The activated fractions of rBC ranged from approximately 0.2 at the smallest size bin (70 to 80 nm) to 0.6 at the largest size bin (200 to 210 nm). Since the fraction of droplets sampled by the CVI during this study was also less than 100%, the calculated activated fractions measured here, should also be considered lower limits to the total fractions activated. The results from the size-resolved activated fractions calculated from Whistler also showed that smaller diameter ($\approx$ 70 nm) rBC cores were significantly incorporated into the droplets measured at this site. Since 70 nm uncoated cores are only expected to be activated at relatively high cloud supersaturations (≈0.5%, see Figure 4.10),

it is likely that the rBC cores were coated with soluble material. In addition, during the first cloud sampled the rBC activated more efficiently than the bulk aerosol over all sizes measured, which strongly suggests the presence of hydrophilic coatings surrounded the rBC cores making the overall particle diameter larger and therefore more easily activated.

7.2 Refractory Black Carbon Properties During Biomass Burning and Free Troposphere Sampling

In Chapter 6, rBC measurements from the summer of 2009 and 2010 as well as the spring of 2012 at a high elevation mountain site at Whistler were presented. From the three sampling periods, two subsets of data were identified: 1) periods that were influenced by biomass burning and 2) periods of free tropospheric sampling. Each subset of data was analyzed to investigate the size distributions, mass concentrations, and coating thicknesses of rBC containing particles.

Fitting of the mass size distributions resulted in median mass diameters of 208 nm for periods of biomass burning influence, and 192 nm for periods of free troposphere sampling. Both of these mass median diameters measured at the WHI site were consistent with previously reported values. Median mass concentrations were also investigated and found to be approximately 94 ng m^{-3} during periods of biomass burning influence, and 11 ng m^{-3} during free troposphere sampling (scaled by a factor of 1.72 for STP). The free tropospheric rBC mass concentrations measured at WHI were significantly lower than similar measurements in the

northwestern part of the US, but agreed to within 65% of mass concentrations measured at the remote mountain high elevation site on top of the Jungfraujoch.

Based on the histograms of rBC coating thicknesses for rBC particles with core diameters between 140-160 nm the average coating thickness during periods of biomass burning (55 nm) was nearly two times thicker than the average coating thickness measured during periods of free troposphere sampling (32 nm). A comparison of the average coating thickness for all rBC core particles with diameters from 80-200 nm measured at WHI with another study that measured coated rBC particles in the free troposphere over the Los Angeles basin showed that the rBC measured in the free troposphere at WHI had significantly thinner coatings.

Figure 5 shown in Bond et al. (2013) shows the modelled S_C of BC from both diesel and gasoline exhaust as a function of both particle diameter and BC mass fraction. In general this figure shows that the overall particle diameter has a greater effect on activation than the mass fraction of BC present in a mixed particle, at a constant S_C. More specifically, Figure 5 shows, at a constant S_C of $\approx$0.05% the increase in mass fraction of BC is negligible for particle diameters greater than approximately 200 nm. Although the source of rBC measured during the studies presented in both Chapters 4 and 5 are most likely not pure engine exhaust, the results presented in these chapters are consistent with the results of the model shown in Figure 5 of Bond et al. (2013). The results presented in Chapter 4 are consistent with these results as even for the smallest core diameters measured at the marine boundary layer site the overall particle diameters were larger than 200 nm, on average, when the coating thickness were taken into account. Figure 5

further shows that for small diameter BC (≈70-100 nm) at 70% BC mass fractions would require very large (>1%) S_C are required. Therefore, the conclusion in Chapter 5 that the rBC cores activated at the high elevation mountain site had large coatings surrounding the cores is supported by Figure 5 in Bond et al. (2013) since the supersaturations experienced at Whistler were likely much lower than 1%.

7.3 Considerations for Future Work

Based on the high degree of uncertainty (≈ 90%) associated with current best-estimates on the radiative forcing of BC due to indirect effects, it is clear that more studies similar to the ones presented in Chapters 4 and 5 are needed to evaluate and constrain model simulations. Although the research presented in these chapters does add to the body of knowledge on the properties of BC that drive CCN activation, there were some limitations to the conclusions that could be drawn. Since only larger (> ≈ 10-11 μm) droplets were investigated during these studies, the question remains of whether BC particles are activated into smaller droplets in a similar manner to larger droplets. Future field studies with a CVI that is optimized to sample smaller droplets would help to answer this question.

Chapters 4 and 5 also showed that smaller (< ≈ 100 nm) rBC particles can act as CCN when large hygroscopic coatings are present. A number of studies (e.g., Metcalf et al., 2012; Rose et al., 2006; Schwarz et al., 2008a) have shown that a significant fraction of the atmospheric BC number distributions are from smaller (< ≈ 100 nm) diameter particles and, if coated, these particle may substantially influence the CCN population. In the quantitative coating analysis presented in

Chapter 4, an assumption was made that the composition of the coating was identical to that of the bulk aerosol for all rBC core diameters. It would be worthwhile to investigate the chemical compositions of coatings on activated BC particles to test if this assumption is valid over all BC diameters. Such an investigation could also increase our knowledge of what properties drive the CCN ability of atmospheric BC. Furthermore, because such large uncertainties are associated with model estimates of the contribution of BC to the indirect effects on climate exist, it would be informative to design a field study that measures the exact components needed by a specific model to simulate a cloud event. This type of study would allow for direct comparison of ambient observations with model simulation, which could provide useful information on necessary model constraints and direction for future ambient studies. It would also be informative to conduct similar studies discussed in Chapters 4 and 5 at other sites and for different cloud types to better understand the global role that clouds play in processing rBC.

Bibliography

L. Ahlm, K. M. Shakya, L. M. Russell, J. C. Schroder, J. P. S. Wong, S. J. Sjostedt, K. L. Hayden, J. Liggio, J. J. B. Wentzell, H. A. Wiebe, C. Mihele, W. R. Leaitch, and A. M. Macdonald. Temperature-dependent accumulation mode particle and cloud nuclei concentrations from biogenic sources during WACS 2010. *Atmos. Chem. Phys.*, 13(6):3393–3407, Mar. 2013. doi:10.5194/acp-13-3393-2013. URL http://www.atmos-chem-phys.net/13/3393/2013/http://www.atmos-chem-phys.net/13/3393/2013/acp-13-3393-2013.pdf. → pages 78

J. D. Allan, A. E. Delia, H. Coe, K. N. Bower, M. Alfarra, J. L. Jimenez, A. M. Middlebrook, F. Drewnick, T. B. Onasch, M. R. Canagaratna, J. T. Jayne, and D. R. Worsnop. A generalised method for the extraction of chemically resolved mass spectra from Aerodyne aerosol mass spectrometer data. *Journal of Aerosol Science*, 35(7):909–922, July 2004. doi:10.1016/j.jaerosci.2004.02.007. → pages 47

T. L. Anderson, R. J. Charlson, and D. S. Covert. Calibration of a Counterflow Virtual Impactor at Aerodynamic Diameters from 1 to 15 m. *Aerosol Science and Technology*, 19(3):317–329, 1993. → pages 41, 42

M. Andreae. Correlation between cloud condensation nuclei concentration and aerosol optical thickness in remote and polluted regions. *Atmospheric Chemistry and Physics*, 9(2):543–556, 2009. → pages 51

M. Andreae and D. Rosenfeld. Aerosol cloud precipitation interactions. Part 1. The nature and sources of cloud-active aerosols. *Earth-Science Reviews*, 89 (1-2):13–41, July 2008. doi:10.1016/j.earscirev.2008.03.001. → pages 59, 89

E. Andrews, J. A. Ogren, P. Bonasoni, A. Marinoni, E. Cuevas, S. Rodríguez,

J. Y. Sun, D. A. Jaffe, E. V. Fischer, U. Baltensperger, E. Weingartner, M. C. Coen, S. Sharma, A. M. Macdonald, W. R. Leaitch, N.-H. Lin, P. Laj, T. Arsov, I. Kalapov, A. Jefferson, and P. Sheridan. Climatology of aerosol radiative properties in the free troposphere. *Atmospheric Research*, 102(4): 365–393, 2011. doi:10.1016/j.atmosres.2011.08.017. → pages 109

T. S. Bates, P. K. Quinn, D. S. Covert, D. J. Coffman, J. E. Johnson, and A. Wiedensohler. Aerosol physical properties and processes in the lower marine boundary layer: a comparison of shipboard sub-micron data from ACE-1 and ACE-2. *Tellus B*, 52B:258–272, 2000. → pages 51

T. S. Bates, Coffman D. J., D. S. Covert, and P. K. Quinn. Regional marine boundary layer aerosol size distributions in the Indian, Atlantic, and Pacific Oceans: A comparison of INDOEX measurements with ACE-1, ACE-2, and Aerosols99. *Journal of Geophysical Research*, 107(D19):8026, 2002. doi:10.1029/2001JD001174. → pages 39

T. C. Bond and R. W. Bergstrom. Light Absorption by Carbonaceous Particles: An Investigative Review. *Aerosol Science and Technology*, 40(1):27–67, Jan. 2006. doi:10.1080/02786820500421521. → pages 24, 29, 44

T. C. Bond, D. G. Streets, K. F. Yarber, S. M. Nelson, J. H. Woo, and Z. Klimont. A technology-based global inventory of black and organic carbon emissions from combustion. *Journal of Geophysical Research*, 109(D14203):1–43, 2004. doi:10.1029/2003JD003697. → pages 5

T. C. Bond, S. J. Doherty, D. W. Fahey, P. M. Forster, T. Berntsen, B. J. DeAngelo, M. G. Flanner, S. Ghan, B. Kärcher, D. Koch, S. Kinne, Y. Kondo, P. K. Quinn, M. C. Sarofim, M. G. Schultz, M. Schulz, C. Venkataraman, H. Zhang, S. Zhang, N. Bellouin, S. K. Guttikunda, P. K. Hopke, M. Z. Jacobson, J. W. Kaiser, Z. Klimont, U. Lohmann, J. P. Schwarz, D. Shindell, T. Storelvmo, S. G. Warren, and C. S. Zender. Bounding the role of black carbon in the climate system: A scientific assessment. *Journal of Geophysical Research: Atmospheres*, 118(11):5380–5552, June 2013. doi:10.1002/jgrd.50171. → pages xvi, 4, 5, 8, 9, 12, 35, 36, 127, 128

R. Y.-W. Chang, J. G. Slowik, N. C. Shantz, A. Vlasenko, J. Liggio, S. J. Sjostedt, W. R. Leaitch, and J. P. D. Abbatt. The hygroscopicity parameter (κ) of ambient organic aerosol at a field site subject to biogenic and anthropogenic influences: relationship to degree of aerosol oxidation. *Atmospheric Chemistry*

and Physics, 10(11):5047–5064, June 2010. doi:10.5194/acp-10-5047-2010. → pages 16, 60

W. Chen, Y. H. Lee, P. J. Adams, A. Nenes, and J. H. Seinfeld. Will black carbon mitigation dampen aerosol indirect forcing? *Geophysical Research Letters*, 37 (L09801):1–5, May 2010. doi:10.1029/2010GL042886. → pages 38

J. Ching, N. Riemer, and M. West. Impacts of black carbon mixing state on black carbon nucleation scavenging: Insights from a particle-resolved model. *Journal of Geophysical Research*, 117(D23209):1–21, Dec. 2012. doi:10.1029/2012JD018269. → pages 36

P. Chýlek, C. M. Banic, B. Johnson, P. A. Damiano, G. A. Isaac, W. R. Leaitch, P. S. K. Liu, F. S. Boudala, B. Winter, and D. Ngo. Black carbon: Atmospheric concentrations and cloud water content measurements over southern Nova Scotia. *Journal of Geophysical Research*, 101(D22):29105–29110, 1996. doi:10.1029/95JD03433. → pages 76

W. Cooke, S. Jennings, and T. Spain. Black carbon measurements at Mace Head, 19891996. *Journal of Geophysical Research*, 102:1989–1996, 1997. doi:10.1029/97JD01430. → pages 52

J. Cozic, B. Verheggen, S. Mertes, P. Connolly, K. Bower, A. Petzold, U. Baltensperger, and E. Weingartner. Scavenging of black carbon in mixed phase clouds at the high alpine site Jungfraujoch. *Atmospheric Chemistry and Physics*, 7(7):1797–1807, 2007. → pages xviii, 36, 37, 49, 76, 83, 88, 99, 110

P. F. DeCarlo, J. R. Kimmel, A. Trimborn, N. M. J., J. T. Jayne, A. C. Aiken, M. Gonin, K. Fuhrer, T. Horvath, K. S. Docherty, D. R. Worsnop, and J. L. Jimenez. Field-deployable, high-resolution, time-of-flight aerosol mass spectrometer. *Analytical Chemistry*, 78(24):8281–8289, 2006. doi:10.1021/ac061249n. → pages 46

R. Draxler and G. Rolph. HYSPLIT (HYbrid Single-Particle Langrangian Integrated Trajectory) Model access via NOAA ARL READY Website . NOAA Air Resources Laboratory, Silver Spring, MD., 2012. URL http://ready.arl.noaa.gov/HYSPLIT.php. → pages 81, 104

R. R. Draxler and G. D. Rolph. HYSPLIT (HYbrid Single-Particle Langrangian Integrated Trajectory) Model access via NOAA ARL READY Website .

NOAA Air Resources Laboratory, Silver Spring, MD., 2013. URL http://ready.arl.noaa.gov/HYSPLIT.php. → pages 47

E. J. Dunlea, P. F. DeCarlo, A. C. Aiken, J. R. Kimmel, R. E. Peltier, R. J. Weber, J. Tomlinson, D. R. Collins, Y. Shinozuka, C. S. McNaughton, S. G. Howell, A. D. Clarke, L. K. Emmons, E. C. Apel, G. G. Pfister, A. van Donkelaar, R. V. Martin, D. B. Millet, C. L. Heald, and J. L. Jimenez. Evolution of Asian aerosols during transpacific transport in INTEX-B. *Atmospheric Chemistry and Physics*, 9(19):7257–7287, Oct. 2009. doi:10.5194/acp-9-7257-2009. → pages 101, 121

U. Dusek, G. P. Frank, A. Massling, K. Zeromskiene, Y. Iinuma, O. Schmid, G. Helas, T. Hennig, A. Wiedensohler, and M. O. Andreae. Water uptake by biomass burning aerosol at sub- and supersaturated conditions: closure studies and implications for the role of organics. *Atmospheric Chemistry and Physics*, 11(18):9519–9532, Sept. 2011. doi:10.5194/acp-11-9519-2011. → pages 16, 36

W. Eugster, R. Burkard, F. Holwerda, F. N. Scatena, and L. Bruijnzeel. Characteristics of fog and fogwater fluxes in a Puerto Rican elfin cloud forest. *Agricultural and Forest Meteorology*, 139(3):288–306, Oct. 2006. → pages 48, 81

L. Fierce, N. Riemer, and T. C. Bond. When is cloud condensation nuclei activity sensitive to particle characteristics at emission? *Journal of Geophysical Research: Atmospheres*, 118(24):13,476–13,488, Dec. 2013. ISSN 2169897X. doi:10.1002/2013JD020608. URL http://doi.wiley.com/10.1002/2013JD020608. → pages 56

B. J. Finlayson-Pitts and J. N. J. Pitts. *Chemistry of the Upper and Lower Atmosphere*. Academic Press, San Diego, 2000. ISBN 0-12-257060-x. → pages 2

J. P. Gallagher, I. G. McKendry, A. M. Macdonald, and W. R. Leaitch. Seasonal and Diurnal Variations in Aerosol Concentration on Whistler Mountain: Boundary Layer Influence and Synoptic-Scale Controls. *Journal of Applied Meteorology and Climatology*, 50(11):2210–2222, Nov. 2011. doi:10.1175/JAMC-D-11-028.1. → pages 109

R. S. Gao, J. P. Schwarz, K. K. Kelly, D. W. Fahey, L. a. Watts, T. L. Thompson, J. R. Spackman, J. G. Slowik, E. S. Cross, J. H. Han, P. Davidovits, T. B. Onasch, and D. R. Worsnop. A Novel Method for Estimating Light-Scattering Properties of Soot Aerosols Using a Modified Single-Particle Soot Photometer. *Aerosol Science and Technology*, 41(2):125–135, 2007. doi:10.1080/02786820601118398. → pages 25, 26, 27, 45

P. Glantz and K. J. Noone. A physically-based algorithm for estimating the relationship between aerosol mass and cloud droplet number. *Tellus B*, 52B: 1216–1231, Nov. 2000. → pages 51

L. Granat, J. E. Engström, S. Praveen, and H. Rodhe. Light absorbing material (soot) in rainwater and in aerosol particles in the Maldives. *Journal of Geophysical Research*, 115(D16307):1–12, Aug. 2010. doi:10.1029/2009JD13768. → pages 37, 77

M. Gysel and J. Crosier. Closure study between chemical composition and hygroscopic growth of aerosol particles during TORCH2. *Atmospheric Chemistry and Physics*, 7(24):6131–6144, 2007. → pages 23, 57, 149

A. Hallberg, J. A. Ogren, K. J. Noone, J. Heintzenberg, A. Berner, I. Solly, C. Kruisz, G. Reischl, S. Fuzzi, M. C. Facchini, H. C. Hansson, A. Wiedensohler, and I. B. Svenningsson. Phase partitioning for different aerosol species in fog. *Tellus B*, 44B(5):545–555, 1992. → pages 36, 37

A. Hallberg, J. A. Ogren, K. J. Noone, K. Okada, J. Heintzenberg, and I. B. Svenningsson. The influence of aerosol particle composition on cloud droplet formation. *Journal of Atmospheric Chemistry*, 19:153–171, 1994. → pages 36, 37, 54

L. N. Hawkins, L. M. Russell, D. S. Covert, P. K. Quinn, and T. S. Bates. Carboxylic acids, sulfates, and organosulfates in processed continental organic aerosol over the southeast Pacific Ocean during VOCALS-REx 2008. *Journal of Geophysical Research*, 115(D13201), July 2010. doi:10.1029/2009JD013276. → pages 51

S. Henning, H. Wex, T. Hennig, A. Kiselev, J. R. Snider, D. Rose, U. Dusek, G. P. Frank, U. Pöschl, A. Kristensson, M. Bilde, R. Tillmann, A. Kiendler-Scharr, T. F. Mentel, S. Walter, J. Schneider, C. Wennrich, and F. Stratmann. Soluble mass, hygroscopic growth, and droplet activation of

coated soot particles during LACIS Experiment in November (LExNo). *Journal of Geophysical Research*, 115(D11206):1–10, June 2010. doi:10.1029/2009JD012626. → pages 36, 37

S. Henning, M. Ziese, A. Kiselev, H. Saathoff, O. Möhler, T. F. Mentel, A. Buchholz, C. Spindler, V. Michaud, M. Monier, K. Sellegri, and F. Stratmann. Hygroscopic growth and droplet activation of soot particles: uncoated, succinic or sulfuric acid coated. *Atmospheric Chemistry and Physics*, 12(10):4525–4537, May 2012. doi:10.5194/acp-12-4525-2012. → pages 36, 37

S. P. Hersey, J. S. Craven, A. R. Metcalf, J. Lin, T. Lathem, K. J. Suski, J. F. Cahill, H. T. Duong, A. Sorooshian, H. H. Jonsson, M. Shiraiwa, A. Zuend, A. Nenes, K. A. Prather, R. C. Flagan, and J. H. Seinfeld. Composition and hygroscopicity of the Los Angeles Aerosol: CalNex. *Journal of Geophysical Research: Atmospheres*, 118(7):3016–3036, Apr. 2013. doi:10.1002/jgrd.50307. → pages 58

R. Hitzenberger, A. Berner, R. Kromp, A. Kasper-Giebl, A. Limbeck, W. Tscherwenka, and H. Puxbaum. Black carbon and other species at a high-elevation European site (Mount Sonnblick, 3106 m, Austria): Concentrations and scavenging efficiencies. *Journal of Geophysical Research*, 105(D20):24637–24645, 2000. → pages 36, 37, 76, 88, 99

R. Hitzenberger, A. Berner, H. Glebl, K. Drobesch, A. Kasper-Giebl, M. Loeflund, H. Urban, and H. Puxbaum. Black carbon (BC) in alpine aerosols and cloud water - concentrations and scavenging efficiencies. *Atmospheric Environment*, 35(30):5135–5141, 2001. → pages 36, 37, 76, 88, 99

R. Holzinger, J. Williams, G. Salisbury, T. Klüpfel, M. de Reus, M. Traub, P. J. Crutzen, and J. Lelieveld. Oxygenated compounds in aged biomass burning plumes over the Eastern Mediterranean: evidence for strong secondary production of methanol and acetone. *Atmospheric Chemistry and Physics*, 5 (1):39–46, Jan. 2005. doi:10.5194/acp-5-39-2005. → pages 83

IPCC-AR4. *Climate Change 2007: The Physical Science Basis. Contributions of Working Group I to the Fourth Assessment Report of the Intergovernmental Panel on Climate Change*. Cambridge University Press, Cambridge, United Kingdom and New York, NY, 2007. → pages xix, 14

IPCC-AR5. *CLIMATE CHANGE 2013: The Physical Science Basis. Working Group I to the Contributions of the Intergovernmental Panel on Climate Change*. Cambridge University Press, Cambridge, United Kingdom and New York, NY, 2013. → pages 6, 7

D. J. Jacob. *Introduction to Atmospheric Chemistry*. Princeton University Press, Princeton, NJ, 1999. → pages 1

M. Z. Jacobson. Investigating cloud absorption effects: Global absorption properties of black carbon, tar balls, and soil dust in clouds and aerosols. *Journal of Geophysical Research*, 117(D06205):1–25, Mar. 2012. doi:10.1029/2011JD017218. → pages 36

J. T. Jayne, D. C. Leard, X. Zhang, P. Davidovits, K. A. Smith, C. E. Kolb, and D. R. Worsnop. Development of an Aerosol Mass Spectrometer for Size and Composition Analysis of Submicron Particles. *Aerosol Science and Technology*, 33(1):49–70, July 2000. doi:10.1080/027868200410840. → pages 104

A. Kasper-Giebl, A. Koch, R. Hitzenberger, and H. Puxbaum. Scavenging efficiency of 'aerosol carbon' and sulfate in soopercooled clouds at Mount Sonnblick (3106 m a.s.l., Austria). *Journal of Atmospheric Chemistry*, 35 (1993):33–46, 2000. → pages 36, 37, 76, 88, 99

Z. Kipling, P. Stier, J. P. Schwarz, A. E. Perring, J. R. Spackman, G. W. Mann, C. E. Johnson, and P. J. Telford. Constraints on aerosol processes in climate models from vertically-resolved aircraft observations of black carbon. *Atmospheric Chemistry and Physics*, 13(12):5969–5986, June 2013. doi:10.5194/acp-13-5969-2013. → pages 101

D. Koch, M. Schulz, S. Kinne, C. McNaughton, J. R. Spackman, Y. Balkanski, S. Bauer, T. Berntsen, T. C. Bond, and Boucher. Evaluation of black carbon estimations in global aerosol models. *Atmospheric Chemistry and Physics*, 9: 9001–9026, 2009. → pages 5

D. Koch, Y. Balkanski, S. E. Bauer, R. C. Easter, S. Ferrachat, S. J. Ghan, C. Hoose, T. Iversen, A. Kirkevå g, J. E. Kristjansson, X. Liu, U. Lohmann, S. Menon, J. Quaas, M. Schulz, O. Seland, T. Takemura, and N. Yan. Soot microphysical effects on liquid clouds, a multi-model investigation.

Atmospheric Chemistry and Physics, 11(3):1051–1064, Feb. 2011. doi:10.5194/acp-11-1051-2011. → pages 36

K. A. Koehler, P. J. DeMott, S. M. Kreidenweis, O. B. Popovicheva, M. D. Petters, C. M. Carrico, E. D. Kireeva, T. D. Khokhlova, and N. K. Shonija. Cloud condensation nuclei and ice nucleation activity of hydrophobic and hydrophilic soot particles. *Physical chemistry chemical physics*, 11(36): 7906–7920, Sept. 2009. doi:10.1039/b905334b. → pages 36

Y. Kondo, N. Oshima, M. Kajino, R. Mikami, N. Moteki, N. Takegawa, R. L. Verma, Y. Kajii, S. Kato, and A. Takami. Emissions of black carbon in East Asia estimated from observations at a remote site in the East China Sea. *Journal of Geophysical Research*, 116(D16201):1–14, Aug. 2011. doi:10.1029/2011JD015637. → pages 105

M. Kuwata, Y. Kondo, and N. Takegawa. Critical condensed mass for activation of black carbon as cloud condensation nuclei in Tokyo. *Journal of Geophysical Research*, 114(D20202):1–9, Oct. 2009. doi:10.1029/2009JD12086. → pages 36

M. Laborde, M. Schnaiter, C. Linke, H. Saathoff, K.-H. Naumann, O. Möhler, S. Berlenz, U. Wagner, J. W. Taylor, D. Liu, M. Flynn, J. D. Allan, H. Coe, K. Heimerl, F. Dahlkötter, B. Weinzierl, a. G. Wollny, M. Zanatta, J. Cozic, P. Laj, R. Hitzenberger, J. P. Schwarz, and M. Gysel. Single Particle Soot Photometer intercomparison at the AIDA chamber. *Atmospheric Measurement Techniques*, 5(12):3077–3097, Dec. 2012. doi:10.5194/amt-5-3077-2012. → pages 102, 103

M. Laborde, M. Crippa, T. Tritscher, Z. Jurányi, P. F. Decarlo, B. Temime-Roussel, N. Marchand, S. Eckhardt, A. Stohl, U. Baltensperger, A. S. H. Prévôt, E. Weingartner, and M. Gysel. Black carbon physical properties and mixing state in the European megacity Paris. *Atmospheric Chemistry and Physics*, 13(11):5831–5856, June 2013. doi:10.5194/acp-13-5831-2013. → pages 109

S. Lance, T. Raatikainen, T. B. Onasch, D. R. Worsnop, X.-Y. Yu, M. L. Alexander, M. R. Stolzenburg, P. H. McMurry, J. N. Smith, and A. Nenes. Aerosol mixing state, hygroscopic growth and cloud activation efficiency during MIRAGE 2006. *Atmospheric Chemistry and Physics*, 13(9): 5049–5062, May 2013. doi:10.5194/acp-13-5049-2013. → pages 58

T. L. Lathem, A. J. Beyersdorf, K. L. Thornhill, E. L. Winstead, M. J. Cubison, A. Hecobian, J. L. Jimenez, R. J. Weber, B. E. Anderson, and A. Nenes. Analysis of CCN activity of Arctic aerosol and Canadian biomass burning during summer 2008. *Atmospheric Chemistry and Physics*, 13(5):2735–2756, Mar. 2013. doi:10.5194/acp-13-2735-2013. → pages 60

W. R. Leaitch, A. M. Macdonald, P. C. Brickell, J. Liggio, S. J. Sjostedt, A. Vlasenko, J. W. Bottenheim, L. Huang, S.-M. Li, P. S. Liu, D. Toom-Sauntry, K. A. Hayden, S. Sharma, N. C. Shantz, H. A. Wiebe, W. Zhang, J. P. Abbatt, J. G. Slowik, R. Y.-W. Chang, L. M. Russell, R. E. Schwartz, S. Takahama, J. T. Jayne, and N. L. Ng. Temperature response of the submicron organic aerosol from temperate forests. *Atmospheric Environment*, 45(37):6696–6704, Dec. 2011. doi:10.1016/j.atmosenv.2011.08.047. → pages 78

D. R. Lide, editor. *CRC Handbook of Chemistry and Physics*. CRC Press, 82 edition, 2001. → pages 58

B. Y. Liu, F. J. Romay, W. D. Dick, K.-S. Woo, and M. Chiruta. A Wide-Range Particle Spectrometer for Aerosol Measurement from 0.010 m to 10 m. *Aerosol and Air Quality Research*, 10:125–139, 2010a. doi:10.4209/aaqr.2009.10.0062. → pages 80

D. Liu, M. Flynn, M. Gysel, A. Targino, I. Crawford, K. Bower, T. Choularton, Z. Jurányi, M. Steinbacher, C. Hüglin, J. Curtius, M. Kampus, A. Petzold, E. Weingartner, U. Baltensperger, and H. Coe. Single particle characterization of black carbon aerosols at a tropospheric alpine site in Switzerland. *Atmospheric Chemistry and Physics*, 10(15):7389–7407, 2010b. doi:10.5194/acp-10-7389-2010. → pages 101, 106, 110, 121

A. M. Macdonald, K. G. Anlauf, W. R. Leaitch, E. Chan, and D. W. Tarasick. Interannual variability of ozone and carbon monoxide at the Whistler high elevation site: 20022006. *Atmospheric Chemistry and Physics*, 11(22): 11431–11446, Nov. 2011. doi:10.5194/acp-11-11431-2011. → pages 78, 101, 109, 110

A. M. Macdonald, W. R. Leaitch, J. P. D. Abbatt, A. K. Betram, D. J. Cziczo, P. Herckes, A. K. Y. Lee, J. Liggio, K. J. Noone, J. R. Pierce, L. M. Russell, S. J. Sjostedt, K. Strawbridge, H. A. Wiebe, L. Ahlm, J. H. Buller, P. Campuzano-Jost, E. Chan, J. Corbin, A. Elford, B. J. Firanski, K. L.

Hayden, S. M. Li, P. S. K. Liu, C. Mihele, D. Toom-Sauntry, S. Sharma, A. Sheppard, J. C. Schroder, J. G. Slowik, G. Stupple, A. Vlasenko, C. D. Wainwright, D. Wang, Y. Wang, J. Wentzell, and J. P. S. Wong. An Overview of WACS 2010: Biogenic Aerosol Formation, Mountain Flows and CCN. *Manuscript*, page In Preparation, 2014. → pages 77, 78, 81, 83

C. Mätzler. MATLAB Functions for Mie Scattering and Absorption Version 1 - Research Report No. 2002-08. 2002a. URL http://www.iap.unibe.ch/publications/download/201/en/. → pages 28

C. Mätzler. MATLAB Functions for Mie Scattering and Absorption Version 2 - Research Report No. 2002-11. 2002b. URL www.iap.unibe.ch/publications/download/199/en/. → pages 28

I. G. McKendry, J. Gallagher, P. Campuzano Jost, A. Bertram, K. Strawbridge, R. Leaitch, and A. M. Macdonald. Ground-based remote sensing of an elevated forest fire aerosol layer at Whistler, BC: implications for interpretation of mountaintop chemistry. *Atmospheric Chemistry and Physics*, 10(23):11921–11930, Dec. 2010. doi:10.5194/acp-10-11921-2010. → pages 78

G. R. McMeeking, T. Hamburger, D. Liu, M. Flynn, W. T. Morgan, M. Northway, E. J. Highwood, R. Krejci, J. D. Allan, A. Minikin, and H. Coe. Black carbon measurements in the boundary layer over western and northern Europe. *Atmospheric Chemistry and Physics*, 10(19):9393–9414, Oct. 2010. doi:10.5194/acp-10-9393-2010. → pages 22

F. Mei, P. L. Hayes, A. Ortega, J. W. Taylor, J. D. Allan, J. Gilman, W. Kuster, J. de Gouw, J. L. Jimenez, and J. Wang. Droplet activation properties of organic aerosols observed at an urban site during CalNex-LA. *Journal of Geophysical Research: Atmospheres*, 118(7):2903–2917, Apr. 2013. doi:10.1002/jgrd.50285. → pages 60

A. R. Metcalf, J. S. Craven, J. J. Ensberg, J. Brioude, W. Angevine, A. Sorooshian, H. T. Duong, H. H. Jonsson, R. C. Flagan, and J. H. Seinfeld. Black carbon aerosol over the Los Angeles Basin during CalNex. *Journal of Geophysical Research: Atmospheres*, 117(D00V13):1–24, Nov. 2012. doi:10.1029/2011JD17255. → pages 29, 36, 52, 54, 55, 106, 111, 128

R. H. Moore, K. Cerully, R. Bahreini, C. A. Brock, A. M. Middlebrook, and A. Nenes. Hygroscopicity and composition of California CCN during summer 2010. *Journal of Geophysical Research: Atmospheres*, 117(D00V12):1–14, Nov. 2012. doi:10.1029/2011JD017352. → pages 16, 58

N. Moteki and Y. Kondo. Method to measure time-dependent scattering cross sections of particles evaporating in a laser beam. *Journal of Aerosol Science*, 39:348 – 364, Dec. 2008. doi:10.1016/j.jaerosci.2007.12.002. → pages 44

N. Moteki, Y. Kondo, N. Takegawa, and S.-i. Nakamura. Directional dependence of thermal emission from nonspherical carbon particles. *Journal of Aerosol Science*, 40(9):790–801, Sept. 2009. doi:10.1016/j.jaerosci.2009.05.003. → pages 23

N. L. Ng, S. C. Herndon, A. Trimborn, M. R. Canagaratna, P. L. Croteau, T. B. Onasch, D. Sueper, D. R. Worsnop, Q. Zhang, Y. L. Sun, and J. T. Jayne. An Aerosol Chemical Speciation Monitor (ACSM) for Routine Monitoring of the Composition and Mass Concentrations of Ambient Aerosol. *Aerosol Science and Technology*, 45(7):780–794, July 2011. doi:10.1080/02786826.2011.560211. → pages 104

K. J. Noone, J. a. Ogren, J. Heintzenberg, R. J. Charlson, and D. S. Covert. Design and Calibration of a Counterflow Virtual Impactor for Sampling of Atmospheric Fog and Cloud Droplets. *Aerosol Science and Technology*, 8(3): 235–244, Jan. 1988. → pages 42, 43, 44, 79

K. J. Noone, J. A. Ogren, A. Hallberg, J. Heintzenberg, J. Ström, H.-C. Hansson, B. Svenningsson, A. Wiedensohler, M. C. Facchinni, B. G. Arends, and A. Berner. Changes in aerosol-size- and phase distributions due to physical and chemical processes in fog. *Tellus*, 44B:489–504, 1992. → pages 36, 59

C. O'Dowd, E. Becker, and M. Kulmala. Mid-latitude North-Atlantic aerosol characteristics in clean and polluted air. *Atmospheric Research*, 58(3): 167–185, 2001. → pages 51

J. Ovadnevaite, D. Ceburnis, M. Canagaratna, H. Berresheim, J. Bialek, G. Martucci, D. R. Worsnop, and C. O'Dowd. On the effect of wind speed on submicron sea salt mass concentrations and source fluxes. *Journal of Geophysical Research*, 117(D16201):1–11, Aug. 2012. doi:10.1029/2011JD017379. → pages 60

M. S. Pekour and D. J. Cziczo. Wake capture, particle breakup, and other artifacts associated with counterflow virtual impaction. *Aerosol Science and Technology*, 45:758–764, 2011. doi:10.1080/02786826.2011.558942. → pages 52

M. D. Petters and S. M. Kreidenweis. A single parameter representation of hygroscopic growth and cloud condensation nucleus activity. *Atmospheric Chemistry and Physics*, 7(8):1961–1971, Apr. 2007. → pages xix, 16, 17, 19, 58

M. D. Petters, C. M. Carrico, S. M. Kreidenweis, A. J. Prenni, P. J. DeMott, J. L. Collett, and H. Moosmüller. Cloud condensation nucleation activity of biomass burning aerosol. *Journal of Geophysical Research*, 114(D22205): 1–16, Nov. 2009. doi:10.1029/2009JD012353. → pages 16, 36, 37, 89

A. Petzold, M. Gysel, X. Vancassel, R. Hitzenberger, H. Puxbaum, S. Vrochticky, E. Weingartner, U. Baltensperger, and P. Mirabel. On the effects of organic matter and sulphur-containing compounds on the CCN activation of combustion particles. *Atmospheric Chemistry and Physics*, 5(12): 3187–3203, Dec. 2005. → pages 36, 37

A. Petzold, J. A. Ogren, M. Fiebig, P. Laj, S.-M. Li, U. Baltensperger, T. Holzer-Popp, S. Kinne, G. Pappalardo, N. Sugimoto, C. Wehrli, A. Wiedensohler, and X.-Y. Zhang. Recommendations for reporting "black carbon" measurements. *Atmospheric Chemistry and Physics*, 13(16): 8365–8379, Aug. 2013. doi:10.5194/acp-13-8365-2013. → pages 4

J. R. Pierce, W. R. Leaitch, J. Liggio, D. M. Westervelt, C. D. Wainwright, J. P. D. Abbatt, L. Ahlm, W. Al-Basheer, D. J. Cziczo, K. L. Hayden, A. K. Y. Lee, S.-M. Li, L. M. Russell, S. J. Sjostedt, K. B. Strawbridge, M. Travis, A. Vlasenko, J. J. B. Wentzell, H. a. Wiebe, J. P. S. Wong, and a. M. Macdonald. Nucleation and condensational growth to CCN sizes during a sustained pristine biogenic SOA event in a forested mountain valley. *Atmospheric Chemistry and Physics*, 12(7):3147–3163, Apr. 2012. doi:10.5194/acp-12-3147-2012. → pages 81

L. Pirjola and C. O'Dowd. Can new particle formation occur in the clean marine boundary layer? *Journal of Geophysical Research*, 105(D21):26531–26546, 2000. → pages 51

O. B. Popovicheva, N. M. Persiantseva, E. D. Kireeva, T. D. Khokhlova, and N. K. Shonija. Quantification of the hygroscopic effect of soot aging in the atmosphere: laboratory simulations. *The Journal of Physical Chemistry. A*, 115(3):298–306, Jan. 2011. doi:10.1021/jp109238x. → pages 36, 37

K. A. Pratt, S. M. Murphy, R. Subramanian, P. J. DeMott, G. L. Kok, T. Campos, D. C. Rogers, A. J. Prenni, a. J. Heymsfield, J. H. Seinfeld, and K. A. Prather. Flight-based chemical characterization of biomass burning aerosols within two prescribed burn smoke plumes. *Atmospheric Chemistry and Physics*, 11(24): 12549–12565, Dec. 2011. doi:10.5194/acp-11-12549-2011. → pages 89

A. J. Prenni, M. D. Petters, S. M. Kreidenweis, P. J. DeMott, and P. J. Ziemann. Cloud droplet activation of secondary organic aerosol. *Journal of Geophysical Research*, 112(D10223):1–12, May 2007. doi:10.1029/2006JD007963. → pages 16

N. Riemer, H. Vogel, and B. Vogel. Soot aging time scales in polluted regions during day and night. *Atmospheric Chemistry and Physics*, 4(7):1885–1893, 2004. → pages 36

N. Riemer, M. West, R. Zaveri, and R. Easter. Estimating black carbon aging time-scales with a particle-resolved aerosol model. *Journal of Aerosol Science*, 41(1):143–158, Jan. 2010. doi:10.1016/j.jaerosci.2009.08.009. → pages 36

G. Rolph. Real-time Environmental Applications and Display sYstem (READY) Website, NOAA Air Resources Laboratory, Silver Spring, MD, 2012. URL http//ready.arl.noaa.gov. → pages 81, 104

G. D. Rolph. Real-time Environmental Application and Display sYstem (READY) Website. NOAA Air Resources Laboratory, Silver Spring, MD. 2013. URL http//ready.arl.noaa.gov. → pages 47

D. Rose, B. Wehner, M. Ketzel, C. Engler, J. Voigtländer, T. Tuch, and A. Wiedensohler. Atmospheric number size distributions of soot particles and estimation of emission factors. *Atmospheric Chemistry and Physics*, 6(4): 1021–1031, 2006. → pages 128

D. Rose, S. S. Gunthe, E. Mikhailov, G. P. Frank, U. Dusek, M. O. Andreae, and U. Pöschl. Calibration and measurement uncertainties of a continuous-flow cloud condensation nuclei counter (DMT-CCNC): CCN activation of

ammonium sulfate and sodium chloride aerosol particles in theory and experiment. *Atmospheric Chemistry and Physics*, 8(5):1153–1179, Feb. 2008. → pages 59

D. Rose, A. Nowak, P. Achtert, A. Wiedensohler, M. Hu, M. Shao, Y. Zhang, M. O. Andreae, and U. Pöschl. Cloud condensation nuclei in polluted air and biomass burning smoke near the mega-city Guangzhou, China Part 1: Size-resolved measurements and implications for the modeling of aerosol particle hygroscopicity and CCN activity. *Atmospheric Chemistry and Physics*, 10(7):3365–3383, Apr. 2010. → pages 16, 58, 61

L. K. Sahu, Y. Kondo, N. Moteki, N. Takegawa, Y. Zhao, M. J. Cubison, J. L. Jimenez, S. Vay, G. S. Diskin, A. Wisthaler, T. Mikoviny, L. G. Huey, A. J. Weinheimer, and D. J. Knapp. Emission characteristics of black carbon in anthropogenic and biomass burning plumes over California during ARCTAS-CARB 2008. *Journal of Geophysical Research*, 117(D16302):1–20, Aug. 2012. doi:10.1029/2011JD017401. → pages 106

J. C. Schroder, S. J. Hanna, R. L. Modini, A. L. Corrigan, A. M. Macdonald, K. J. Noone, L. M. Russell, W. R. Leaitch, and A. K. Bertram. Size-resolved observations of refractory black carbon particles in cloud droplets at a marine boundary layer site. *Atmospheric Chemistry and Physics Discussions*, 14: 11447–11491, 2014. doi:10.5194/acp-14-11447-2014. → pages 77

J. P. Schwarz, R. S. Gao, D. W. Fahey, D. S. Thomson, L. A. Watts, J. C. Wilson, J. M. Reeves, M. Darbeheshti, D. G. Baumgardner, G. L. Kok, S. H. Chung, M. Schulz, J. Hendricks, A. Lauer, B. Kärcher, J. G. Slowik, K. H. Rosenlof, T. L. Thompson, a. O. Langford, M. Loewenstein, and K. C. Aikin. Single-particle measurements of midlatitude black carbon and light-scattering aerosols from the boundary layer to the lower stratosphere. *Journal of Geophysical Research*, 111(D16207):1–15, 2006. doi:10.1029/2006JD007076. → pages 22, 24, 25, 44

J. P. Schwarz, R. S. Gao, J. R. Spackman, L. A. Watts, D. S. Thomson, D. W. Fahey, T. B. Ryerson, J. Peischl, J. S. Holloway, M. Trainer, G. J. Frost, T. Baynard, D. a. Lack, J. a. de Gouw, C. Warneke, and L. a. Del Negro. Measurement of the mixing state, mass, and optical size of individual black carbon particles in urban and biomass burning emissions. *Geophysical Research Letters*, 35(13):L13810, July 2008a. doi:10.1029/2008GL033968. → pages 29, 55, 106, 109, 128

J. P. Schwarz, J. R. Spackman, D. W. Fahey, R. S. Gao, U. Lohmann, P. Stier, L. a. Watts, D. S. Thomson, D. A. Lack, L. Pfister, M. J. Mahoney, D. Baumgardner, J. C. Wilson, and J. M. Reeves. Coatings and their enhancement of black carbon light absorption in the tropical atmosphere. *Journal of Geophysical Research*, 113(D03203):1–10, Feb. 2008b. doi:10.1029/2007JD009042. → pages 29, 36

J. P. Schwarz, J. R. Spackman, R. S. Gao, a. E. Perring, E. Cross, T. B. Onasch, A. Ahern, W. Wrobel, P. Davidovits, J. Olfert, M. K. Dubey, C. Mazzoleni, and D. W. Fahey. The Detection Efficiency of the Single Particle Soot Photometer. *Aerosol Science and Technology*, 44(8):612–628, June 2010a. doi:10.1080/02786826.2010.481298. → pages 102

J. P. Schwarz, J. R. Spackman, R. S. Gao, L. A. Watts, P. Stier, M. Schulz, S. M. Davis, S. C. Wofsy, and D. W. Fahey. Global-scale black carbon profiles observed in the remote atmosphere and compared to models. *Geophysical Research Letters*, 37(18):L18812, Sept. 2010b. doi:10.1029/2010GL044372. → pages 101

J. P. Schwarz, B. H. Samset, A. E. Perring, J. R. Spackman, R. S. Gao, P. Stier, M. Schulz, F. L. Moore, E. A. Ray, and D. W. Fahey. Global-scale seasonally resolved black carbon vertical profiles over the Pacific. *Geophysical Research Letters*, 40(20):5542–5547, Oct. 2013. doi:10.1002/2013GL057775. → pages 101

A. Schwarzenboeck, J. Heintzenberg, and S. Mertes. Incorporation of aerosol particles between 25 and 850 nm into cloud elements: measurements with a new complementary sampling system. *Atmospheric research*, 52:241–260, 2000. → pages 52

A. J. Sedlacek, E. R. Lewis, L. Kleinman, J. Xu, and Q. Zhang. Determination of and evidence for non-core-shell structure of particles containing black carbon using the Single-Particle Soot Photometer (SP2). *Geophysical Research Letters*, 39(6):L06802, Mar. 2012. doi:10.1029/2012GL050905. → pages 29, 54

J. H. Seinfeld and S. N. Pandis. *Atmospheric Chemistry and Physics: From Air Pollution to Climate Change*. John Wiley & Sons, Hoboken, NJ, 2nd edition, 2006. ISBN 978-0-471-72017-1. → pages 3, 16

K. Sellegri, P. Laj, R. Dupuy, M. Legrand, S. Preunkert, and J. P. Putaud. Size-dependent scavenging efficiencies of multicomponent atmospheric aerosols in clouds. *Journal of Geophysical Research*, 108(D11):4334, 2003. doi:10.1029/2002JD002749. → pages 36, 37, 76, 88, 99

J. S. Serafini. Impingement of water droplets on wedges and double-wedge airfoils at supersonic speeds. *NACA*, TR 1159, 1954. → pages 43

L. M. Shank, S. Howell, A. D. Clarke, S. Freitag, V. Brekhovskikh, V. Kapustin, C. McNaughton, T. Campos, and R. Wood. Organic matter and non-refractory aerosol over the remote Southeast Pacific: oceanic and combustion sources. *Atmospheric Chemistry and Physics*, 12(1):557–576, Jan. 2012. doi:10.5194/ACP-12-557-2012. → pages 52

N. C. Shantz, W. R. Leaitch, L. Phinney, M. Mozurkewich, and D. Toom-Sauntry. The effect of organic compounds on the growth rate of cloud droplets in marine and forest settings. *Atmospheric Chemistry and Physics*, 8(19):5869–5887, Apr. 2008. → pages 58

Z. Shen, J. Liu, L. W. Horowitz, D. K. Henze, S. Fan, H. Levy II, D. L. Mauzerall, J.-T. Lin, and S. Tao. Analysis of transpacific transport of black carbon during HIPPO-3: implications for black carbon aging. *Atmospheric Chemistry and Physics Discussions*, 14(1):505–540, 2014. doi:10.5194/acpd-14-505-2014. → pages 101

B. Simoneit, J. Schauer, C. Nolte, D. Oros, V. Elias, M. Fraser, W. Rogge, and G. Cass. Levoglucosan, a tracer for cellulose in biomass burning and atmospheric particles. *Atmospheric Environment*, 33(2):173–182, Jan. 1999. doi:10.1016/S1352-2310(98)00145-9. → pages 107

J. G. Slowik, E. S. Cross, J.-H. Han, P. Davidovits, T. B. Onasch, J. T. Jayne, L. R. Williams, M. R. Canagaratna, D. R. Worsnop, R. K. Chakrabarty, H. Moosmüller, W. P. Arnott, J. P. Schwarz, R.-S. Gao, D. W. Fahey, G. L. Kok, and A. Petzold. An Inter-Comparison of Instruments Measuring Black Carbon Content of Soot Particles. *Aerosol Science and Technology*, 41(3): 295–314, Apr. 2007. ISSN 0278-6826. doi:10.1080/02786820701197078. URL http://www.tandfonline.com/doi/abs/10.1080/02786820701197078. → pages 38

M. Stephens, N. Turner, and J. Sandberg. Particle identification by laser-induced incandescence in a solid-state laser cavity. *Applied optics*, 42(19):3726–3736, July 2003. → pages 20, 22, 44

B. Stevens, G. Feingold, W. R. Cotton, and R. L. Walko. Elements of the Microphysical Structure of Numerically Simulated Nonprecipitating Stratocumulus. *Journal of the Atmospheric Sciences*, 53(7):980–1006, 1995. → pages 55

R. B. Stull. *Introduction to Boundary Layer Meteorology*. Kluwer Academic Press, Dordrecht, Netherlands, 2003. doi:10.1007/978-94-009-3027-8. → pages 2

S. Takahama, R. E. Schwartz, L. M. Russell, A. M. Macdonald, S. Sharma, and W. R. Leaitch. Organic functional groups in aerosol particles from burning and non-burning forest emissions at a high-elevation mountain site. *Atmospheric Chemistry and Physics*, 11(13):6367–6386, July 2011. doi:10.5194/acp-11-6367-2011. → pages 78, 101, 104, 107

C. H. Twohy, M. D. Petters, J. R. Snider, B. Stevens, W. Tahnk, M. Wetzel, L. M. Russell, and F. Burnet. Evaluation of the aerosol indirect effect in marine stratocumulus clouds: Droplet number, size, liquid water path, and radiative impact. *Journal of Geophysical Research*, 110:1–16, 2005. doi:10.1029/2004JD005116. → pages 51

B. Verheggen, J. Cozic, E. Weingartner, K. Bower, S. Mertes, P. Connolly, M. Gallagher, M. Flynn, T. Choularton, and U. Baltensperger. Aerosol partitioning between the interstitial and the condensed phase in mixed-phase clouds. *Journal of Geophysical Research*, 112(D23):1–13, Dec. 2007. doi:10.1029/2007JD008714. → pages 36, 37

G. Vidaurre, J. Hallett, and D. C. Rogers. Airborne Measurement of Liquid and Total Water Content. *Journal of Atmospheric and Oceanic Technology*, 28(9): 1088–1103, Sept. 2011. → pages 52

E. Vignati, M. Karl, M. Krol, J. Wilson, P. Stier, and F. Cavalli. Sources of uncertainties in modelling black carbon at the global scale. *Atmospheric Chemistry and Physics*, 10(6):2595–2611, Mar. 2010. → pages 36

S.-L. Von der Weiden, F. Drewnick, and S. Borrmann. Particle Loss Calculator a new software tool for the assessment of the performance of aerosol inlet

systems. *Atmospheric Measurement Techniques*, 2(2):479–494, Sept. 2009. → pages 40

J. M. Wallace and P. V. Hobbs. *Atmospheric Science: An Introductory Survey*. Academic Press, London, United Kingdom, 2nd edition, 2006. → pages xix, 1, 13

C. Wang. Impact of anthropogenic absorbing aerosols on clouds and precipitation: A review of recent progresses. *Atmospheric Research*, 122: 237–249, Mar. 2013. → pages 36

Q. Wang, D. J. Jacob, J. R. Spackman, A. E. Perring, J. P. Schwarz, N. Moteki, E. a. Marais, C. Ge, J. Wang, and S. R. H. Barrett. Global budget and radiative forcing of black carbon aerosol: Constraints from pole-to-pole (HIPPO) observations across the Pacific. *Journal of Geophysical Research: Atmospheres*, 119(1):195–206, Jan. 2014. doi:10.1002/2013JD020824. → pages 10, 113, 121

Z. Wang, H. Zhang, J. Li, X. Jing, and P. Lu. Radiative forcing and climate response due to the presence of black carbon in cloud droplets. *Journal of Geophysical Research: Atmospheres*, 118:1–14, May 2013. doi:10.1002/jgrd.50312. → pages 36

Z. J. Wu, L. Poulain, S. Henning, K. Dieckmann, W. Birmili, M. Merkel, D. van Pinxteren, G. Spindler, K. Müller, F. Stratmann, H. Herrmann, and A. Wiedensohler. Relating particle hygroscopicity and CCN activity to chemical composition during the HCCT-2010 field campaign. *Atmospheric Chemistry and Physics*, 13(16):7983–7996, Aug. 2013. doi:10.5194/acp-13-7983-2013. → pages 58

B. L. Zhuang, L. Liu, F. H. Shen, T. J. Wang, and Y. Han. Semidirect radiative forcing of internal mixed black carbon cloud droplet and its regional climatic effect over China. *Journal of Geophysical Research*, 115(May):D00K19, Sept. 2010. doi:10.1029/2009JD013165. → pages 36

Appendix A

HR-ToF-AMS Ion Pairing Scheme used in Chapter 4

The inorganic ions (NH_4^+, NO_3^-, SO_4^{2-}, Cl^-) mass fractions measured with the HR-ToF-AMS were converted to mass fractions of ammonium nitrate, ammonium sulfate, ammonium bisulfate, sulfuric acid, or ammonium chloride using the sim-

plified ion-pairing scheme below:

$$
\begin{aligned}
n_{NH_4NO_3} &= n_{NO_3^-} \\
n_{NH_4Cl} &= n_{Cl^-} \\
n_{(NH_4)_2SO_4} &= max(0, n_{NH_4^+} - n_{SO_4^{2-}} - n_{NO_3^-} - n_{Cl^-}) \\
n_{NH_4HSO_4} &= min(2n_{SO_4^{2-}} - \ n_{NH_4^+} + n_{NO_3^-} + n_{Cl^-}, \\
&\qquad\qquad n_{NH_4^+} - n_{NO_3^-} - n_{Cl^-}) \\
n_{H_2SO_4} &= max(0, n_{SO_4^{2-}} - n_{NH_4^+} + n_{NO_3^-} + n_{Cl^-})
\end{aligned}
$$

Where n is the number of moles of that species. This ion scheme is the same as the one used by Gysel and Crosier (2007) except it has been modified to incorporate ammonium chloride.

Appendix B

Calculation of the Droplet Transmission Factor Through the CVI used in Chapter 4

The droplet transmission factor (DT) through the CVI was determined by plotting the number of droplets measured by the FM-100 that were greater than the $CVI - D_{50}$ as a function of the number of residual particles (see Figure B.1). The number of residual particles plotted in Figure B.1 were corrected for the CVI enhancement factor (EF) and only residual particles $>$100 nm were included since particles smaller than this size were likely not due to nucleation scavenging (see Section 4.4.3.2 for further discussion). From 1/slope in Figure B.1 panels A and B, the DT values were determined to be 26% during Cloud 2 and 45% during Cloud 3. DT values less than 100% may be attributed to ; 1) particle or droplet losses in

the CVI; 2) incomplete drying of the droplets; 3) misalignment of droplets in the wind tunnel prior to entering the CVI; and 4) insufficient acceleration of some of the larger droplets.

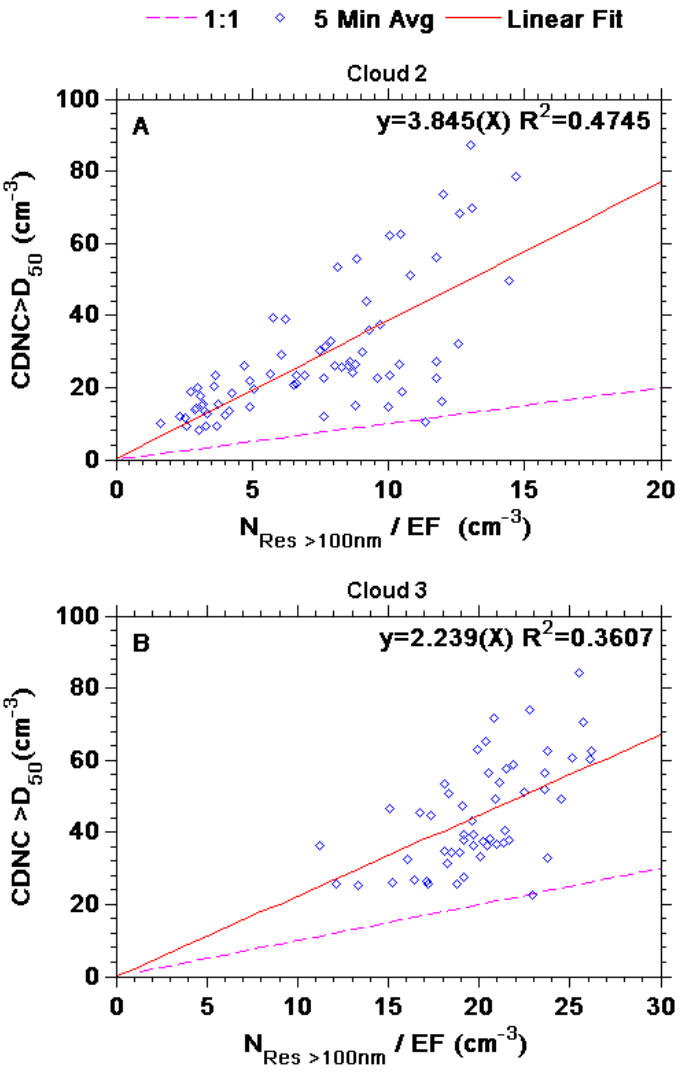

Figure B.1: Correlation plots between the cloud droplet number concentration (CDNC) greater than the $CVI - D_{50}$ (CDNC $> D_{50}$) and the enhancement factor (EF) corrected residual number concentration greater than 100 nm ($N_{Res>100nm}$) in cm^{-3}.

Appendix C

Calculation of the Droplet Transmission Factor Through the CVI used in Chapter 5

To account for droplet losses during CVI sampling a droplet transmission (DT) factor was determined by plotting the CDNC that was greater than the CVI cut-size as a function of the number of residual particles counted by a CPC (TSI-3775), which counted all residual particles behind the CVI with diameters between 10 nm and 1 μm (Figure C.1). The number of residual particles counted by the CPC was corrected for the enhancement of particles by the CVI. The droplet transmissions were calculated from 1/slope of linear fits to the data shown in Figure C.1 panels A and B, and were found to be 33 and 35% for Clouds 1 and 2, respectively. A DT value of less than 100% may be due to; particle or droplet losses

in the CVI or tubing downstream of the CVI; droplets improperly aligned within the wind tunnel prior to entering the CVI; incomplete drying of the droplets; and insufficiently accelerating some of the larger droplets, which would result in rejection of the droplet by the counterflow. Droplet transmission values reported here are similar to values reported in the study described in Chapter 4.

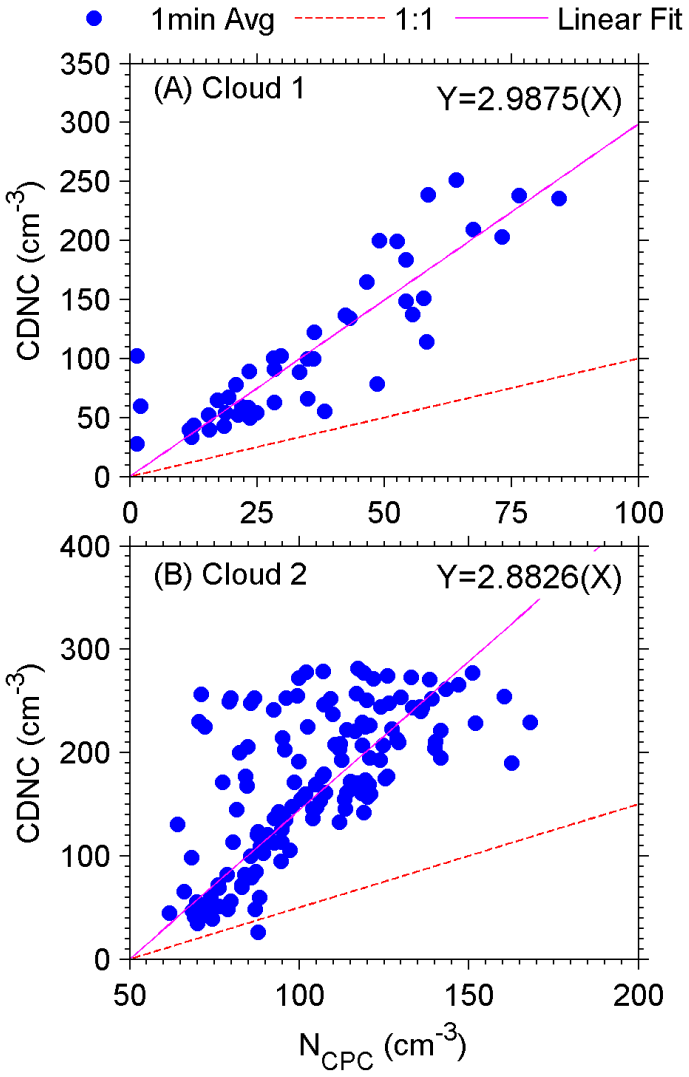

Figure C.1: Correlation plots for Clouds 1 and 2 in panels A and B, respectively, of the cloud droplet number concentration (CDNC) for droplets that are greater than the CVI cut-size as a function of the enhancement factor corrected residual number concentration. The slope of the linear fits to the correlation data represent the scaling factor needed to account for droplet losses and 1/slope represents the droplet transmission.